RUPTURE POINT MOVEMENT IN JOURNAL BEARINGS

A Thesis

Submitted to the Faculty of

WORCESTER POLYTECHNIC INSTITUTE

In partial fulfillment of the requirements for the

Degree of Master of Science

In

Mechanical Engineering

By

Richard J. Bara

May 26, 2004

Approved by:

Professor Joseph J. Rencis, Major Advisor

Dr. Coda H.T. Pan, Industrial Co-Advisor

Professor Grétar Tryggvason, Department Head, Committee Member

Professor John M. Sullivan, Committee Member

Professor Michael A. Demetriou, Graduate Committee Representative

Abstract

Two most important events in the history of lubrication theory are attributed to Reynolds and Sommerfeld. Reynolds derived the governing equations for lubricating films in simplifying the Navier-Stokes equations considering thin-film effects. Sommerfeld obtained a closed form analytical solution to the Reynolds equation for the long bearing (one-dimensional case) with fixed constant eccentricity which results in a point symmetric pressure profile compared to an arbitrary (ambient) level.

In attempting to reconcile with experimental evidence, Gumbel advanced the argument that sub-ambient pressure in a fluid film is not possible. On the basis that the fluid film would rupture, he put forth that the sub-ambient portion of the Sommerfeld solution should be discarded, a proposition that is commonly recognized as the half-Sommerfeld solution (of Gumbel). Ever since Gumbel suggested this improvement, much interest remains regarding the physical process of rupture in bearing lubricating films. In lubrication literature, cavitation is used interchangeably with rupture to indicate a condition in which an abundance of a gas phase, essentially ambient air, is present in a portion of the bearing clearance.

A cogent two-phase morphology for addressing cavitation in long bearings is postulated in order to predict time-dependent fluid behavior from an initial state that is a generalization of Gumbel's half-Sommerfeld solution. The ultimate steady-state is presumed to satisfy the hypothesis of Swift and Stieber that an ambient condition is reached by the rupture point at an unspecified location simultaneously with a vanishing pressure gradient. A trans-rupture continuity equation, as proposed by Olsson, determines a formula for the speed of a moving rupture point requiring a specific model of the two-phase flow in the rupture region. Employing an adhered film model, sequential application of Olsson's equation to the rupture points of the intermediate states between the half-Sommerfeld and Swift-Stieber states renders an interpretation of a time-dependent progression towards a steady-state solution.

Closed form analytical formulas, which readily combine to provide an exact solution to the Reynolds equation are derived with the start (formation point) of the full-film other than the customary bearing maximum gap and with the rupture point at any assigned intermediate location. Each valid solution for an intermediate state yields an invariant flux that must satisfy a window of constraints to exclude the possibility of sub-ambient pressures. A complete set of such valid solutions exists for each fixed eccentricity and can be depicted as a contour plot of the invariant flux with formation and rupture points as coordinates.

The method can readily be extended to two-dimensions, offering a promising alternative to the Elrod cavitation algorithm, which is commonly used in more comprehensive bearing analyses.

Acknowledgements

I would like to thank my advisor Professor Rencis for providing direction, keeping me on schedule, putting my ideas to the test and making numerous corrections. His guidance, helpful suggestions and reassurance were invaluable.

I am sincerely grateful to Dr. Coda Pan for being an exceptional mentor and offering outstanding background and expertise in lubrication theory and practice (and for his share of editing, too). His contributions and continued interest in the field are inspiring.

I wish to acknowledge the National Science Foundation who generously funded my education as part of a Graduate K-12 Teaching Fellowship.

Finally, I am forever indebted to the love of my life, Marie-Claude, for believing in me, encouraging me and supporting me every step of the way. I would not be where I am today without her.

Contents

List of Figures

List of Tables

List of Symbols

C	Radial Clearance	x	Coordinate Axis in Circumferential Direction
D	Journal Diameter	y	Coordinate Axis in Radial Direction
e	Eccentricity	z	Coordinate Axis in Axial Direction
g	Flag for Switch Function (refer to Elrod Algorithm)	Z	Non-dimensional Axial Coordinate
h	Film Thickness	α	Void Fraction used with Film Thickness
H	Non-dimensional Film Thickness	β	Fluid Bulk Modulus (refer to Elrod Algorithm)
I_2, I_3	Integrals for Component of Bearing Load in y-direction (W_y)	γ	Attitude Angle
J_1, J_2, J_3	Reynolds Equation Integrals	δ	Small Number Used to Compare Pressure to Zero (refer to Bisection Method)
L	Journal Length	ε	Non-dimensional Eccentricity
F_f	Frictional Force	θ	Circumferential Distance from Maximal Gap (radians)
p	Fluid Pressure	Θ	State Variable with Dual Meaning (see Elrod Algorithm)
P	Non-dimensional Fluid Pressure	μ	Absolute Viscosity ($Pa \cdot s$ or $N/m^2 \cdot s$)
R	Journal Radius	ϕ	Fluid Flux in Circumferential Direction
T	Non-dimensional Time	Φ	Non-dimensional Fluid Flux in Axial Direction
u	Fluid Velocity in Circumferential Direction	ψ	Fluid Flux in Axial Direction
U	Non-dimensional Velocity in Radial Direction	Ψ	Non-dimensional Fluid Flux in Axial Direction
W	Bearing Load	ω	Angular Velocity of Journal (rad/sec)

Often Used Subscripts

a	Pertaining to Adhered Film	ref	At Reformation Point
form	At Formation Point	rup	At Rupture Point
m	At Makeup Point (Supply Groove)	ss	Steady-state
min	At Minimum Gap	SS	At Swift-Stieber Point or Along Swift-Stieber Line
max	At Maximum Gap	o	"naught" or "zero", At Point of Maximum Pressure

1. Introduction

1.1 Goal

Ever since Gumbel [1.1] suggested the half-Sommerfeld solution as an improvement to journal bearing analysis, much interest viremains regarding the physical process of rupture in bearing lubricating films. The *goal* of this work is provide a complete temporal development in a long journal bearing, with an arbitrary supply groove placement, that accurately follows the rupture meniscus movement from an assumed initial Gumbel condition towards the Swift-Stieber condition. An improved understanding of rupture phenomena should lead to significant advances in the numerical analysis of cavitated films in journal bearings.

1.2 Objectives

The four research objectives consist of:

1. *Postulating a Cogent Two-phase Flow Structure in the Ruptured Region.* A morphological description, that is consistent with known experimental evidence and is amenable to analytical treatment, will be established for the ruptured region.
2. *Satisfying Olsson's Equation at the Terminal Points of the Full-film Region.* Olsson's equation will be imposed across the junction between the two-phase flow region and either terminal point of the full-fluid film; flow rate will be calculated at a fixed supply groove and meniscus movement speed will be determined for the rupture point.

3. *Computing Time to Intermediate Rupture States.* Making use of the rupture meniscus speed and treating the intermediate location of the rupture point as a "state variable," the entire history of the rupture point location can be determined.
4. *Establishing the Evolving Two-phase Flow Structure.* While the rupture point is moving toward the Swift-Stieber location, fluid that passes through the rupture point modifies the two-phase flow structure concurrently.

1.3 Scope

All analysis is performed for the one-dimensional problem of a single supply groove with a connection to an ambient level reservoir that fixes the starting location of the full-film region. Eccentricity is kept constant; thereby squeeze effect on the fluid is excluded.

1.4 Strategies

The following strategies are employed to fulfill the four research objectives**:**

- *Generalize Analytical Formulas of the Sommerfeld Solution.* Analytical formulations will be pursued in place of conventional discretized computation. However, in lieu of the so-called "Sommerfeld derivation," integrals that can be readily computed with modern computational software are derived which combine to form fast, compact and accurate solutions to the Reynolds equation in the full-film region for arbitrary terminal points at any fixed eccentricity.
- *Construct Gumbel Charts.* Contour plots will be constructed of the non-dimensional flux as a function of terminal points of the generalized Gumbel solution.

- *Perform Inverse Time-domain Integration.* The rupture meniscus movement is constructed as time-from-start for the present rupture location, which is treated as a state variable; "surface clocked" location of a prior state would be determined by interpolation.
- *Calculation of Additional Performance Parameters.* Additional formulations are derived in terms of the aforementioned integrals for rapid calculations of the load components and frictional force.

1.5 Literature Review

1.5.1 Reynolds Equation and the Gumbel Solution

Reynolds [1.2] introduced the basic hydrodynamic fluid equation in 1886 recognizing that the full Navier-Stokes equations are not necessary for the thin-film in a bearing. Sommerfeld [1.3] presented a periodic analytical solution to the Reynolds equation for the long bearing that is relevant today with long journal bearings and light loads or sufficient pressure to maintain full film (see Appendix A-1). Gumbel [1.1] observed oil could not sustain much negative pressure in the divergent region of the bearing and argued the half-Sommerfeld solution as being a better approximation of reality. As with long bearing theory, the half-bearing approximation is emulated in the numerical solution of finite length journal bearings by omitting the sub-ambient portion of the computed result.

1.5.2 Experiments of Film Rupture

In the industrial application of thin-film lubrication, it is recognized that the clearance may not be fully filled by the lubricant and a void region containing mainly air in contact with ambient air may occupy a portion of the bearing gap in the divergent section. It is generally agreed that the void presents a uniform pressure condition to its boundary with the liquid film. The actual liquid-gas two-phase morphology remains a topic that invites attention of lubrication researches from time to time. The Proceedings of the 1st Leeds-Lyon Symposium [1.4] marks such an event and Brewe et al. [1.5] reported on a more recent occurrence.

Photographic records obtained by Dowson [1.4] are typical of visual observations of the ruptured film in the steady-state operation of an eccentric journal bearing. They provide a glimpse into the actual two-phase morphology that is of interest. The experiment, shown pictorially in Figure 1-1, involves a rotating cylindrical drum submerged in oil over a clear, flat plate. Figures 1-2, 1-3 and 1-4 show the three different cavitation patterns that form depending on the speed of the rotating drum. At slower speeds (Figure 1-2), separated bubbles form with the oil passing both in between the bubbles and possibly separating from the drum. At moderate speeds, the comb-like appearance (Figure 1-3) is common, which features oil streams separating the bubbles, becoming thinner as the gap diverges, eventually terminating in an open ring. At higher speeds (Figure 1-4), the bubbles coalesce to form a single sheet with a well-defined boundary between the full-film region and a void region with the oil completely separating from the stationary surface.

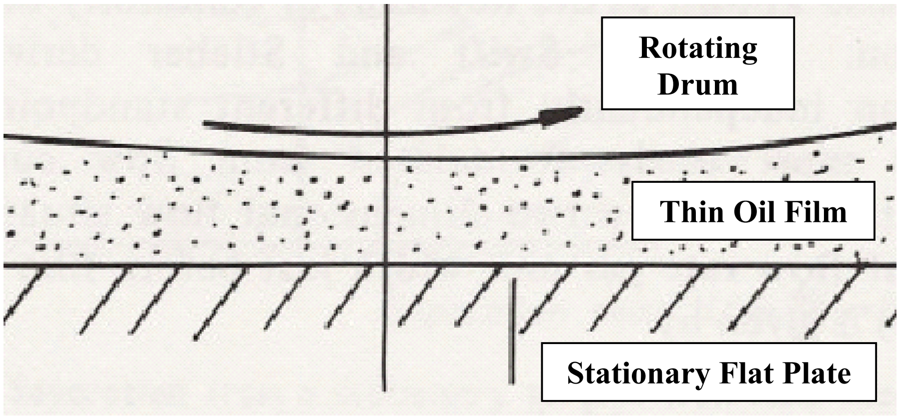

Figure 1-1. Experimental setup for rotating drum over flat plate [1.4].

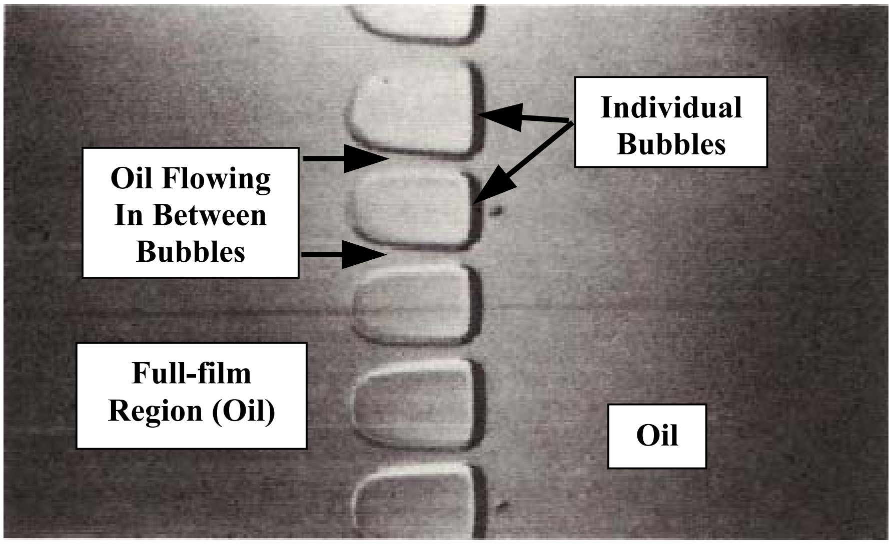

Figure 1-2. Cavitation pattern at slower speed with oil flowing in between individual bubbles [1.4].

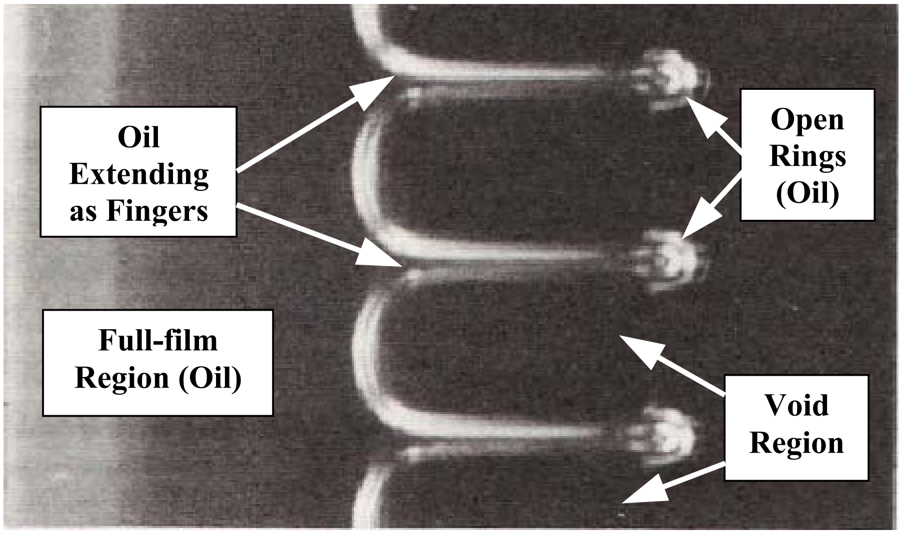

Figure 1-3. Cavitation pattern at moderate speed with comb-like appearance [1.4].

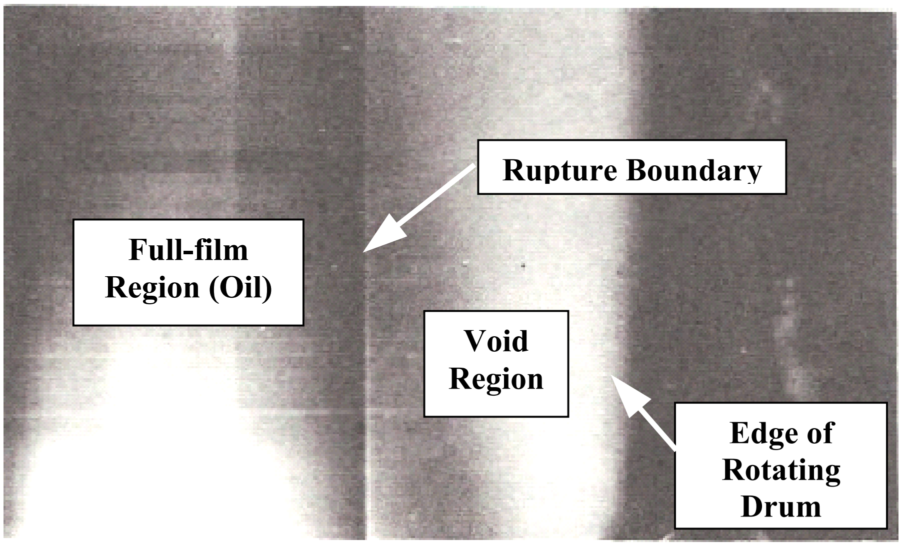

Figure 1-4. Cavitation pattern at higher speed consisting of single sheet [1.4].

Swift [1.6] and Stieber [1.7] independently suggested a boundary condition (often referred to as the Reynolds boundary condition) that upon reaching the boundary of the void, the pressure gradient should go to zero. The Swift-Stieber condition is presently recognized to be the correct boundary condition for the steady-state problem if surface tension can be neglected.

Olsson [1.9] considered the question of flow continuity between the two sides of the rupture boundary and concluded that the interface or meniscus cannot be stationary if there is a non-zero pressure gradient. In the presence of a pressure gradient depending on the manner fluid is transported, the rupture meniscus would advance in the direction of the local Poiseuille flow. This was interpreted as a stability issue of the Gumbel solution. The present work aims to make use of the rupture boundary continuity formula of Olsson to derive the time-dependent evolution that satisfies the Swift-Stieber condition. The single sheet pattern (Figure 1-4) will be the model to guide relevant analytical derivations.

1.5.3 Film Separation and Adhered Fluid

Coyne and Elrod [1.10, 1.11] considered the role of surface tension in the rupture meniscus that separates the lubricating film from the void. Flow downstream of the rupture meniscus is modeled as a viscous fluid that adheres only on the sliding surface and is connected to the stationary surface through the rupture meniscus. Thus the concept of a half-void, with an adhered viscous film on the sliding surface is described for the first time. Floberg [1.12] extended the idea of partial film separation to include fluid transport streamers. Emphasizing the case of an enclosed void, Floberg associated the streamer structure to the "tensile strength" of the fluid. Crosby [1.13] advocates a model that is equivalent to that of Floberg in the asymptotic limit of infinitely many streamers. Pan [1.14] re-examined the Olsson problem assuming the model of a half-void with an adhered film. He interpreted the Olsson equation as a formula for the trans-meniscus flow and formulated a hyperbolic type scheme for computation that would result in the Swift-Stieber condition upon reaching steady-state; no computed example was furnished.

Cole and Hughes [1.15] provided photographic evidence of the streamer-like flow structure. Etsion and Pinkus [1.16] published a study of finite length bearings with the ruptured region vented to ambient, with photographic views of both upstream and downstream boundaries of the ruptured region. Heshmat [1.17] discussed various features of the rupture film based on temperature measurements and observations of a transparent bearing. San Andres and Diaz [1.18] performed an experimental study of rupture film in squeeze film dampers.

1.5.4 Elrod Algorithm

With the advent of the digital computer, more complex numerical analysis in bearing lubrication became practical. Elrod and Adams [1.19] proposed an algorithm employing a switch function to handle both the full-film and cavitated regions with a pseudo-compressibility concept; finite difference computation of the one-dimensional problem was furnished to illustrate the method. Elrod [1.20] added a refinement to the Elrod-Adams algorithm, featuring the ADI technique for time-domain two-dimensional simulation of rupture in the bearing film. The latter version is now known as the Elrod cavitation algorithm.

The Elrod cavitation algorithm has gained wide-spread acceptance. Some researchers simply made use of the method to solve particular problems, others adapted portions of the technique, added refinements, still others developed their own algorithm using the same basic concepts; e.g., Bayada [1.21], Bayada et al. [1.22], Woods and

Brewe [1.23], Vijayaraghavan and Keith [1.24], Kumar and Booker [1.25], Claro, Miranda [1.26], Yu and Keith [1.27] – the roster is still growing.

Regardless of its popular acceptance, the Elrod algorithm is deficient in not treating the Olsson equation with reference to its dependence on the morphology model for the ruptured region; thus it has indirectly inspired the present work. Further discussion can be found in Appendix B.

1.6 Significance of Work

The computational method employed in this work presents the following two important features that are different from conventional methods:

1. *Derived Compact Reynolds Integral.* An exact one-dimensional integral of Reynolds equation is developed that contains a single invariant to define the entire solution profile (pressure). Being compact, but complete (one-dimensional), such a solution is information rich and invites creative interpretation from the user.
2. *Computed Two-Phase Morphology*. The Olsson equation can be "precisely" examined at both terminal points rendering information regarding the meniscus movement at the rupture boundary and the makeup flux at the fixed supply groove or formation boundary. Knowledge of details at the boundaries is accomplished by full (temporal) description of the two-phase flow morphology hitherto not understood.

The new method can readily be extended to two dimensions, offering the dual possibility of computation efficiency and improved description of cavitation at both steady-state and time-dependent conditions.

2. Problem Statement and Formulation

2.1 Journal Bearing Configuration and Description of the Half-void

The Reynolds equation is applicable to a fluid film that fills the gap of journal bearing, consisting of a rigid, rotating journal located inside a rigid, stationary bushing as shown in Figure 2-1. The journal with center O_J is maintained at a constant eccentricity e from the bushing with center O_B. The long bearing case with no side leakage is considered as a one-dimensional investigation in the circumferential direction θ. The line of centers, drawn through O_B and O_J and indicated by the y-axis, marks where $\theta = 0$, which is also the location of the maximum film thickness h_{max}. The location of h_{min} is given by $\theta = 180°$. The orientation of the line of centers from the load vector W is given by the attitude angle γ, where W represents the magnitude of the resulting force from the fluid pressure on the bearing. The journal speed U is given by ωR where ω is the constant angular speed and R is the journal radius.

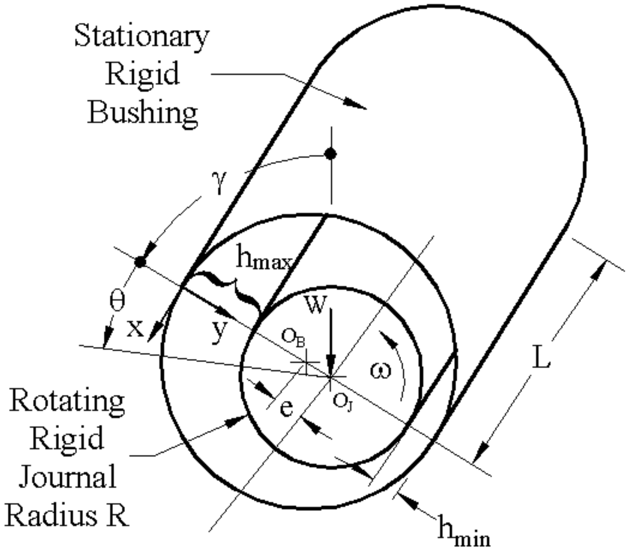

Figure 2-1. Journal bearing geometry and coordinate system.

The half-void problem, as shown in Figure 2-2 for three different times, supposes that the bearing circumference is initially divided into a full-film region containing fluid and a void-dominated (or void) region where any volume not occupied by fluid is filled with air at ambient pressure. A supply groove is located at an arbitrarily chosen formation point θ_{form} and serves to fix the starting location of the full-film region. The rupture point θ_{rup}, which marks the end of the full-film region, coincides with h_{min} ($\theta_{rup} = 180°$) at time T = 0, and moves towards the steady-state value θ_{SS} as T progresses. The full-film extent is $\theta_{form} \leq \theta \leq \theta_{rup}$.

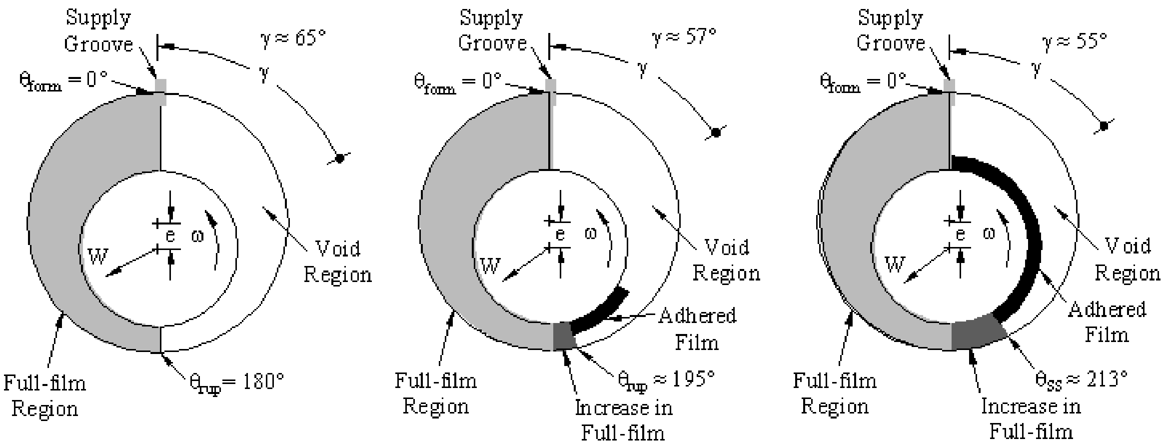

T = 0 T =60 T = T_{SS}

Figure 2-2. Temporal development for θ_{form} = 0° at times T = 0, T = 60 and T = T_{SS}.

The void region is initially dry, meaning the bearing gap being completely filled with air. Because the viscosity of lubricating oil (~1.9 $^{kg}/_{m \cdot s}$) is much larger than that of air (1.8×10^{-5} $^{kg}/_{m \cdot s}$), the void can be assumed to be isobaric at the ambient pressure and shear imparted to the adhered film can be neglected. The adhered film will continue to advance until it reaches θ_{form}, where it will re-supply the full-film, thereby reducing the feed required through the supply groove. For the special case of $\theta_{form} = 0°$, the bearing is initially half filled with fluid.

The Reynolds equation is applicable to the full-film region where the film pressure is above ambient between the terminal points. Transition of flow between the full-film region and the void-dominated region, at either θ_{form} or θ_{rup}, takes place across a meniscus transition distance in which surface tension plays a significant role and is of the same order as the bearing gap. The morphology of a cavitated liquid film is quite complicated [2.1]; here, details of the meniscus transition are neglected. The full-film is connected to a single-sided adhered film entirely at ambient pressure.

An unwrapped journal bearing is shown in Figure 2-3 to highlight the effect of supply groove location on the film thickness profile $h(\varepsilon, \theta)$. Depending on the chosen θ_{form}, the sliding surface is passing over a different profile h with different resulting pressure profiles and fluid flows expected for each case. Figures 2-4 and 2-5 show the half-void problem for three different times for cases where $\theta_{form} = -20°$ and 20°, respectively. For all cases, the initial rupture boundary is at $\theta_{rup} = 180°$ (h_{min}); the corresponding full-film region is more than a half-circle for $\theta_{form} = -20°$ and is less than a half-circle for $\theta_{form} = 20°$.

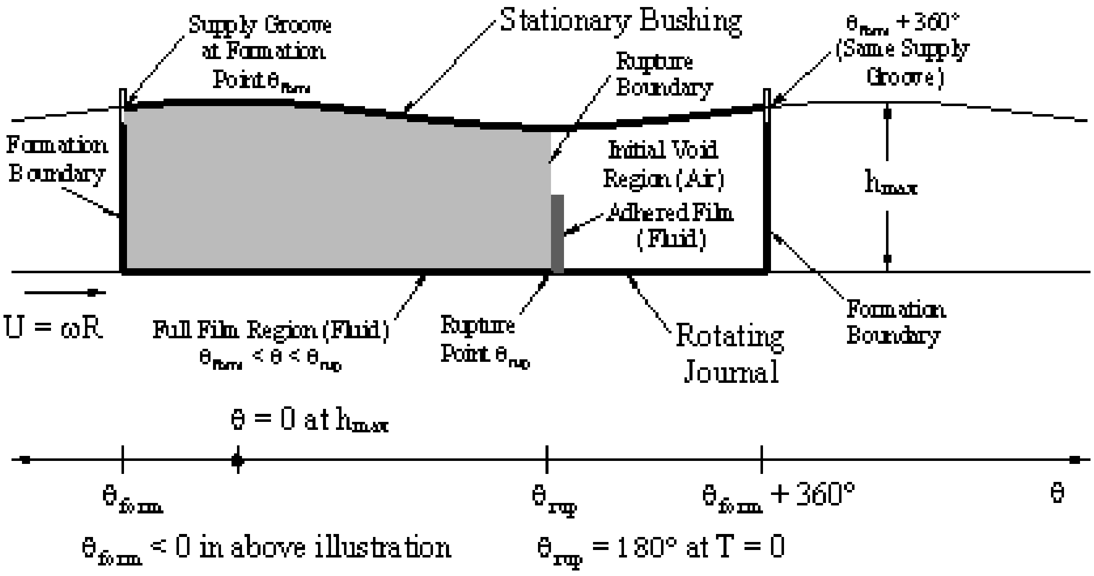

Figure 2-3. Unwrapped bearing in θ direction showing full-film and void regions (not to scale).

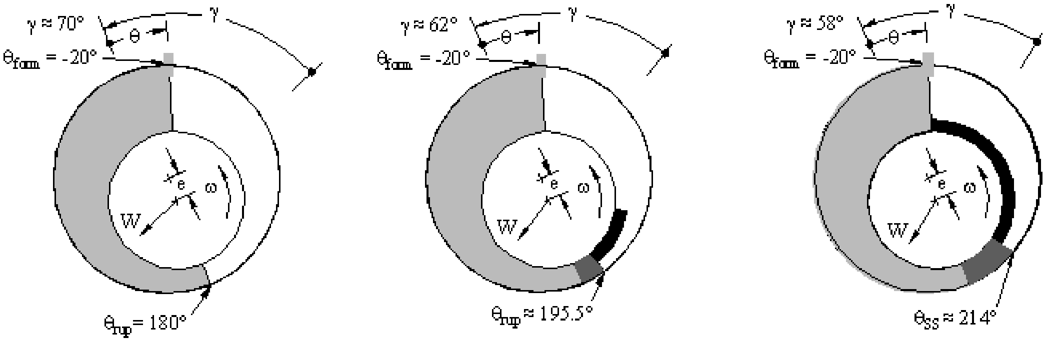

T = 0

T = 60

T = T_{SS}

Figure 2-4. Temporal development for θ_{form} = -20° at T = 0, T = 60 and T = T_{SS}.

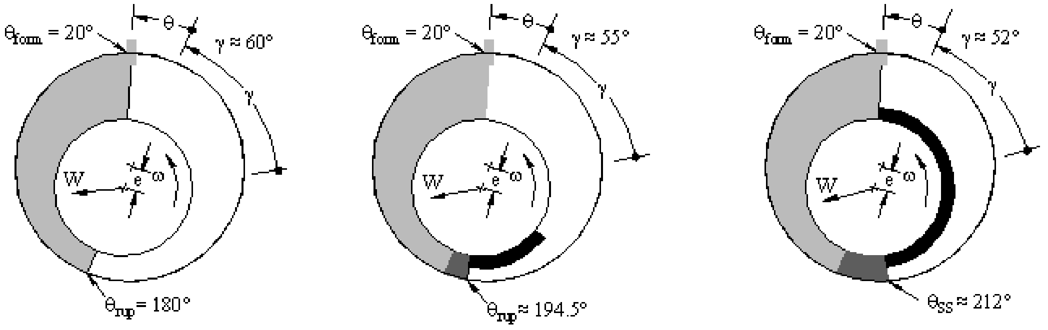

T = 0 T = 60 T = T_{SS}

Figure 2-5. Temporal development for θ_{form} = 20° at T = 0, T = 60 and T = T_{SS}.

2.2 Full-film Region: Reynolds Equation

Fluid film lubrication theory (of Reynolds) is reduced from the Navier-Stokes equations upon stipulating thin film, low Reynolds number flow between impermeable walls of an iso-viscous Newtonian lubricating liquid. It presents three basic concepts:

- Pressure is uniform across the bearing gap.
- The film velocity field within the bearing gap is the vector sum of two components – the Couette velocity is a linear interpolation between the sliding velocities of the walls that satisfies the non-slip condition of a viscous fluid and the Poiseuille velocity is pressure driven (with a parabolic profile) directed against the local pressure gradient.
- Flow continuity is maintained amongst the divergence of the film velocity fluxes, squeeze displacement and surface permeance.

Using vector notation viewed in the mean surface of the bearing film, the governing equations of the fluid film lubrication theory comprise the (Reynolds) flux law

$$\vec{\phi} = \vec{\phi}_{\text{Couette}} + \vec{\phi}_{\text{Poiseuille}} = \left(\vec{U}_{\text{lower}} + \vec{U}_{\text{upper}}\right)\frac{h}{2} - \frac{h^3}{12\mu}\vec{\nabla}p \qquad (2\text{-}1)$$

and the continuity condition (for a liquid film)

$$\vec{\nabla}\cdot\vec{\phi} + \vec{\phi}_{\text{permeance}} + \frac{\partial h}{\partial t} = 0 \qquad (2\text{-}2)$$

where $\vec{\phi}$ is the film flux vector, $\vec{U}$ (as subscripted) is the wall sliding velocity, h is the film thickness, μ is the viscosity, $\vec{\nabla}$ is the two-dimensional gradient operator of the mean film surface, $\phi_{\text{permeance}}$ the combined permeance flux through both walls, t is time and p is the fluid pressure. For the present interest, a journal bearing ($h = C + e\cos\theta$) with impermeable walls, Equations (2-1) and (2-2) are simplified to

$$\vec{\phi}_{\text{Couette}} = U_{\text{entrainment}} h\vec{i} \qquad (2\text{-}3)$$

$$\vec{\phi}_{\text{Poiseuille}} = -\frac{h^3}{12\mu}\left(\frac{\partial p}{\partial x}\vec{i} + \frac{\partial p}{\partial z}\vec{k}\right) \qquad (2\text{-}4)$$

$$\frac{\partial}{\partial x}\left(\frac{Uh}{2} - \frac{h^3}{\mu}\frac{\partial p}{\partial x}\right) + \frac{\partial}{\partial z}\left(\frac{h^3}{\mu}\frac{\partial p}{\partial z}\right) + \frac{\partial h}{\partial t} = 0 \qquad (2\text{-}5)$$

where $\left(\vec{i},\vec{k}\right)$ are unit vectors in the circumferential and axial directions, respectively, (x,z) are corresponding Cartesian coordinates, and $U_{\text{entrainment}} \equiv 2U$ is the entrainment velocity. With a time-independent eccentricity, the squeeze term $\left(\frac{\partial h}{\partial t}\right)$ drops out and the formula for a journal bearing at fixed eccentricity is obtained

$$\frac{\partial}{\partial x}\left(\frac{Uh}{2}-\frac{h^3}{\mu}\frac{\partial p}{\partial x}\right)+\frac{\partial}{\partial z}\left(\frac{h^3}{\mu}\frac{\partial p}{\partial z}\right)=0 \tag{2-6}$$

The classical Sommerfeld solution for a long bearing is obtained from Equation (2-6) by neglecting the axial pressure gradient term $\left(\frac{\partial p}{\partial z}\right)$. The Ocvirk solution [2.2] (short bearing) can be obtained by dropping the circumferential pressure gradient term $\left(\frac{\partial p}{\partial x}\right)$ (see Appendix A.2).

Equation (2-1), rewritten as the flux law of a one-dimensional problem with a time-independent gap in journal bearing coordinates, would serve as the starting point of the present work:

$$\phi=\frac{Uh}{2}-\frac{h^3}{12\mu}\frac{\partial p}{\partial x} \tag{2-7}$$

Note that the partial differentiation notation is retained, even though h is assumed to be time-independent, in anticipation of time-dependence to be introduced by Olsson's equation. Normalizing (h, x, ϕ) with (C, R, $\frac{UC}{2}$), respectively, and defining $P=\frac{(p-p_a)C^2}{6\mu UR}$, the normalized flux law is obtained:

$$H_0=\frac{2\phi}{UC}=H-H^3\frac{\partial P}{\partial\theta} \tag{2-8}$$

where $H = 1 + \varepsilon \cos\theta$. A general solution of Equation (2-8) is

$$P = P_0 + J_2(\theta, \theta_0) - H_0 J_3(\theta, \theta_0) \tag{2-9}$$

$$J_n(\theta, \theta_0) \equiv \int_{\theta_0}^{\theta} H^{-n} d\theta \tag{2-10}$$

where θ_0 is a suitable lower limit of integration and $P_0 \equiv P(\theta_0)$. Closed form formulas can be written for J_n. Equation (2-9) can be used to generate the pressure profile for any suitable range of θ.

Since Equation (2-8) is applicable in the full-film region where $P \geq 0$, the pressure gradient must be positive at θ_{form}, but negative at θ_{rup}, consequently[1]

$$H_{form} \geq H_0 \geq H_{rup} \tag{2-11}$$

This observation restricts the possible location of the rupture point to where the film thickness at rupture H_{rup} is less than that at formation H_{form}.

2.3 Generalized Gumbel Solution

The lower limit of integration in Equation (2-9) is arbitrary; setting P_0 to zero makes θ_0 an ambient boundary. H_0 can then be calculated upon identifying the upper limit and the corresponding pressure. For the generalized Gumbel problem, θ_0 is θ_{form}

---

[1] This inequality is violated by the classical Sommerfeld solution that corresponds to ($\theta_{form} = 0$, $\theta_{rup} = 180°$) or ($H_{form} = H_{rup} = H_{max}$); sub-ambient pressure is featured in the span ($180° < \theta_{rup} < 360°$). The half-Sommerfeld solution, ($\theta_{form} = 0$, $\theta_{rup} = 180°$), however, is entirely above-ambient and is a special case of the Gumbel solution.

and the upper limit is θ_{rup}. By requiring $P_{rup} = 0$, one determines

$$H_0 = \frac{J_2(\theta_{rup}, \theta_{form})}{J_3(\theta_{rup}, \theta_{form})} = \frac{\displaystyle\int_{\theta_{form}}^{\theta_{rup}} \frac{d\theta}{(1+\varepsilon\cos\theta)^2}}{\displaystyle\int_{\theta_{form}}^{\theta_{rup}} \frac{d\theta}{(1+\varepsilon\cos\theta)^3}} \tag{2-12}$$

Equation (2-10) shows that H_0 is the film thickness at the location of a pressure extremum. If the inequality given by Equation (2-11) is in effect, θ_0 would be the location of peak pressure. The full Sommerfeld condition is obtained with $\theta_{form} = 0°$ and $\theta_{form} = 360°$ and the half-Sommerfeld solution is obtained with $\theta_{form} = 0°$ and $\theta_{form} = 180°$. Because $J_n(180°, 0°)$ is exactly one half of $J_n(360°, 0°)$, H_0 of the half-Sommerfeld and Sommerfeld solutions are identical.

Upon finding H_0, the complete pressure profile can be constructed with Equation (2-9). One can also use Equation (2-8) to find, at any $\theta_{form} \le \theta \le \theta_{rup}$

$$\frac{\partial P}{\partial \theta} = \frac{1}{H^2}\left(1 - \frac{H_0}{H}\right) \tag{2-13}$$

2.4 Swift-Stieber Steady-state Rupture Boundary Condition

For any given θ_{form}, the Swift-Stieber condition stipulates the existence of a steady-state rupture location θ_{SS}, which is to be determined, where pressure and its gradient vanish simultaneously

$$\left.\frac{\partial P}{\partial \theta}\right|_{SS} = 0,\ P(\theta_{SS}) \text{ at } \theta_{SS} \tag{2-14}$$

θ_{SS} is determined by an iterative, narrowing search for where $\left.\frac{\partial P}{\partial \theta}\right|_{rup}$ changes sign from negative to positive (see Appendix C).

The half-void problem will focus on the transition in time from the half-Sommerfeld condition to the Swift-Stieber condition, both of which are illustrated in terms of pressure profiles in Figure 2-6. The starting point θ_{rup} for the time-dependent analysis was chosen to be at 180° (the minimum gap) for two reasons. First, historically, the use of the half-Sommerfeld solution as an approximation for obtaining performance parameters makes data available for comparison. Second, and most important, a bearing in practice will operate normally near steady-state. Any disturbance from steady-state (change in eccentricity, pressure or flow) will result in an intermediate state that is unsteady and the fluid flow inside the bearing will react as to re-establish equilibrium. It is unlikely that a bearing will be disturbed past an intermediate state of $\theta_{rup} = 180°$, so only cases where $\theta_{rup} \geq 180°$ are considered. How quickly the fluid returns to equilibrium will be determined in applying Olsson's equation to both terminal points of the full-film.

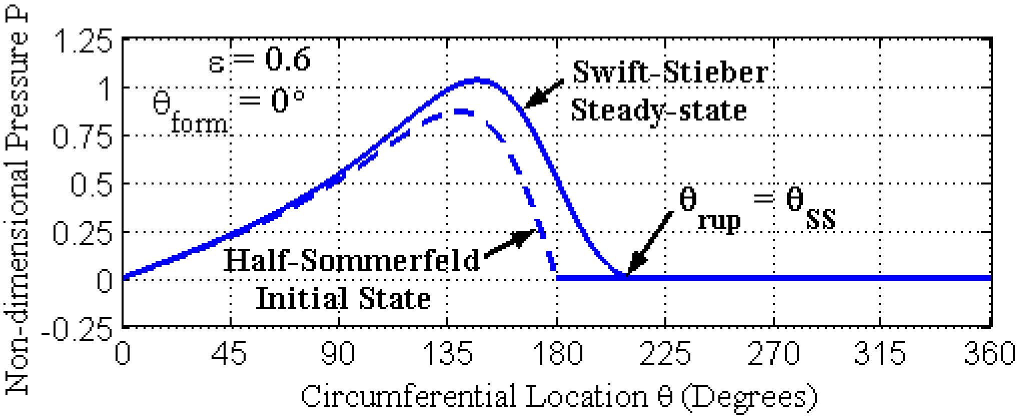

Figure 2-6. Pressure profiles for initial and final Gumbel states.

2.5 Meniscus Boundaries: Olsson Equation

2.5.1 Rupture Point θ_{rup}

Olsson [2.6] pointed out that flow continuity at the rupture point requires allowance for a non-vanishing meniscus speed U_{rup}. The one-dimensional journal bearing flux law has been previously stated by Equation (2-2). The full-film flux $\phi = \frac{UCH_0}{2}$ is invariant with respect to θ for a time-independent film thickness. Across the rupture point, flow is transformed into a single-side adhered film $H_a = h_a/C$ that has the equivalent flux of

$$\phi_a = UCH_a \tag{2-13}$$

which is not the same as the full-film flux, so that the meniscus is allowed to move at U_{rup} to fill the remaining space. In order to ensure that the flow balance is satisfied

$$\phi_{rup} = \phi_a + \phi_{void} = UCH_a + U_{rup}C\left(H_{rup} - H_a\right) \tag{2-14}$$

as illustrated in Figure 2-3 where ϕ_a and ϕ_{void} are the adhered film flow and the resulting filling flow of the moving meniscus, respectively. Substituting the left-hand side with the Couette and Poiseuille components of the film flux and dividing by C, one finds

$$\frac{UH_{rup}}{2} - \frac{UH_{rup}^3}{2}\left(\frac{dP}{d\theta}\right)_{rup} = UH_a + U_{rup}\left(H_{rup} - H_a\right) \tag{2-15}$$

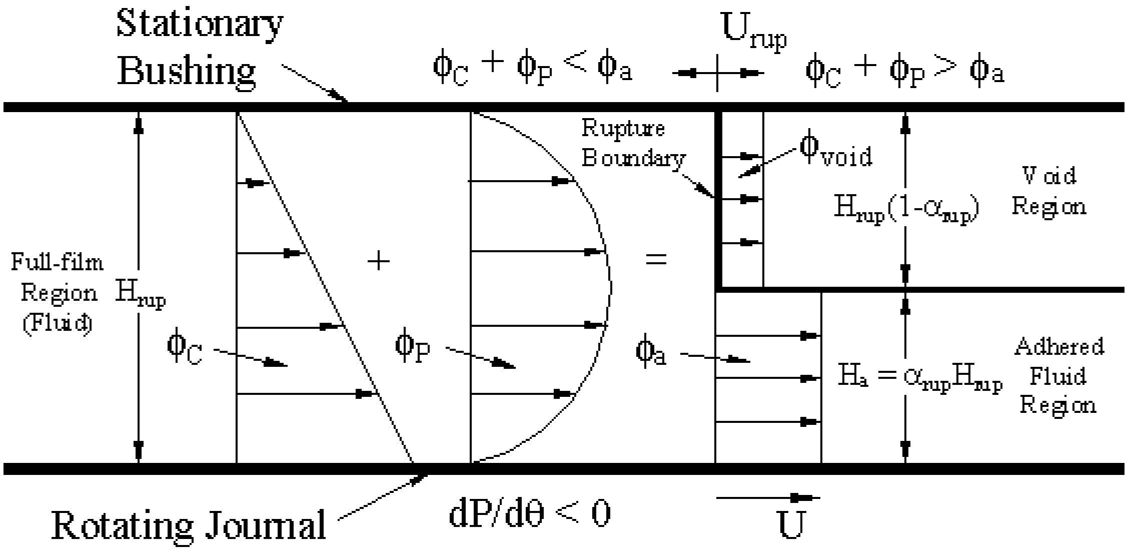

Figure 2-7. Olsson equation applied at the rupture boundary θ_{rup}.

Introducing $\alpha_{rup} = H_a / H_{rup}$ as the fractional film content with $0 \leq \alpha_{rup} \leq 1$ gives

$$\frac{UH_{rup}}{2}-\frac{UH_{rup}^3}{2}\left(\frac{dP}{d\theta}\right)_{rup}=U\alpha_{rup}H_{rup}+U_{rup}H_{rup}(1-\alpha_{rup}) \tag{2-16}$$

Solving for the rupture speed

$$U_{rup}=\frac{U}{2(1-\alpha_{rup})}\left[(1-2\alpha_{rup})-H_{rup}^2\left(\frac{dP}{d\theta}\right)_{rup}\right] \tag{2-17}$$

Equation (2-17) shows that for the rupture point to possess a steady-state, not only the pressure gradient must be zero according to Swift and Stieber, the first term of the right-hand side must also vanish, rendering

$$\alpha_{rup}=\frac{1}{2} \tag{2-18}$$

This means that if fluid is to move ahead of the meniscus, becoming adhered only to the moving journal surface, its height should become halved. Implied in this conclusion is the conservation of fluid mass while the momentum associated with the velocity profile plays no role in the trans-meniscus flow process. The latter idea is consistent with the low Reynolds number thin film approximation of lubrication theory. Therefore, Equation (2-18) can be regarded as a hypothesis of creeping trans-meniscus flow or creep for short and should remain valid even when $U_{rup} \neq 0$. The meniscus speed can be calculated by substituting Equation (2-18) into Equation (2-17) to obtain

$$U_{rup} = -UH_{rup}^{2}\left(\frac{dP}{d\theta}\right)_{rup} \tag{2-19}$$

The direction of U_{rup} is always downstream for the half-void problem since the pressure gradient at rupture is negative. Substituting for $\left(\frac{dP}{d\theta}\right)_{rup}$ from Equation (2-12) shows the dependence of U_{rup} on H_0.

$$U_{rup} = U\left(\frac{H_0}{H_{rup}} - 1\right) \tag{2-20}$$

The condition $U_{rup} = 0$ corresponds to when $H_0 = H_{rup}$ which occurs when $H_0 = H_{SS}$, which is the Swift-Stieber steady-state flux.

2.5.2 Formation Point θ_{form}

Olsson's equation can also be applied at the formation point:

$$UH_{a,form} + U_{form}\left(H_{form} - H_{a,form}\right) = \frac{UH_{form}}{2} - \frac{UH_{form}^{3}}{2}\left(\frac{dP}{d\theta}\right)_{form} \tag{2-21}$$

The formation boundary θ_{form} is fixed by means of a supply groove, as shown in Figure 2-8, which is connected to an ambient level reservoir. Thus, in lieu of a moving meniscus U_{form}, flow is added or removed through the supply groove in the form of a makeup flux (divided here by the clearance C):

$$\frac{\phi_m}{C} = U_{form}\left(H_{form} - H_{a,form}\right) = \frac{\phi_{form} - \phi_{a,form}}{C} = \frac{UH_0}{2} - UH_{a,form} \tag{2-22}$$

where H_0 is the non-dimensional flux of the full-film region given by Equation (2-12), $H_{a,form}$ is the single-side adhered film thickness that has been carried to θ_{form} by the moving journal surface and H_{form} is the non-dimensional film thickness at formation. The non-dimensional makeup flux is then

$$H_m = \frac{2\phi_m}{UC} = H_0 - 2H_{a,form} \tag{2-23}$$

with the convention that H_m is positive with flow into the bearing gap with flow drainage occurring when $H_m < 0$ and flow makeup occurring when $H_m > 0$[2].

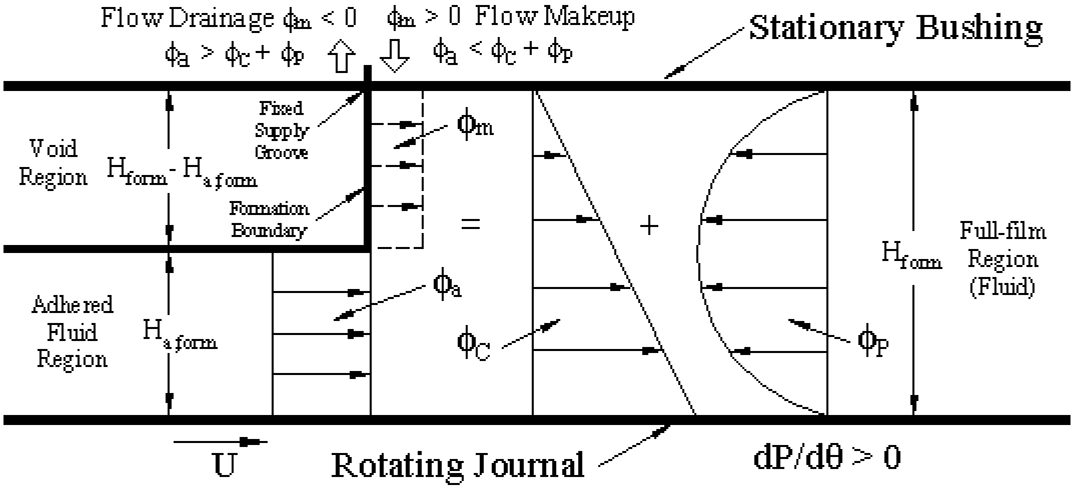

Figure 2-8. Olsson equation applied at the formation boundary θ_{form}.

---

[2] If θ_{form} is not fixed (no supply groove), then, from Equation (2-22), the formation point would move at $\frac{U_{form}}{U} = \left(H_{form} - H_{a,form}\right)^{-1}\left(\frac{H_0}{2} - H_{a,form}\right)$.

2.5 Bearing Performance Parameters

Through application of Olsson's equation at the terminal points as just described, a precise location of the rupture boundary can be determined, which also leads to more accurate calculations for important bearing performance parameters – the load capacity and the frictional force.

2.6.1 Load Capacity and Attitude Angle

Integral formulations are developed for the load capacity W and the attitude angle γ, which give the magnitude and direction of the resultant force to the hydrodynamic pressure. W and γ are shown in Figure 2.9 and expressions for both are given here for the general case where θ_{form} is not necessarily zero in order to be able to qualitatively describe the effect of the choice of θ_{form} on bearing performance. The formulations depend only on the pressure for the full-film extent; the cavitation zone makes no contribution since the pressure there is assumed ambient (P = 0). The components of W in the tangential (W_x) and radial (W_y) directions are found by integrating the effect of pressure over the entire applied area of the full-film given by

$$W_x = LR \int_{\theta_{form}}^{\theta_{rup}} P \sin\theta d\theta \qquad (2\text{-}24)$$

$$W_y = -LR \int_{\theta_{form}}^{\theta_{rup}} P \cos\theta d\theta \qquad (2\text{-}25)$$

where L is the length of the bearing and R is the radius. By convention W_x is chosen in the same direction as the journal rotation ω and W_y in the direction from the bushing to journal center.

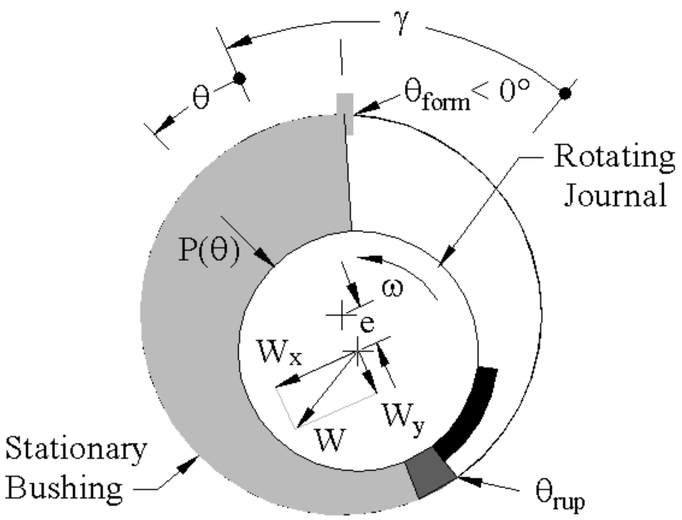

Figure 2-9. Bearing showing load vector and components.

The magnitude of the load capacity is the resultant of the two components

$$W = \sqrt{W_x^2 + W_y^2} \tag{2-26}$$

The attitude angle is given by

$$\tan\gamma = \frac{W_x}{W_y} \tag{2-27}$$

In calculating W_x and W_y, it is unnecessary to integrate the pressure profile if integration by parts is used on Equations (2-24) and (2-25) yielding

$$W_x = LR\left(-P\sin\theta\Big]_{\theta_{form}}^{\theta_{rup}} + \int_{\theta_{form}}^{\theta_{rup}} \frac{dP}{d\theta}\sin\theta d\theta \right) \tag{2-28}$$

$$W_y = LR\left(-P\cos\theta\Big]_{\theta_{form}}^{\theta_{rup}} + \int_{\theta_{form}}^{\theta_{rup}} \frac{dP}{d\theta}\cos\theta d\theta \right) \tag{2-29}$$

Since the flux is invariant, the pressure gradient is found from Equation (2-12)

$$\frac{dP}{d\theta} = \frac{1}{H^2} - \frac{H_0}{H^3} \tag{2-30}$$

Substituting this into the two load capacity components and recognizing that P(θ_{form}) and P(θ_{rup}) are both zero leaves

$$W_x = LR\left(\int_{\theta_{form}}^{\theta_{rup}} \frac{\sin\theta d\theta}{(1+\varepsilon\cos\theta)^2} - H_0 \int_{\theta_{form}}^{\theta_{rup}} \frac{\sin\theta d\theta}{(1+\varepsilon\cos\theta)^3} \right) \tag{2-31}$$

$$W_y = LR\left(\int_{\theta_{form}}^{\theta_{rup}} \frac{\cos\theta d\theta}{(1+\varepsilon\cos\theta)^2} - H_0 \int_{\theta_{form}}^{\theta_{rup}} \frac{\cos\theta d\theta}{(1+\varepsilon\cos\theta)^3} \right) \tag{2-32}$$

Evaluating the integrals in x-component:

$$\frac{W_x}{LR} = \frac{1}{\varepsilon}\left[\frac{1}{H} - \frac{H_0}{2H^2} \right]_{\theta_{form}}^{\theta_{rup}} \tag{2-33}$$

Taken from a table of integrals [2.7], the integrals associated with W_y turn out to be functions of the J_n integrals given by Equation (2-10) used to calculate the non-dimensional flux H_0 and pressure P:

$$I_n = \int \frac{\cos x dx}{(1+\varepsilon\cos x)^n} = -\frac{1}{\varepsilon}\int \frac{dx}{(1+\varepsilon\cos x)^n} + \frac{1}{\varepsilon}\int \frac{dx}{(1+\varepsilon\cos x)^{n-1}} = \frac{1}{\varepsilon}(J_{n-1} - J_n) \tag{2-34}$$

This leaves the bearing load in the y-direction in compact form where J_1, J_2 and J_3 are all evaluated with the limits of the full-film θ_{form} and θ_{rup}:

$$\frac{W_y}{LR} = (I_2 - H_0 I_3) = \frac{1}{\varepsilon}\left[(J_1 - J_2) - H_0(J_2 - J_3)\right]_{\theta_{form}}^{\theta_{rup}} \tag{2-35}$$

Although, the definition of the load involves an integral of the pressure over the whole bearing, very little extra computational effort is required beyond calculating H_0.

2.6.2 Frictional Force

Similar to the load capacity W, another bearing design parameter, the non-dimensional friction force F_f can also be derived for an expression obtained with little extra computation once H_0 is found. $\hat{F}_f$ is the force of resistance due to fluid shear required to drag the fluid along with the journal given by

$$\hat{F}_f = LR\int_{\theta_{form}}^{\theta_{rup}} \tau_w d\theta \tag{2-36}$$

where $\tau_w = \mu \left.\frac{du}{dy}\right|_{(y=h)}$ is the shear stress of the fluid at the wall [2.8]. $\hat{F}_f$ opposes the direction of journal rotation. The limits for calculating the frictional force are the terminal points of the full-film, since, with the presence of cavitation, only air is sheared in the void region, and this has a negligible contribution due to the much smaller value of air viscosity compared to that of oil. Figure 2-10 is given here as a reminder of the velocity profiles involved in the full-film region. This leads to a non-dimensional expression for the friction force in terms of the same J_n integrals:

$$F_f = \frac{\hat{F}_f}{RL} = \left(\frac{C}{\mu URL}\right)\int_{\theta_{form}}^{\theta_{rup}} \tau_w d\theta = \left(4J_1 - 3\frac{J_2^2}{J_3}\right)_{\theta_{form}}^{\theta_{rup}} \tag{2-37}$$

It is intended by the notation that the J_n integrals be evaluated with a lower limit of θ_{form} and an upper limit of θ_{rup}.

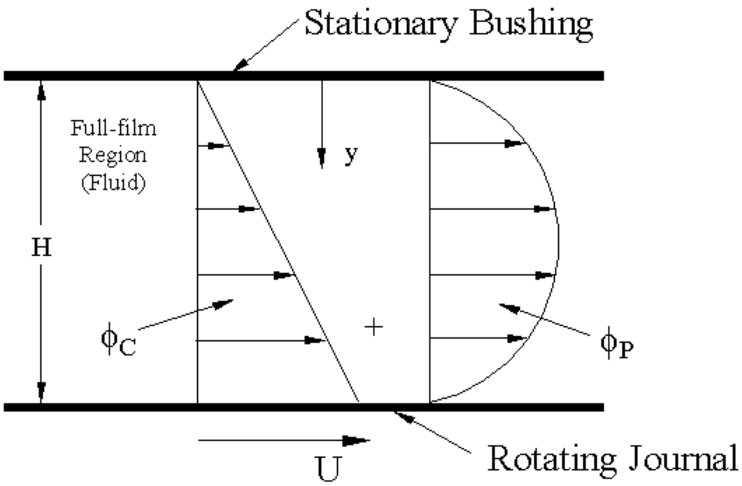

Figure 2-10. Velocity profile used to calculate shear stress.

2.7 Summary of Assumptions

The major assumptions used throughout this work are provided here and divided into the following four categories: Geometrical Considerations, Full-film Region (Reynolds Equation), Rupture Boundary (Olsson's Equation) and Partial-film Region (Adhered Film and Void Regions).

- **Geometrical Considerations**
  - *Long Bearing.* The ratio of the journal length to diameter is at least 2 and there is no flow in the axial direction.
  - *Constant Eccentricity.* The center of the journal is offset from, but does not translate in relation to the bushing center.
  - *Negligible Bearing Curvature Effects.* The radius R is much larger than the film thickness and hence $H = 1 + \varepsilon \cos \theta$.

- **Full-film Region (Reynolds Equation)**
  - *Thin Film.* The velocity gradients along the film (du/dx) are negligible relative to across the film thickness (du/dy). Two consequences of this assumption:
    - *Constant Pressure across the Full-film.* The pressure p does not vary in the y-direction.
    - *Negligible Gravity.* The acceleration of the fluid due to gravity is negligible in comparison to the viscous forces.
  - *Laminar Flow.* Flow is smooth and in layers without mixing between layers (i.e. absence of turbulence). Further, the Reynolds number Re, which is a ratio of inertial to viscous forces, is assumed to be less than 1000. This implies the effect of inertia is small when compared to the effect of viscosity. A consequence of this assumption:
    - *Newtonian Lubricant.* The shear rate as a result of an applied force is linear ($F = \mu \, du/dx$), which is implied in the Reynolds equation.
  - *Continuous Lubricant.* This allows for the pressure profile in the entire full-film region to be calculated from only the terminal points, i.e., θ_{form} and θ_{rup}.
  - *Incompressible Lubricant.* The density ρ is a constant.
  - *Constant Viscosity.* The fluid viscosity μ is not dependent on temperature.
  - *No Slip Condition.* The velocity of the fluid at both boundaries is consistent with the boundary. The fluid in contact with the moving journal travels along with the journal at a rotational speed U and fluid at the stationary bushing does not move at all. There is no boundary layer at either surface in the full-film region.

- **Rupture Boundary (Olsson's Equation)**
    - *Location of Cavitation Onset.* The rupture boundary occurs exactly at the circumferential location where the pressure is below zero.
    - *Static Meniscus Shape.* The shape of the meniscus does not change as the rupture boundary moves.

- **Partial Film Region (Adhered Film and Void Regions)**
    - *No Slip Condition.* The adhered film travels along with the journal at constant speed U and the air in the void region at the bushing remains stationary.
    - *Constant Velocity Across Adhered Film.* The velocity of the fluid does not vary in the y-direction.
    - *Void Composition is Air.* The void region is entirely filled with air, and there is no presence of a vacuum or oil vapor.
    - *Ambient Void Pressure.* The pressure everywhere in the void is equal to ambient.

3. Analytical and Numerical Implementation

3.1 Elimination of Branch Points of the Full-film Integrals

A critical step in achieving a solution to the half-void problem is to accurately evaluate the invariant non-dimensional flux H_0 for the full-film region given by Equation (2-12). From H_0, for instance, $\left(\frac{dP}{d\theta}\right)_{rup}$ from Equation (2-13) and rupture point speed U_{rup} from Equation (2-20) will follow. This requires an accurate solution to the two integrals J_2 and J_3. Exact analytical solutions would be ideal since a continuous pressure profile P given by Equation (2-8) for various choices of supply groove locations is desired. General solutions to the integrals are found in integral tables [3.1] in the following forms

$$J_2 = \left[\frac{-\varepsilon \sin\theta}{(1-\varepsilon^2)(1+\varepsilon\cos\theta)}\right]_{\theta_{form}}^{\theta_{rup}} + \frac{1}{(1-\varepsilon^2)} J_1 \tag{3-1}$$

$$J_3 = \left[\frac{-\varepsilon \sin\theta}{2(1-\varepsilon^2)(1+\varepsilon\cos\theta)^2}\right]_{\theta_{form}}^{\theta_{rup}} + \frac{3}{2(1-\varepsilon^2)} J_2 - \frac{1}{2(1-\varepsilon^2)} J_1 \tag{3-2}$$

and rely on the intermediate evaluation of a third integral

$$J_1 = \int_{\theta_{form}}^{\theta_{rup}} \frac{d\theta}{1+\varepsilon\cos\theta} = \left[\frac{2}{\sqrt{1-\varepsilon^2}} \tan^{-1}\left(\sqrt{\frac{(1-\varepsilon)}{(1+\varepsilon)}} \tan\frac{\theta}{2}\right)\right]_{\theta_{form}}^{\theta_{rup}} \tag{3-3}$$

The arc tangent function in Equation (3-3), according to accepted mathematical convention, has a branch point (in radians) at $\theta = \pi$ where it is shifted by π. Since J_1 is used here to construct a continuous pressure profile for $\theta_{form} \le \theta \le \theta_{rup}$, it is necessary to compensate for the branch condition by subtracting out π from the arc tangent function as

θ passes through π. However, if it were constructed as $J_1(\theta_{rup}; \varepsilon)$ - $J_1(\theta_{form}; \varepsilon)$, even after compensation, numerical inaccuracy can occur due to truncation error in the computation of the arc tangent function. This difficulty is removed by rewriting $J_1(\theta_{form}, \theta_{rup}; \varepsilon)$ with the aid of standard trigonometric identities to factor out the difference parameter (θ_{rup} - θ_{form}) prior to computing the arc tangent function, rendering

$$J_1 = \frac{2}{\sqrt{1-\varepsilon^2}} \operatorname{atan2}\left[\sqrt{1-\varepsilon^2}\sin\frac{(\theta_{rup}-\theta_{form})}{2},\ \cos\frac{(\theta_{rup}-\theta_{form})}{2}+\varepsilon\cos\frac{(\theta_{rup}+\theta_{form})}{2}\right] \quad (3\text{-}4)$$

In Equation (3-4), atan2 notation follows the standard four quadrant function that is continuous from $-\pi$ to π where the parenthesized parameters are (ordinate, abscissa). With the branch removed from the J_1 integral by taking advantage of the atan2 function only recently available, H_0, $\left(\frac{dP}{d\theta}\right)_{rup}$, U_{rup} and P can now be evaluated accurately and effortlessly. Because Equation (3-4) is simpler to use with arbitrary supply groove location, it is an improvement to current practice in evaluating the J_n integrals that involve use of the Sommerfeld substitution [3.2].

3.2 Gumbel Charts

Based on the numerical approach just described, for a given choice of formation location θ_{form}, H_0 for an arbitrary rupture location θ_{rup} can be determined for the general, non-periodic, Gumbel solution of the Reynolds equation. At a fixed eccentricity ε, a complete set of Gumbel solutions can be described as a contour map of the non-dimensional flux for any combination of formation and rupture locations. This contour map will form the basis for a Gumbel chart, which will be helpful in explaining the solution to the half-void problem.

A Gumbel chart for $\varepsilon = 0.6$ will be explained using Figure 3-1. For a given $-180° \le \theta_{form} \le 180°$, the appropriate range of rupture location is $\theta_{form} < \theta_{rup} \le \theta_{form}+360°$; the lower diagonal of the charts is the lower limit $\theta_{form} = \theta_{rup}$ and the upper diagonal is the Sommerfeld periodic solution. The location of the steady-state rupture point θ_{SS}, as it is dependent on θ_{form}, is indicated by the Swift-Stieber Line. In addition, the values of the steady-state fluxes H_{SS} are plotted versus θ_{form} as an attic added above the Gumbel chart.

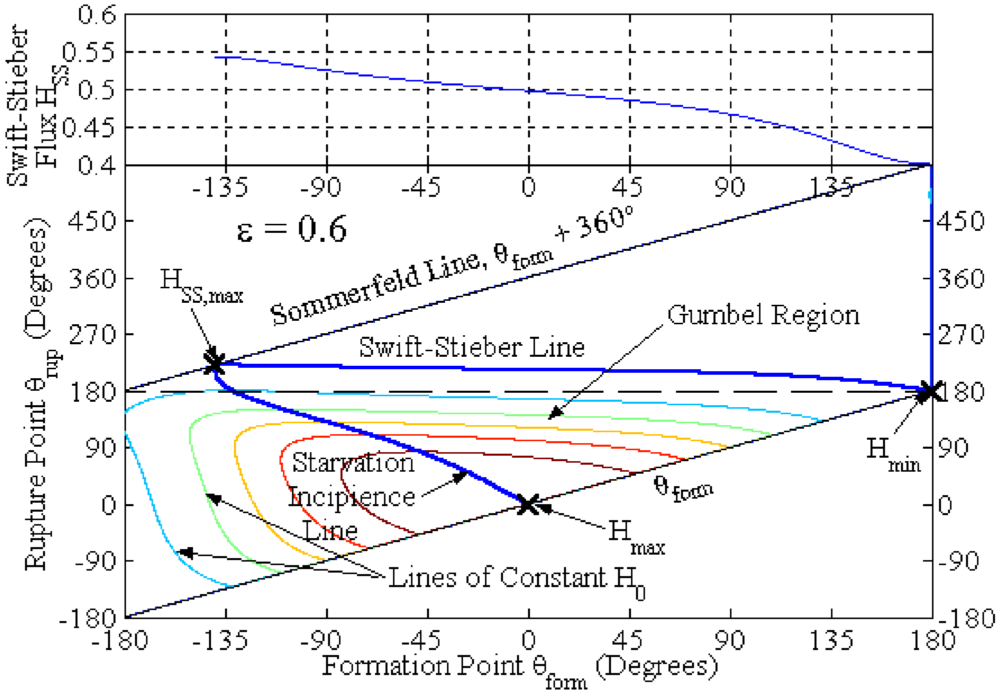

Figure 3-1. Sample Gumbel chart.

The starvation incipience line based on Equation (2-3) is placed to designate the rupture point limit below which inlet starvation occurs, i.e., where negative pressure exists just downstream of θ_{form}. The Swift-Stieber, Starvation Incipience and the lower diagonal lines define the boundaries of the Gumbel region where the interior pressures are above ambient at all locations in the full-film region. A horizontal dash-line at θ_{rup} = 180° of the ordinate, denotes the half-Sommerfeld solutions and marks the assumed initial rupture point in a study of the evolution process toward development of the final Swift-Stieber condition. Gumbel charts for three different eccentricities were constructed and can be found along with a discussion in Section 4.1.

Expanded views of the Gumbel charts for the upper Gumbel region $180° \leq \theta_{rup} \leq \theta_{SS}$ are also included in Section 4.1 for the same three values of ε to show more closely how the values of H_0 vary as θ_{rup} approaches θ_{SS}. During the evolution process, the filled portion of the bearing gap obeys an intermediate Gumbel solution between the Half-Sommerfeld Line and the Swift-Stieber Line. A sample expanded view for $\varepsilon = 0.6$ is given in Figure 3-2 and marked with X's to indicate the path taken by the rupture point for the $\theta_{form} = 0°$ case. A vertical segment of the Gumbel chart between the initial rupture and the Swift-Stieber Line is subdivided into many intermediate state points θ_{rup} with a range from $180° \leq \theta_{rup} \leq \theta_{SS}$. For clarity, only five equal distant X's are shown, but the distance between 180° and θ_{SS} is actually divided into more points for an accurate representation.

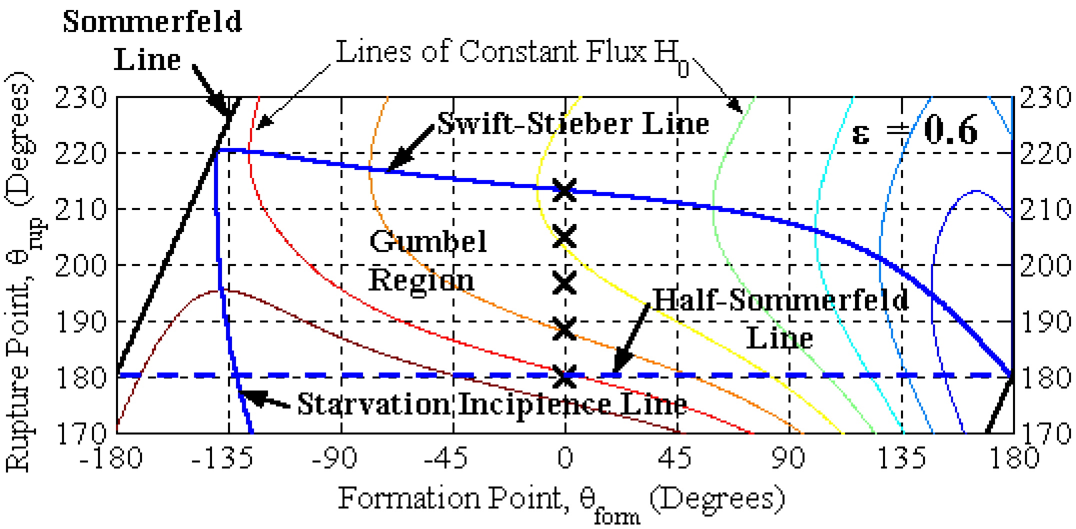

Figure 3-2. Sample expanded view of Gumbel chart.

3.3 Rupture Point Movement

At each θ_{rup}, unless $\left(\frac{dP}{d\theta}\right)_{rup}$ vanishes, as in the case of the Swift-Stieber solution, Olsson's equation would stipulate that the rupture point would move in the direction of the Poiseuille flux at a speed depending on H_0 obtained from the Reynolds equation in the full-film region beyond the current location of the rupture point. Evolution towards the Swift-Stieber condition is described by the space-time relationship of the rupture meniscus, beginning from an assumed initial Gumbel solution. Non-dimensional time T is given by θ / U, with θ being the angle that the journal has rotated in one unit of time and U = ωR is the journal surface speed. The meniscus speed U_{rup} as calculated from Olsson's equation is calculated and U_{rup}^{-1} is then integrated by the trapezoidal rule to obtain the time T to reach the intermediate state. The trapezoidal rule was chosen for simplicity over Simpson's rule or higher-order numerical integration schemes, because appreciable differences from the trapezoidal rule were not noticed except when θ_{rup} approaches θ_{SS} and U_{rup}^{-1} rises sharply and becomes unbounded.

For the purpose of animating the rupture point motion that allows not only for visualization of the rupture movement, but also for the determination the non-dimensional makeup flux H_m, the rupture location must be determined at equally spaced temporal increments from the original rupture time versus location data calculated in equally spaced spatial increments. To accomplish this, a least-squared curve fit was performed using Matlab's *polyfit* function [3.2] on the time versus rupture location curve. The best fit was determined to be a third-order polynomial of the rupture location versus the natural log of the time plot.

To help explain the rationale of the method, the curve fit is plotted along with the original data on the same axis with a coarse resolution in Figure 3-2. The original data (marked with X's) shows a spatial increment θ, which divides up the curve by placing 9 grid points evenly, spaced over the approximate 27° (from 180° to 207°) covered by the meniscus movement. The curve fit (marked with Os) shows a temporal increment T placing the same number of grid points evenly spaced in time over the approximate 2.77 units of time it takes the meniscus to cover the exact same distance. It can be noticed that the X's are not evenly spaced in time since the change in time between successive points increases. Likewise, the O's are not evenly spaced in space since the change in distance between successive points decreases.

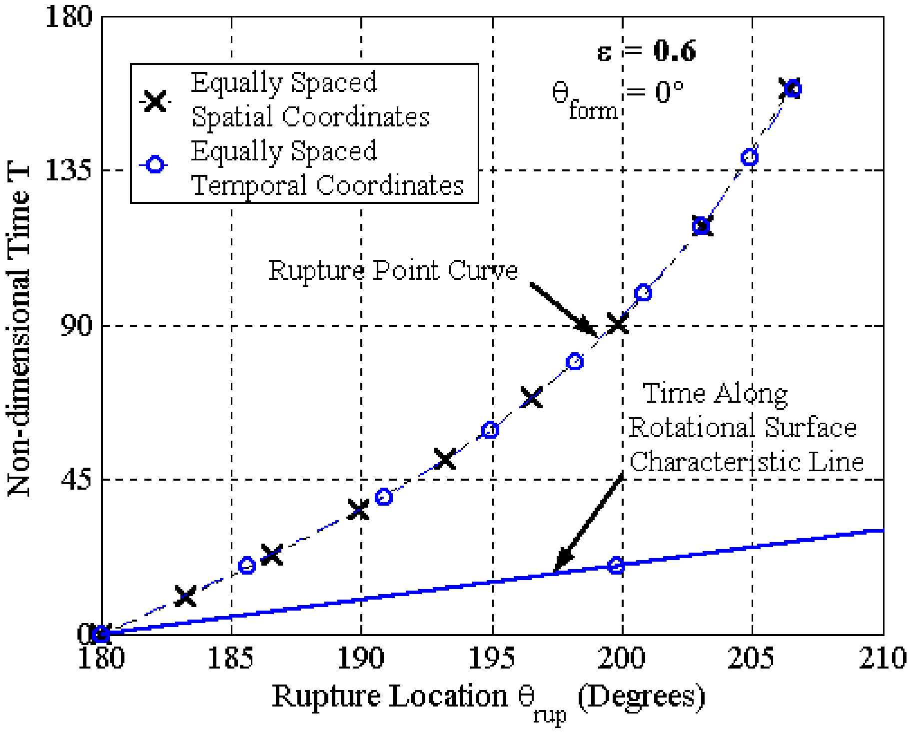

Figure 3-3. Curve fit of time to the intermediate rupture states.

3.4 Complete Half-void Solution

3.4.1 Advancing the Adhered Film

The coefficients obtained from the curve fit allow the calculation of the rupture location θ_{rup} at any time T, including evenly spaced increments of time. Attention is now turned toward flow in the void region to complete a comprehensive solution to the half-void problem. For each time increment ΔT, three flow processes occur simultaneously. First, the adhered film between θ_{rup} and θ_{form} stays with the moving journal surface rotating at angular speed $U = \frac{\Delta\theta}{\Delta T}$. For simplicity, Δθ is set to exactly to ΔT, so that U is exactly 1 degree per unit of time. The rotating surface characteristic line or the distance the adhered film travels in one time unit is also plotted on Figure 3-2 for comparison to

U_{rup}. Since the slope $\frac{dT}{d\theta}$ is greater for U_{rup} than for U, $U_{rup} < U$, always. Second, once the adhered film advances to the supply groove, any fluid reaching the supply groove re-supplies the full-film reducing the required makeup flux H_m according to Olsson's equation at θ_{form} given by Equation (2-23). This will be explained further in the next section. Third, the rupture meniscus is advanced according to the curve fit of the space-time relationship based on the current value of H_0. Along with the third step, the adhered film $H_a(T) = \frac{1}{2} H_{rup}$, as concluded with creeping flow, completes the profile of the adhered film in the space $d\theta_{rup}$ between $H_a(T)$ and $H_a(T + \Delta T)$.

3.4.2 Calculating Makeup Flux

Since the divergent portion of the bearing is fully starved at T = 0, there will be a time lapse before the first occurrence of adhered film reaches θ_{form}. Up until that time, the value of the makeup flux H_m is given by Equation (2-22) with $H_{a,form} = 0$, which turns out to be just H_0 (see Equation (2-11)). Once the adhered film does reach θ_{form}, the additional contribution of the adhered film has to be taken into account. Since the location and value of the adhered film is only known at discrete times $Ha(T_n)$, the flux must be found by numerically integrating the adhered film profile previously created as it reaches the full-film. The supply groove is assumed to have a finite width Δg of 1 degree centered at θ_{form}. For each value of the adhered film reaching at least the upstream edge of the supply groove $\left(\theta_{form} - \frac{\Delta g}{2}\right)$, one of two possibilities arises. Either the trailing value also passes over the supply groove or it does not.

If the trailing value does pass over the supply groove, then the entire area under the profile between $H_a(T_n)$ and $H_a(T_{n-1})$ is added to H_m as the area of a trapezoid $\Delta H_{a,form}$ as in Figure 3-2(a). For this possibility the value of $H(T_n)$ is no longer kept for the next time step. It should be made clear that the distance between $H_a(T_{n-1})$ and $H_a(T_n)$ is not necessarily equal to $\Delta\theta$ which is the distance that each value advances along with the rotating journal surface in one unit time.

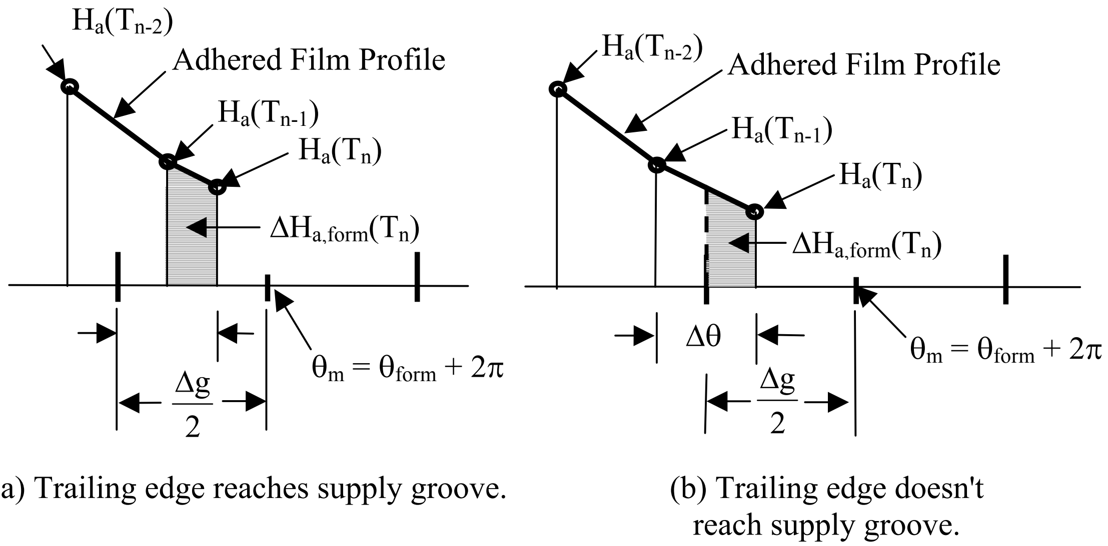

(a) Trailing edge reaches supply groove.

(b) Trailing edge doesn't reach supply groove.

Figure 3-4. Computing contribution of adhered film to makeup flux.

For the second possibility, when the trailing value has not yet reached the full-film, only the percentage of the area that has reached is counted, as in Figure 3-4(a). The value of the adhered film at the upstream edge of the supply groove is determined by linear interpolation between $H_a(T_{n-1})$ and $H_a(T_n)$, which is then used to calculate the reduced area to add to $\Delta H_{a,form}$. For the next time step, the value of $H_a(T_n)$ is set to the newly found interpolated value and its location is set to $\left(\theta_{\text{form}} - \frac{\Delta g}{2}\right)$. Although the distance $H_a(T_n)$ - $H_a(T_{n-1})$ should be larger than $Ha(T_{n-1})$ - $Ha(T_{n-2})$ since the rupture point is moving slower and slower as time progresses, it may indeed be smaller at any given time, since the distance may have been reduced at the previous time step under the second possibility.

3.4.3 Displaying the Half-void Results

Once the meniscus speed can be determined, the adhered film advanced and the makeup calculations performed, a thorough picture of the half-void solution from time zero to steady-state can be observed by simultaneously plotting both the pressure profile and film thickness. In the void region, the pressure is set to zero and the film thickness is given by a filled adhered film profile. The value of the makeup flux as it varies in time is displayed and saved for later plotting versus time.

4. Results and Discussion

4.1 Gumbel Charts

The Gumbel charts provide insight into the invariant full-film flux as dictated by the selected supply groove location θ_{form} for a given value of ε. A description of the Gumbel charts is illustrated with the chart for $\varepsilon = 0.4$ given in Figure 4-1. These charts are framed by the abscissa $-180° \leq \theta_{form} \leq 180°$ and the ordinate θ_{rup}. Every valid solution of the Reynolds equation with ambient condition specified at θ_{rup} at the given ε appears as a point $\theta_{rup}(\theta_{form}; \varepsilon)$. Two diagonal lines exclude redundancy due to the periodic property of the journal bearing. The lower diagonal represents the trivial limit of $\theta_{rup} \rightarrow \theta_{form}$. The upper diagonal is the general Sommerfeld solution.[3]

---

[3] The commonly known Sommerfeld solution with $\theta_{form} = 0°$ and $\theta_{rup} = 360°$ is the mid-point of the upper diagonal.

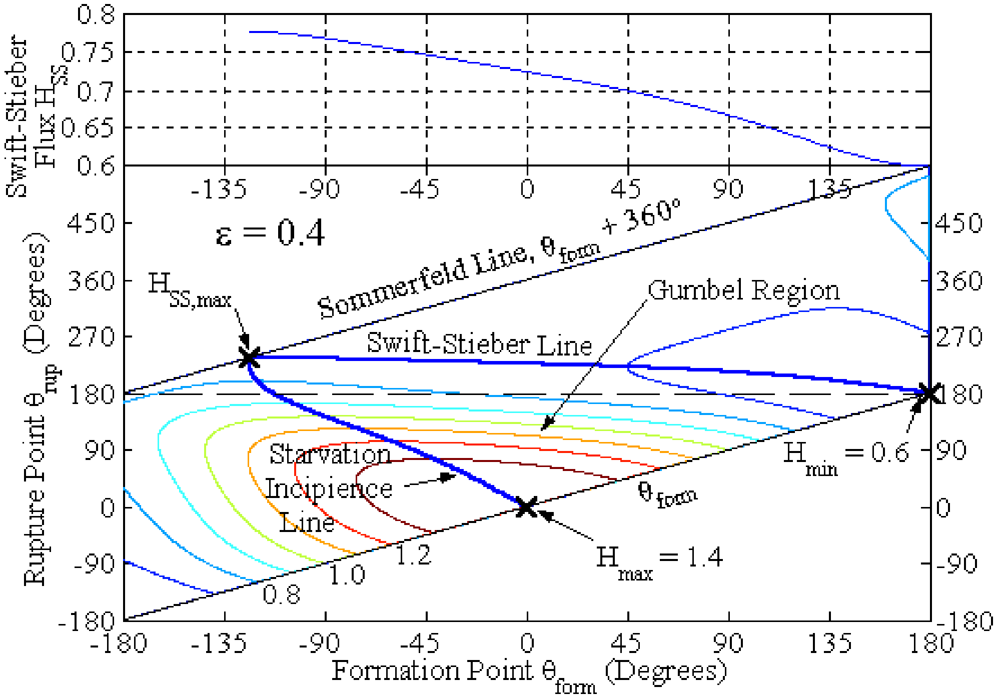

Figure 4.1. Gumbel chart for ε = 0.4.

Only a portion of the domain between the two diagonal lines is without sub-ambient condition satisfying the requirement

$$H_{form} \geq H_0 \geq H_{rup} \tag{4-1}$$

The upper boundary of this sub-domain is the Swift-Stieber Line that stipulates

$$\left(\frac{dP}{d\theta}\right)_{rup} = 0 \tag{4-2}$$

The lower boundary of this sub-domain is the Starvation Incipience Line, on which

$$\left(\frac{dP}{d\theta}\right)_{form} = 0 \tag{4-3}$$

In between these boundaries there exists a Generalized Gumbel Solution of the Reynolds equation with the properties of

- $P(\theta_{form} \leq \theta \leq \theta_{rup}) \geq 0$

- $\left(\frac{dP}{d\theta}\right)_{\text{form}} \geq 0$
- $\left(\frac{dP}{d\theta}\right)_{\text{rup}} \leq 0$

The lower diagonal is the trivial case of a film of zero extent and $H_0 = 1 + \varepsilon \cos \theta_{\text{form}}$. It intercepts the Swift-Stieber line at the right end, where $H_0 = 1-\varepsilon$ is the smallest possible film flux. On the Swift-Stieber Line, as θ_{form} moves to the left, H_{form} increases gradually and $H_0 = H_{SS}$ also increases. This is a monotonic process until the Swift-Stieber Line meets the Sommerfeld Line; the film extent is now a full circle. On the lower diagonal, as θ_{form} decreases further, the gap would be initially divergent. θ_{rup} can no longer follow the lower diagonal; it has a lower limit in order to preclude sub-ambient pressure. This is the beginning of the Starvation Incipience Line on which $\left.\frac{dP}{d\theta}\right|_{\text{form}}$ vanishes. To its left, the Reynolds equation solution would feature $\left.\frac{dP}{d\theta}\right|_{\text{form}} \geq 0$; hence the condition $\left.\frac{dP}{d\theta}\right|_{\text{form}} = 0$ truncates the Gumbel Chart as the lower boundary of θ_{rup}. The final effective Gumbel region is a distorted triangle that is enclosed within the Starvation Incipience Line, the lower diagonal and the Swift-Stieber Line. Along the Starvation Incipience Line, $\theta_{\text{rup}} \geq 0$ increases as θ_{form} further decreases until the former reaches the Sommerfeld Line concurrently with the Swift-Stieber Line. This is a Triple Point where $\left.\frac{dP}{d\theta}\right|_{\text{form}} = 0$, $\left.\frac{dP}{d\theta}\right|_{\text{rup}} \geq 0$ and $\theta_{\text{rup}} = \theta_{\text{form}} + 360°$ are simultaneously satisfied. The value of H_0 at the Triple Point (θ_{triple}) is the largest possible Swift-Stieber film flux $H_{SS,\max}$ for the given ε.

4.1.1 Gumbel Charts for Eccentricity Values of ε = 0.4, 0.6 and 0.8.

The generalized Gumbel solutions have been compiled for ε = 0.4, 0.6 and 0.8. The Gumbel chart for ε = 0.4 was already given in Figure 4-1 and charts for ε = 0.6 and 0.8 are presented in Figures 4-2 and 4-3. $H_{SS}(\theta_{form})$ is shown as the upper portion of each Gumbel chart. Sections of the contour lines of constant H_0 to the left of the Starvation Incipience Line depict film fluxes of incomplete Gumbel solutions. Two important trends with increasing ε are apparent from the charts and summarized in Table 4-1. First, inlet starvation, as indicated by θ_{triple}, occurs further downstream of the maximum gap. Second, the maximum invariant steady-state flux in the full-film region given by $H_{SS,max}$ is considerably less.

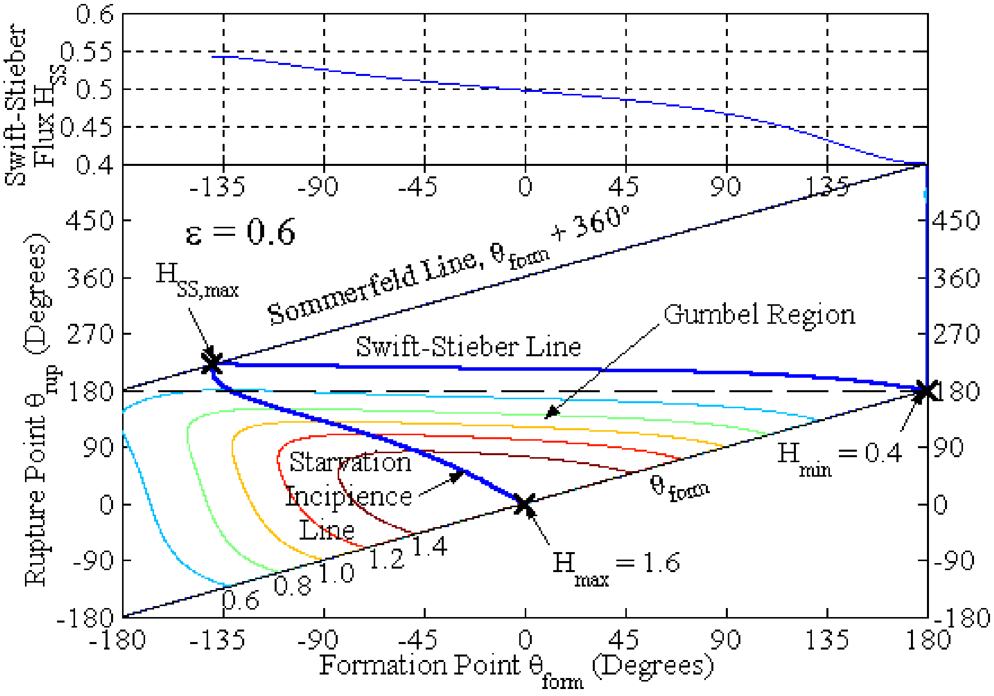

Figure 4-2. Gumbel chart for ε = 0.6.

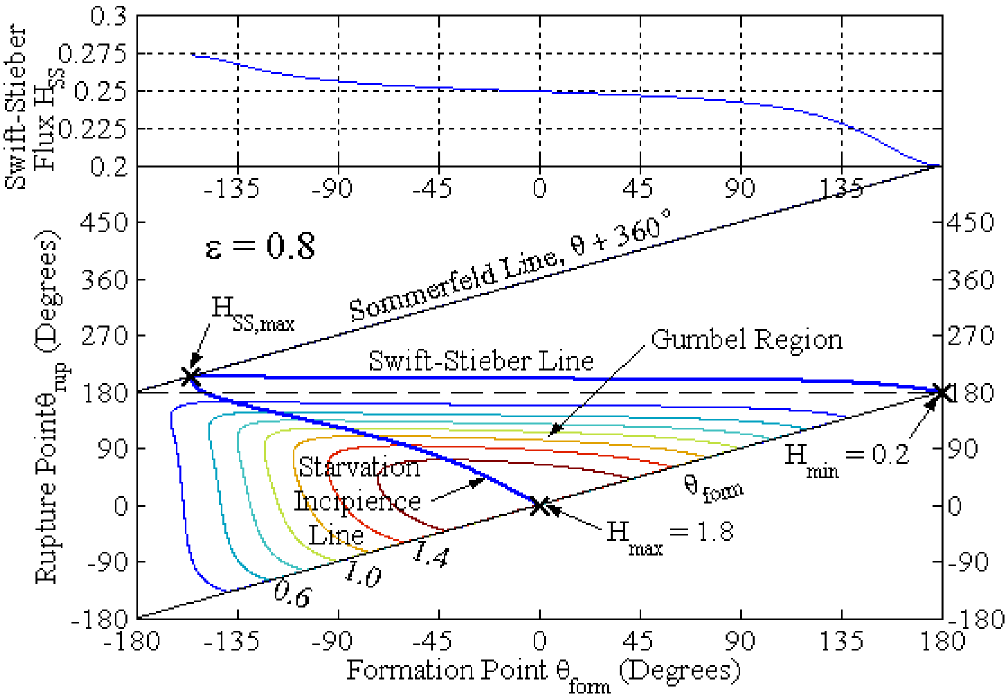

Figure 4-3. Gumbel chart for ε = 0.8.

Table 4-1. Comparison of Gumbel Charts with Different Eccentricity Values ε.

ε	θ_{triple} (Degrees)	$H_{SS,max}$ (Non-dimensional)
0.4	-123.7	0.775
0.6	-139.8	0.548
0.8	-155.4	0.275

4.1.2 Expanded Views of Gumbel Charts

As this work focuses on the transient problem of the Gumbel solution with θ_{rup} = 180° as an initial state towards the Swift-Stieber solution as the final steady-state, the details between the Half-Sommerfeld Line and the Swift-Stieber Line are of vital importance. Therefore, portions of Figures 4-1 to 4-3 are enlarged to fill the full height of Figures 4-4 to Figures 4-6 with contour lines for H_0 drawn at smaller intervals.

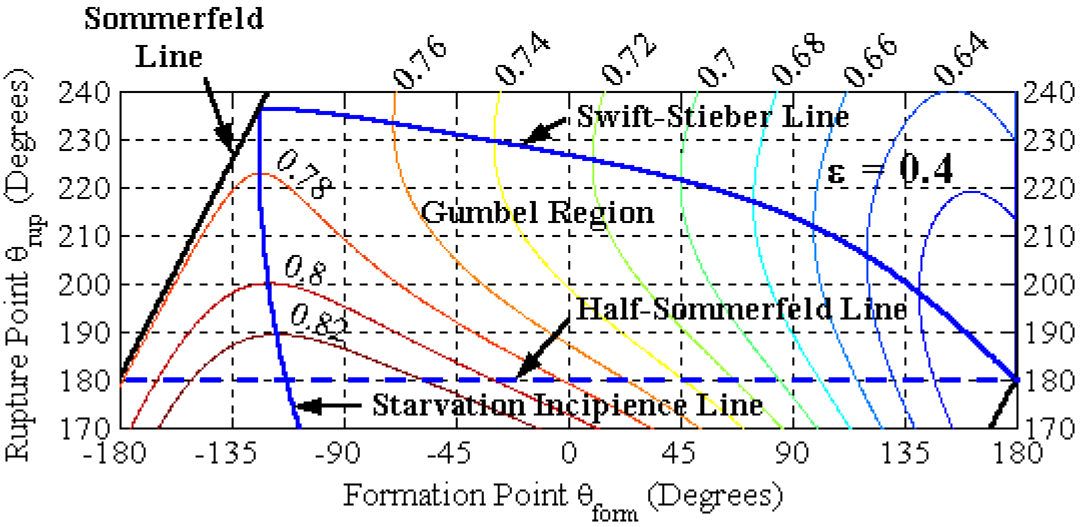

Figures 4-4. Expanded view of Gumbel chart for ε = 0.4.

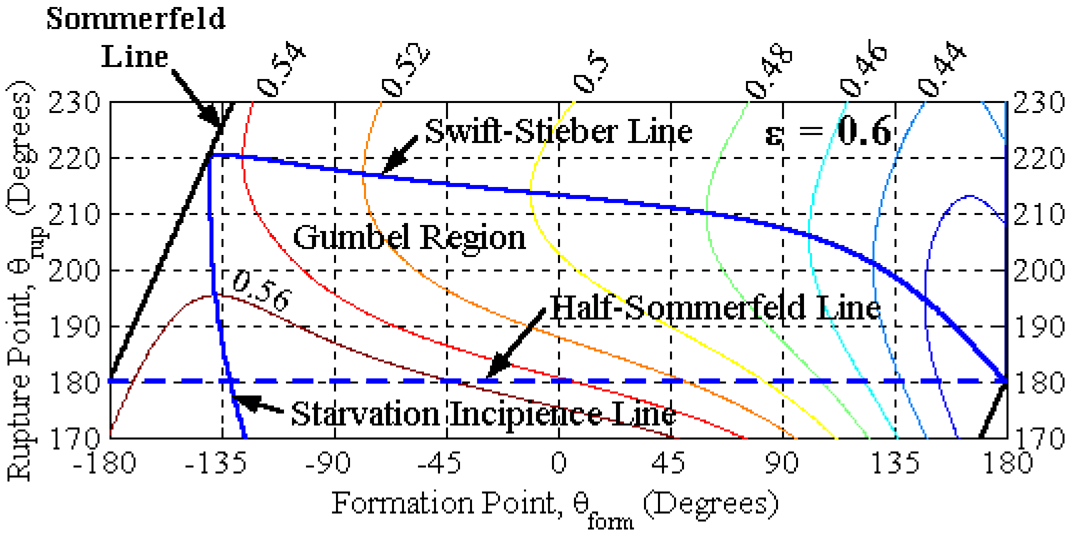

Figures 4-5. Expanded view of Gumbel chart for ε = 0.6.

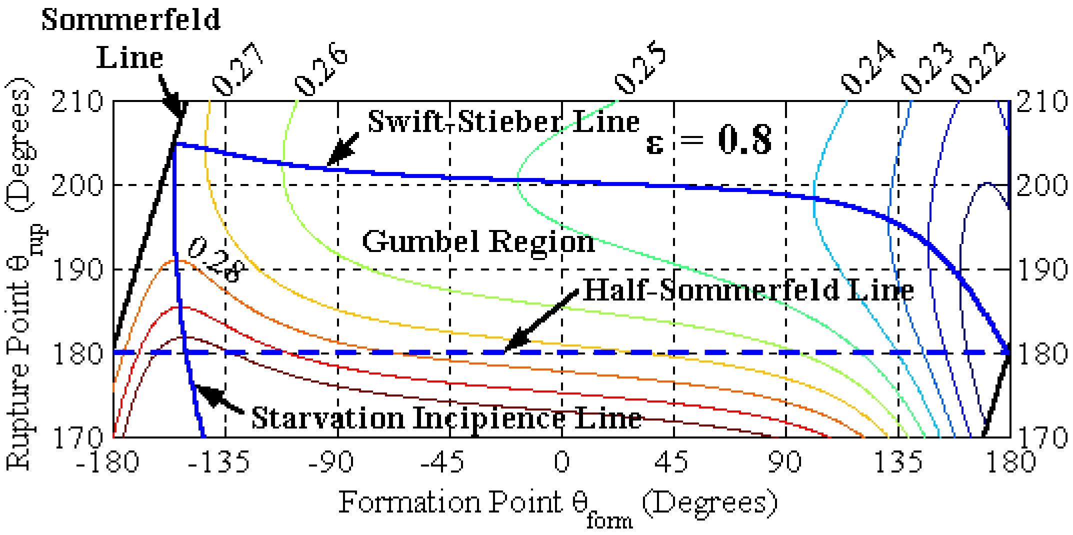

Figures 4-6. Expanded view of Gumbel chart for ε = 0.8.

4.2 Time Dependent Computations of the Rupture Point Movement

In a Gumbel chart, a vertical line, upon fixing θ_{form}, which connects a selected initial θ_{rup} to the Swift-Stieber line, contains the entire state history of the rupture point movement. Olsson's equation renders the speed of movement of the rupture meniscus at every intermediate state ($\theta_{rup,int}$). Time from start ($\theta_{rup,0}$) to a particular intermediate state is calculated as

$$T\left(\theta_{rup,int}\right) = \int_{\theta_{rup,0}}^{\theta_{rup,int}} \frac{d\theta_{rup}}{U_{rup}(\theta_{rup})} \tag{4-4}$$

For numerical computation, the state variable, $\theta_{rup,0} \le \theta_{rup} \le \theta_{SS,}$ is discretized in 100 grid spacings. $U_{rup}(\theta_{rup})$ is calculated from Olsson's equation and inverted to form the integrand, and numerical quadrature, e.g. trapezoidal rule, is used to construct $T(\theta_{rup})$. This procedure is called Inverse Time-Domain Integration because the result is $T(\theta_{rup})$ in contrast to Direct Time-Domain Integration that would yield $\theta_{rup}(T)$. Illustration of results obtained with this computation method are presented for $\varepsilon = 0.6$ with $\theta_{form} = (0°, \pm 20°, \pm 40°)$. Discretization sensitivity test for various grid spacing includes the cases for $\varepsilon = (0.4, 0.6$ and $0.8)$.

4.2.1 Examples of Inverse Time-Domain Integration

A grid system of 100 spacings for $180° \leq \theta \leq \theta_{SS}$ is used for the sample results with $\theta_{form} = (0°, \pm 20°, \pm 40°)$ at $\varepsilon = 0.6$. U_{rup} versus θ_{rup} is shown in Figure 4-7. The left end of the abscissa, 180°, is the initial state for all five cases. The bottom of the ordinate, $U_{rup} = 0$, is reached at the steady-state condition of Swift-Stieber. The five different θ_{form} yield five nearly parallel lines with slight downward tapers. θ_{SS} increases modestly for decreasing θ_{form} by a factor of roughly 0.05. The left intercepts of these lines show that $U_{rup,0}$ increases with decreasing θ_{form}, roughly 0.25% per degree.

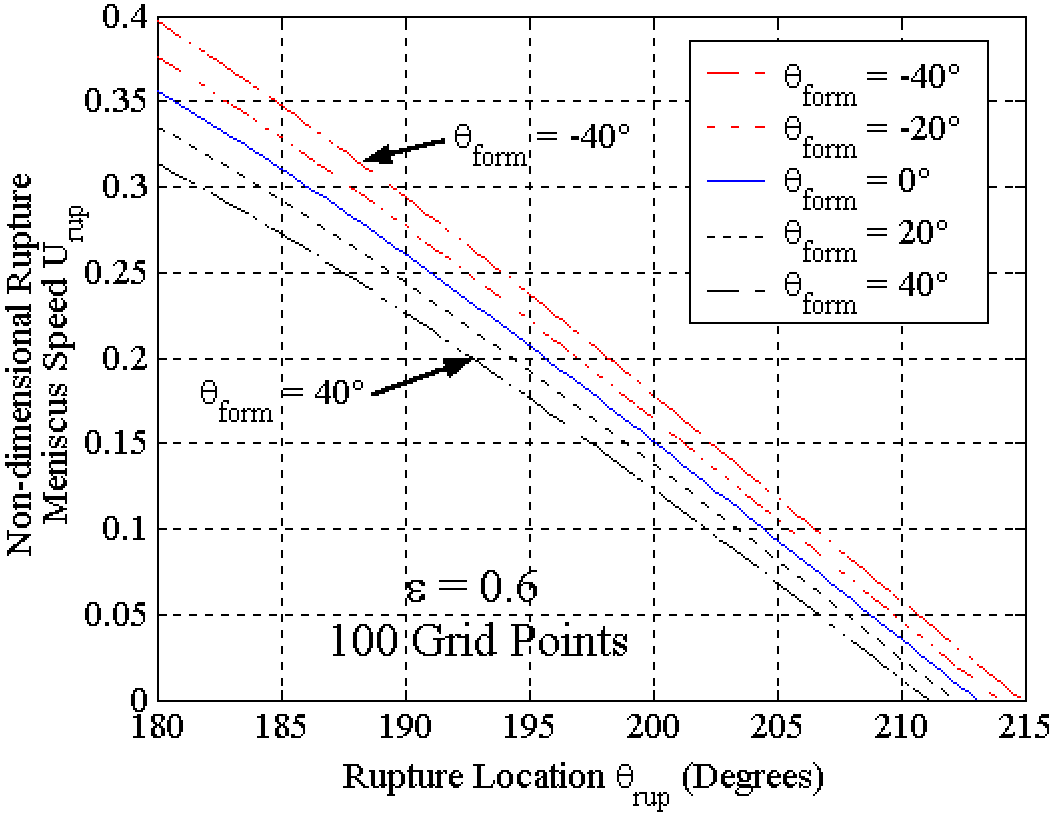

Figure 4-7. Non-dimensional rupture meniscus speed U_{rup} versus intermediate rupture point θ_{rup}.

In Figure 4-8, the reciprocal of the rupture point U_{rup}^{-1} is plotted versus θ_{rup}. The area underneath the curve represents the time T to reach a specific intermediate point. The last 5% of the grid system is not shown because U_{rup}^{-1} is unbounded as θ_{SS} is approached.

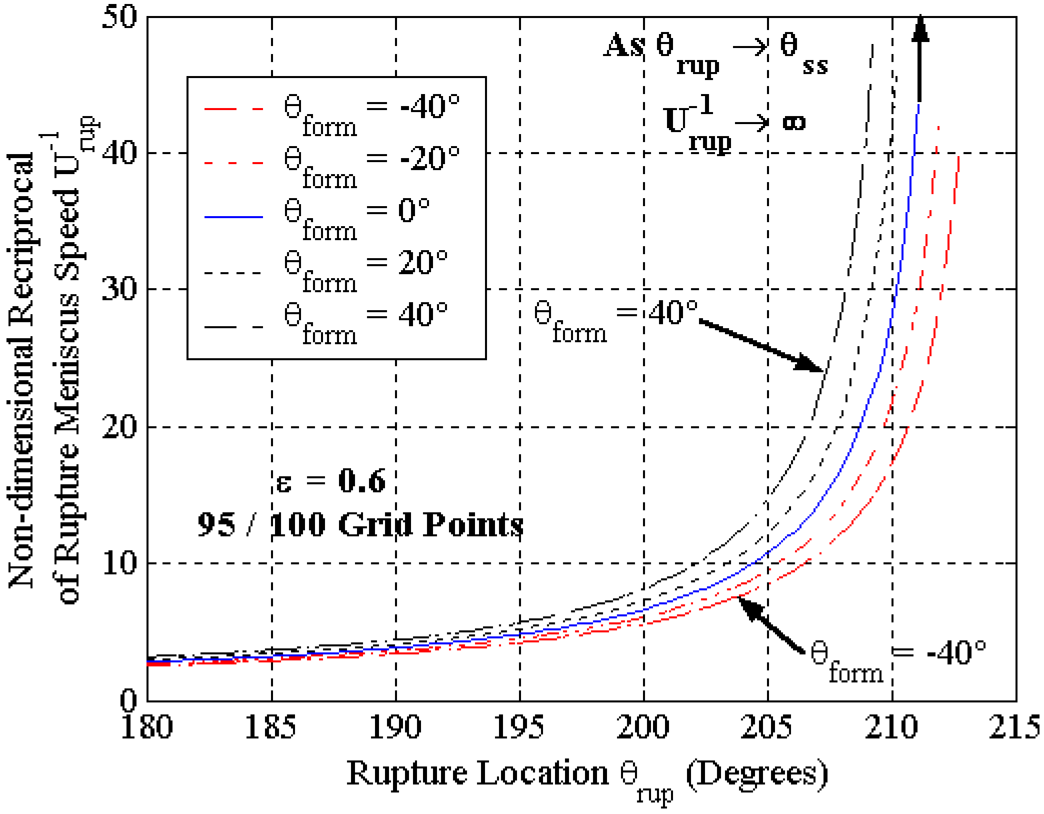

Figure 4-8. Non-dimensional reciprocal of rupture meniscus speed U_{rup}^{-1} versus intermediate rupture point θ_{rup}.

Figure 4-9 shows the result of Inverse Time-Domain Integration, again not including the last 5%. Earlier, in Figure 4-7, it was seen that a shift of θ_{form} causes competing consequences, that of a shift of θ_{SS} and concurrently a change in U_{rup}. Curiously, Figure 4-9 indicates by moving θ_{form} ahead of the maximum film thickness, the farther steady-state Swift-Stieber condition is reached earlier. It should be noted that it is not the direction of change of θ_{form} as such, but rather the change of $\left(\frac{dP}{d\theta}\right)_{rup}$ that enters into Olsson's equation. The trends observed here will, for certain, be reversed as θ_{form} approaches the Triple Point.

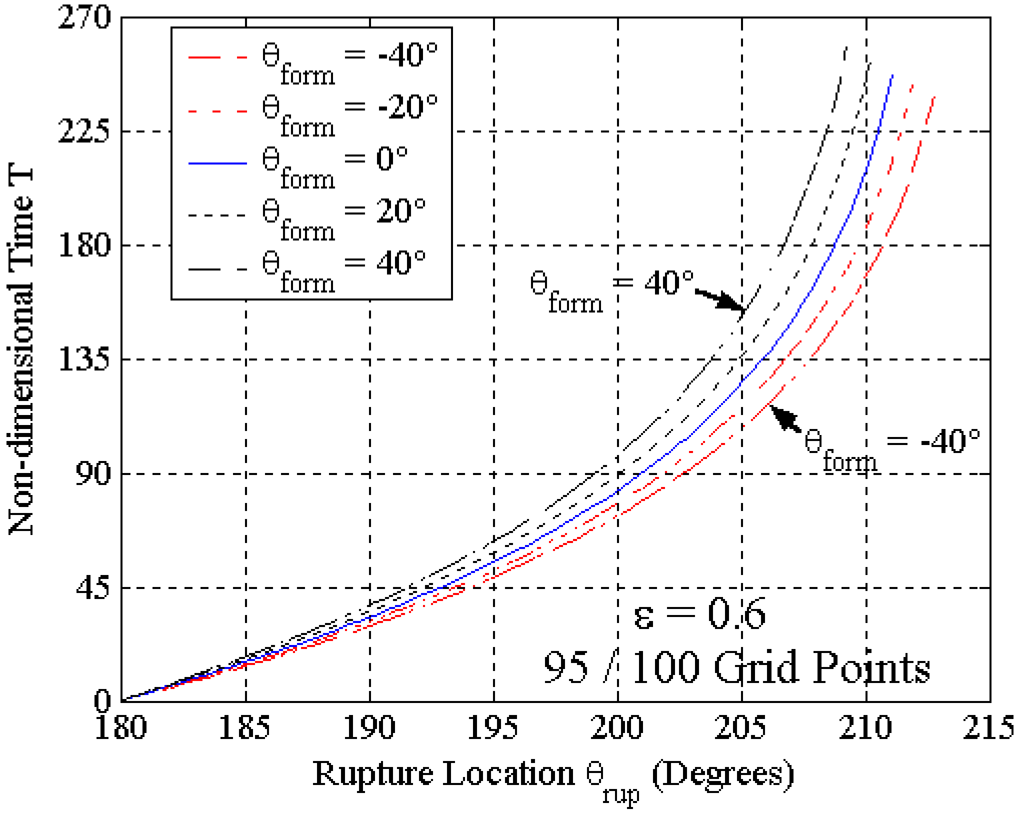

Figure 4-9. Non-dimensional time T versus intermediate rupture point θ_{rup}.

4.2.2 Effect of Grid Spacing

A convergence study was performed to see how the grid spacing affects the time-dependent results. θ_{SS} is unaffected by the grid spacing, since it obtained by the bisection method, which is why only a single value for θ_{SS} is given in Tables 4.2 – 4.4. As the number of grid points increases, the time though to reach the Swift-Stieber point, clearly increases. This can be attributed to the fact that U_{rup} is always decreasing. With a smaller grid spacing, a more up-to-date value of U_{rup} (i.e. smaller value) is used which results in more time after integration.

Table 4-2. Time Dependent Results for ε = 0.4.

θ_{form} (Degrees)	θ_{rup} (Degrees)	Non-dimensional Steady-state Time T_{SS}		
		Number of Grid Points in θ-Direction		
		100	300	900
-40	230.42	389.4	402.8	407.7
-20	228.54	398.2	411.8	416.8
0	226.58	408.5	422.4	427.5
20	224.46	421.3	435.4	440.6
40	222.08	437.6	452.2	457.5

Table 4-3. Time Dependent Results for ε = 0.6.

θ_{form} (Degrees)	θ_{rup} (Degrees)	Non-dimensional Steady-stateTime T_{SS}		
		Number of Grid Points in θ-Direction		
		100	300	900
-40	214.86	238.9	247.1	250.1
-20	213.95	243.2	251.5	254.6
0	213.08	247.7	256.1	259.2
20	212.16	252.7	261.3	264.4
40	211.14	258.8	267.5	270.7

Table 4-4. Time Dependent Results for ε = 0.8.

θ_{form} (Degrees)	θ_{rup} (Degrees)	Non-dimensional Steady-state Time T_{SS}		
		Number of Grid Points in θ-Direction		
		100	300	900
-40	200.63	145.5	150.4	152.3
-20	200.39	146.8	151.8	153.6
0	200.17	148.1	153.1	154.9
20	199.95	149.3	154.4	156.2
40	199.70	150.8	155.9	157.7

The convergence study was performed by determining T at two different values – at 50% of the T_{SS} and also 95% of T_{SS}, as the number of grid points was increased The results can be found in Figures 4-10 and 4-11. There is a greater range in T as the grid spacing is reduced for the study at 95% than at 50%. This can be attributed to the values of U_{rup}^{-1} approaching infinity as θ_{rup} approached θ_{SS}. With the steep slope of U_{rup}^{-1} at this point, a small change in θ_{rup} results in a large change in T.

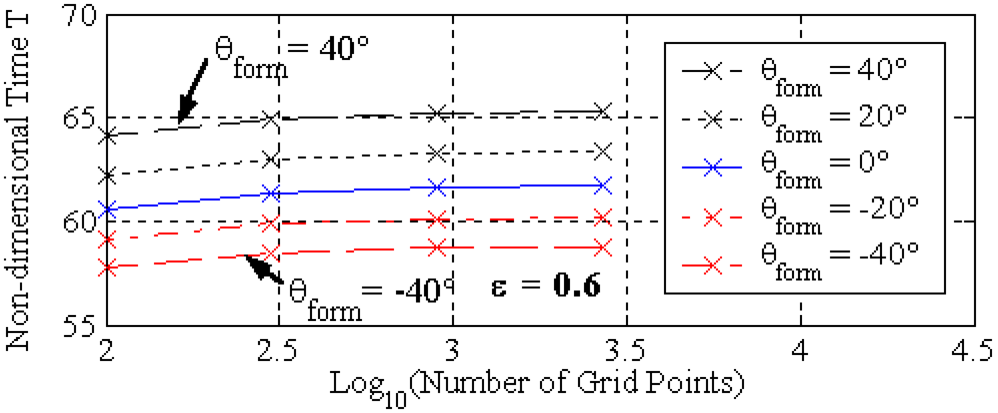

Figure 4-10. Convergence study of time to reach 50% of Swift-Stieber value θ_{SS}.

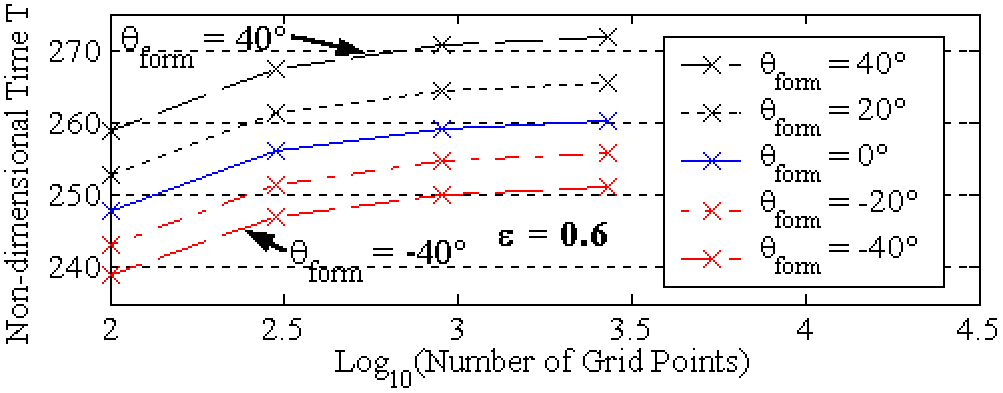

Figure 4-11. Convergence study of time to reach 95% of Swift-Stieber value θ_{SS}.

4.2.3 Comparing Eccentricity Values

The eccentricity ε is also varied (ε = 0.4, 0.6 and 0.8) to see its contribution on the steady-state time T_{SS}. The differences obtained with the changes in ε can be noticed by comparing Tables 4-2 through 4-4. For any θ_{form}, the decrease in T_{SS} is the same (roughly 39% depending on θ_{form}) when ε is changed from 0.4 to 0.6 as when it is changed from ε = 0.6 to 0.8. Since the time T has been made non-dimensional with respect to the journal rotational speed U, T_{SS} corresponds to the equivalent distance covered by the adhered film while the rupture point travels form 180° to θ_{SS}. This is referred to as "surface clocking". As an example, for $\varepsilon = 0.6$ and $\theta_{form} = 0°$, $T_{SS} = 247.7$ which indicates the adhered film produced at T = 0 at rupture would travel 247.7° with the journal (if it didn't reach θ_{form} first). All else being equal, if the journal orientation is placed in an unsteady state, the fluid requires less time to re-establish equilibrium while operating under a higher value of ε.

4.3 Complete Solution to the Half-void Problem

The complete solution to the half-void problem presented here involves three steps concurrently:

- performing the integral method to obtain rupture point speeds just explained.
- advancing the adhered film profile $H_a(T, \theta)$ along with the rotating journal
- calculating the makeup flux H_m at the supply groove for each time step T.

Two graphs were generated for a wide range of chosen θ_{form} plotting both pressure P and film thickness H versus rupture location θ_{rup} on different axes. In the void region of the film thickness versus θ_{rup} graph, the adhered film thickness H_a is plotted with H for comparison. Two graphs were selected for the same $\theta_{form} = 0°$ location at two different T in Figures 4-12 and 4-13 for the purpose of explaining the graphs. All examples given are for $\varepsilon = 0.6$.

The top half of Figure 4-12 plots the non-dimensional pressure P versus θ_{rup} at T only slightly after T = 0. The pressure profile is only slightly changed from the half-

Sommerfeld shape and $\left(\frac{dP}{d\theta}\right)_{rup}$ is still very steep. The bottom half of Figure 4-12 shows the full-film region extended to just past 180°. The void region was initially fully starved, but H_a begins its advance towards $\theta_{form} + 360°$. The current contribution at any T to H_a is always equal to ½ H_{rup}. The adhered film profile remains close to horizontal as θ_{rup} advances in the early parts of the divergent section of the bearing.

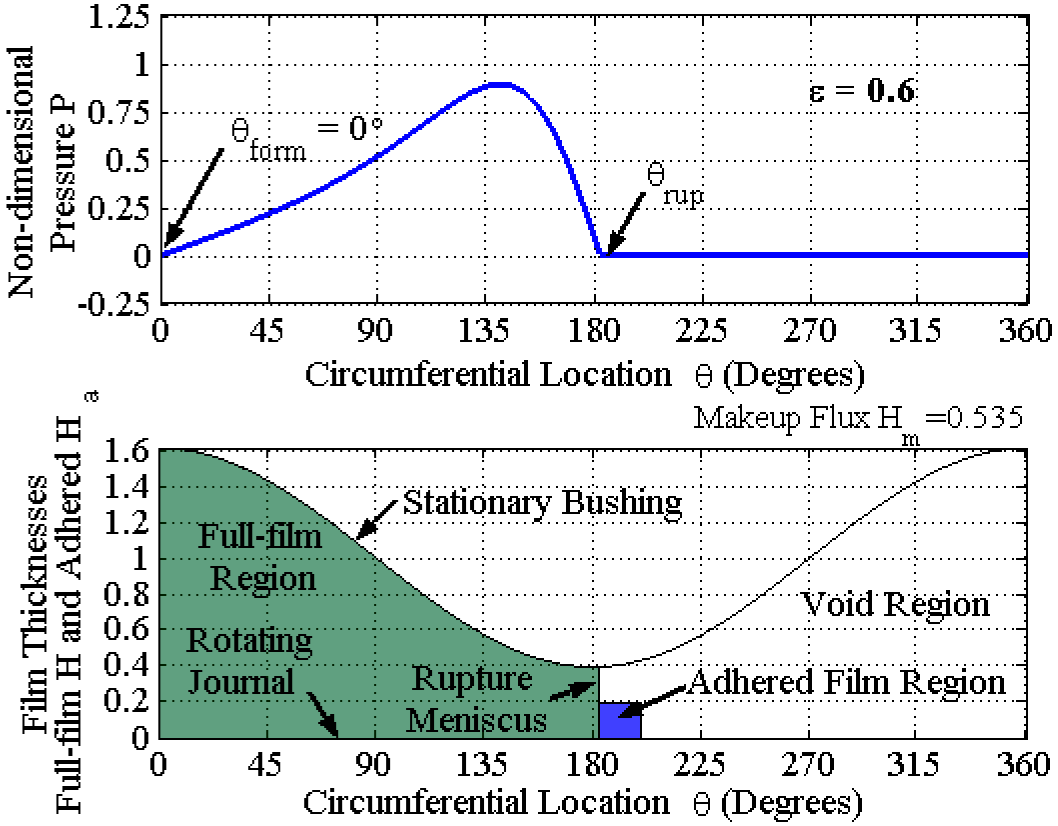

Figure 4-12. Solution to the half-void problem for $\theta_{form} = 0°$.

Figure 4-13 plots the same information contained in Figure 4-12 for the same $\theta_{form} = 0°$, except for a later value of T closer to T_{SS}. θ_{rup} is now much closer to θ_{SS} and $\left(\frac{dP}{d\theta}\right)_{rup}$ is closer to zero. It can also be observed, but not so apparent, that the maximum pressure P_0 has moved closer to 180° and the value of P0 has also increased. The curved shape of H_a is now much more noticeable, since θ_{rup} is now moving through the divergent section of the bearing where H increases faster compared to earlier times.

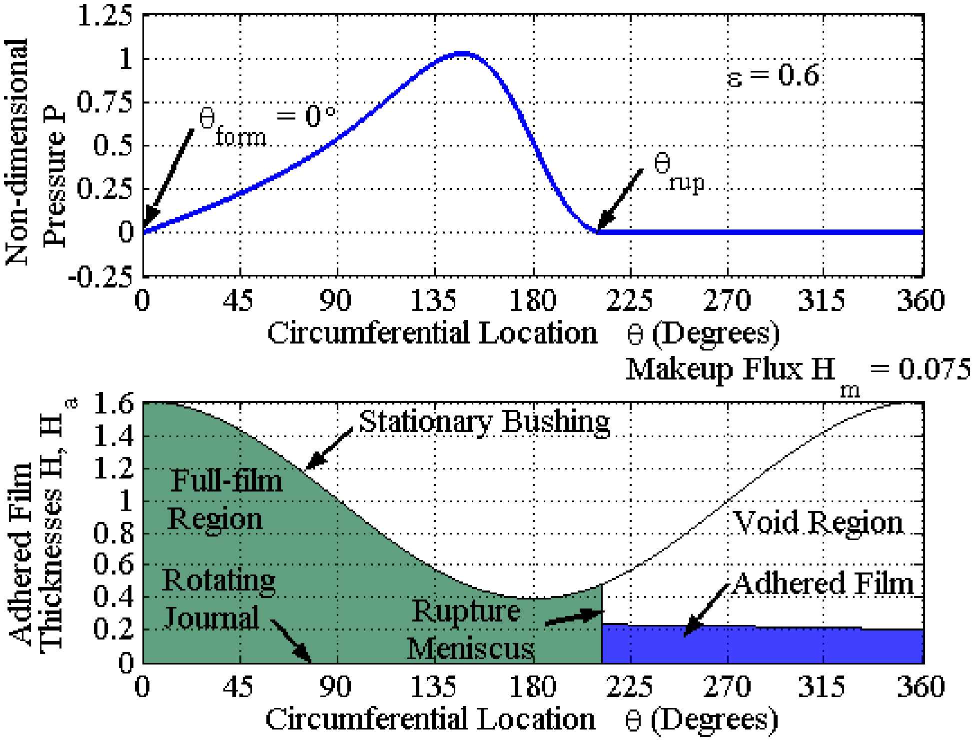

Figure 4-13. Solution to the half-void problem for $\theta_{form} = 0°$ at a later time T.

4.3.1 Classifying Results by Regions

To help with the investigation of the effects of different values of θ_{form}, an expanded, shaded view of the upper Gumbel region for $\varepsilon = 0.6$ is given in Figure 4-14 which serves to divide the results into three regions. The two vertical dividing lines between the regions are located where the Starvation Incipience Line crosses the half-Sommerfeld dashed line and where the Starvation Incipience Line intersects the Swift-Stieber Line. Region I is the only region with all the intermediate Gumbel states contained within the Gumbel region from start to finish. For this reason, Region I is well understood and will be the only region which will be considered here. Both Regions II and III involve inlet starvation downstream of θ_{form} where the pressure drops below ambient and entail the presence of a reformation boundary θ_{ref} where P = 0 downstream of θ_{form} for some or all of the Gumbel states. Correct handling of rupture point movement in Regions II and III is uncertain and will be discussed in Section 6 – Future Works.

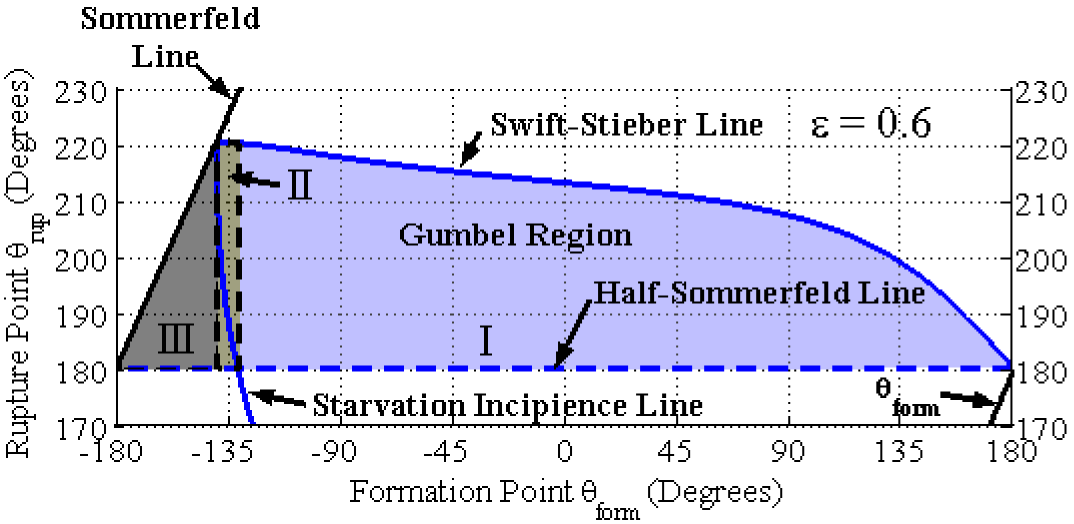

Figure 4-14. The three regions of the upper Gumbel region: I, II and III.

4.3.2 Region I – Entirely Gumbel Region

Region I includes all θ_{form} which are entirely in the Gumbel region for which $P \geq 0$ everywhere $\theta < \theta_{form} \leq \theta_{rup}$ for all T. The dividing point between Regions I and II is determined by the vertical line drawn through where the Starvation Incipience Line crosses the half-Sommerfeld Line. The rupture point speeds obtained (and the method behind them) are considered entirely valid for this region. The overall time-dependent behavior for all cases in Region I are roughly the same, there is nothing outstanding to note concerning any particular case. There are no abrupt transitions from one case to the next with only gradual differences in magnitude.

Besides the θ_{form} = 0° case already explained, one additional example in Region I is given in Figure 4-15 for θ_{form} = -90°. The pressure profile reveals that the value of P_0 is indeed higher for θ_{form} = -90° than for θ_{form} = 0°, although there is little apparent difference in θ_0 corresponding to P_0 for the two cases. The extent of the full film (θ_{rup} - θ_{form}) is, of course, longer. Although not shown since it is of little practical interest, the θ_{form} = +90°, does have a much smaller value of P_0 and a very small full-film extent.

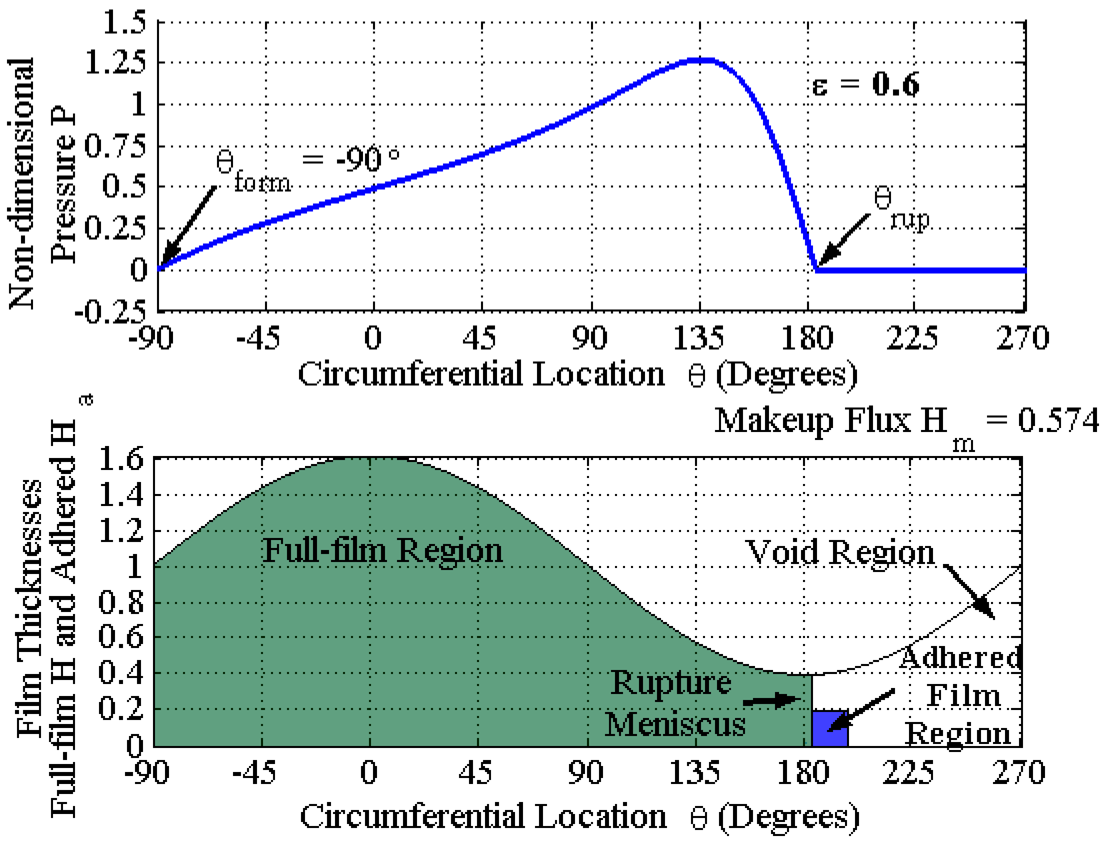

Figure 4-15. Example of supply groove location in Region I, θ_{form} = -90°.

4.3.3 Makeup Fluxes

The makeup fluxes for $\varepsilon = 0.6$ are plotted in Figures 4-16, 4-17 and 4-18 with $\theta_{form} = 90°$, $0°$ and $-90°$, respectively. As θ_{form} is moved further upstream of the minimum gap, the decreased distance that the adhered film travels before steady-state is reached is evident. The flow required to maintain full-film which is provided through the supply groove must also increase as θ_{form} shifts further from the minimum gap. Upon reaching steady-state it can be observed that the makeup flux goes to zero in all cases; when θ_{rup} reaches the equilibrium point θ_{SS}; the adhered film that is produced is exactly equal to the flow required to maintain a full-film. At steady-state, flow through the supply groove is no longer required and conservation of mass is demonstrated.

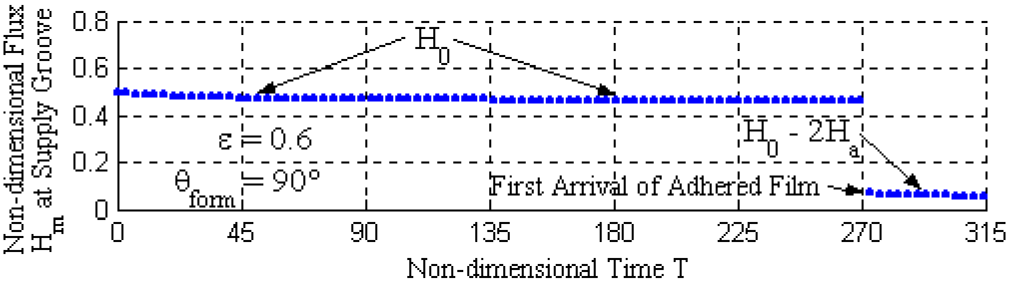

Figure 4-16. Makeup flux H_m for $\theta_{form} = 90°$.

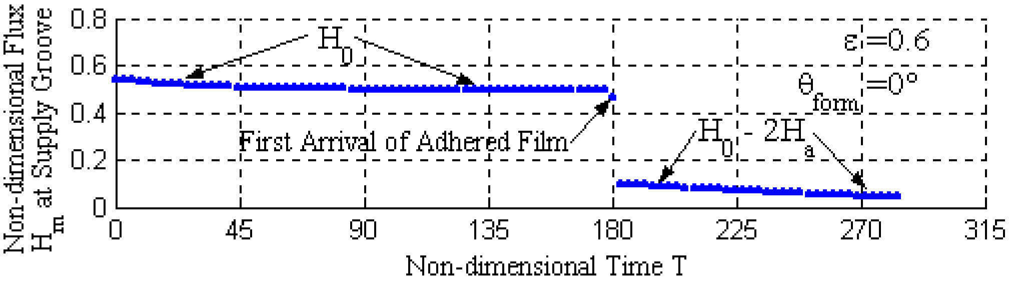

Figure 4-17. Makeup flux H_m for $\theta_{form} = 0°$.

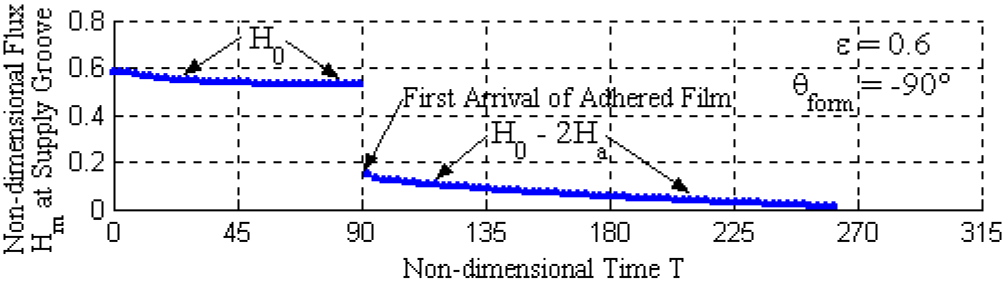

Figure 4-18. Makeup flux H_m for $\theta_{form} = -90°$.

4.4 Bearing Performance Results

4.4.1 Load Capacity and Attitude Angle

Polar plots showing the resulting non-dimensional load vector comprised of the load capacity W (magnitude) and attitude angle γ (direction) of various θ_{form} for $\varepsilon = 0.4$, 0.6 and 0.8 are shown in Figures 4-19, 4-20 and 4-21, respectively. For each θ_{form}, W is plotted as a continuous time-dependent curve from T = 0 to T_{SS} moving from left to right on the plots. The maximum steady-state load capacity occurs at $\gamma = 90°$ when the tangential component $W_x = 0$ and the radial component W_y is a maximum. This coincides with the Triple Point θ_{triple} for each ε as suggested by the Gumbel charts. The load vector indicates the non-dimensional load that could be supported by the fluid for a given ε as the fluid attains equilibrium. Figure 4-19 shows W for $\varepsilon = 0.6$ with $\theta_{form} = -160°$, displaying a lower magnitude compared to $\theta_{triple} = -139.8°$ at all but the final resting point at T_{SS}. Although the $\theta_{form} = -160°$ case is classified in Region III and involves inlet starvation, the anticipated path of the load capacity can be considered a reasonable estimate.

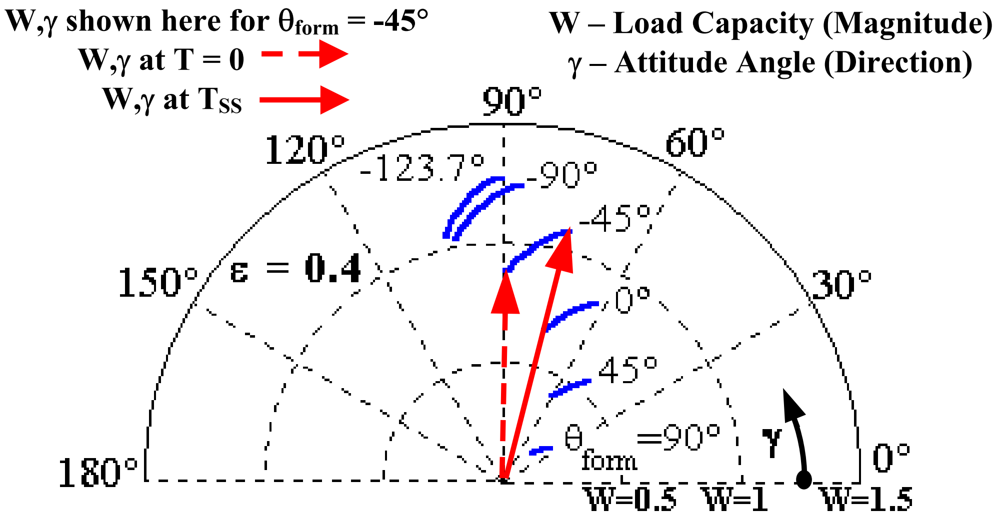

Figure 4-19. Polar plot showing load vector paths for ε = 0.4 and various θ_{form}.

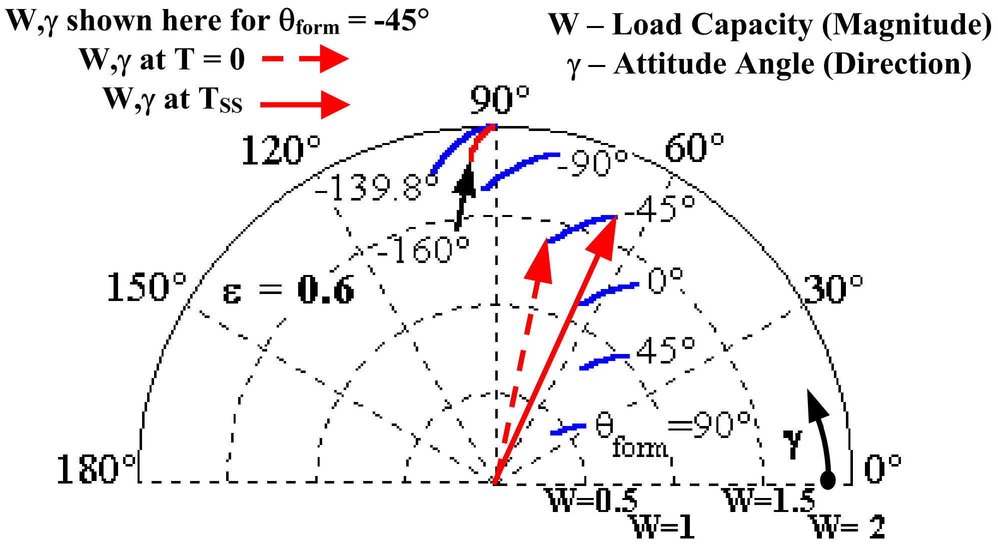

Figure 4-20. Polar plot showing load vector paths for ε = 0.6 and various θ_{form}.

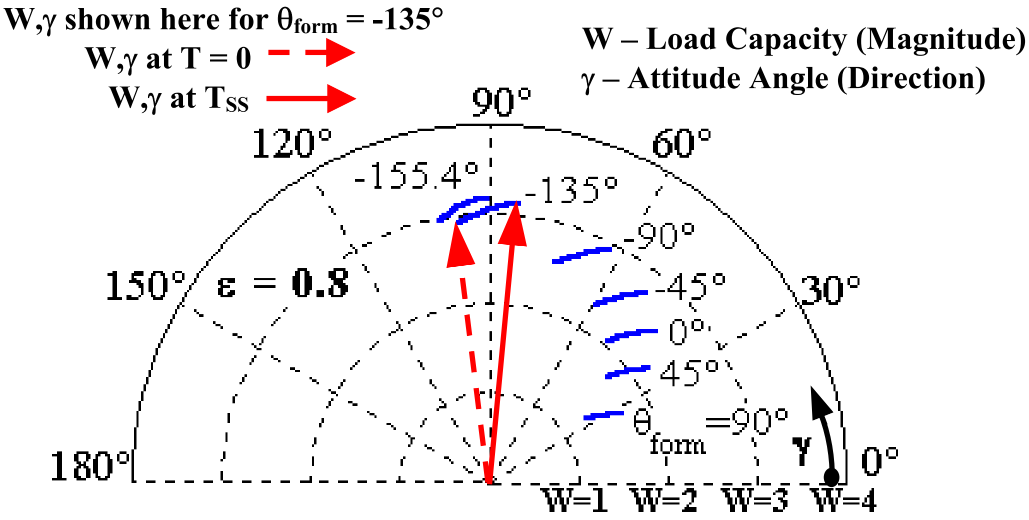

Figure 4-21. Polar plot showing load vector paths for ε = 0.8 and various θ_{form}.

The half-Sommerfeld (T = 0) and steady-state values (T_{SS}) can be found in Tables 4-6, 4-7 and 4-8 for ε = 0.4, 0.6 and 0.8, respectively. Results listed here agree with recently published results [4.1, 4.2], which only give formulations for special cases (half-Sommerfeld and Swift-Stieber at θ_{form} = 0°), whereas general, time-dependent results were obtained and plotted here. In addition, an expanded view of the contour plot of γ within the upper Gumbel region is provided for ε = 0.6 in Figure 4-22 which displays how γ varies with different Gumbel intermediate states.

Table 4-5. Load Capacity W and Attitude Angle γ for $\varepsilon = 0.4$.

θ_{form} (Degrees)	Non-dimensional Time T = 0		Non-dimensional Steady-state Time T_{SS}	
	Non-dimensional Load Capacity W	Attitude Angle γ (Degrees)	Non-dimensional Load Capacity W	Attitude Angle γ (Degrees)
90	0.171	42.98	0.249	34.27
45	0.410	59.56	0.555	48.52
0	0.659	74.47	0.843	61.67
-45	0.884	88.74	1.085	74.45
-90	1.037	100.94	1.243	86.01
-123.7	1.055	102.73	1.270	90.00

Table 4-6. Load Capacity W and Attitude Angle γ for $\varepsilon = 0.6$.

θ_{form} (Degrees)	Non-dimensional Time T = 0		Non-dimensional Steady-state Time T_{SS}	
	Non-dimensional Load Capacity W	Attitude Angle γ (Degrees)	Non-dimensional Load Capacity W	Attitude Angle γ (Degrees)
90	0.435	39.32	0.398	31.93
45	0.801	52.50	1.032	43.58
0	1.106	64.48	1.362	54.23
-45	1.382	77.25	1.636	65.60
-90	1.646	92.04	1.876	78.98
-139.8	1.772	100.94	1.997	90.00

Table 4-7. Load Capacity W and Attitude Angle γ for $\varepsilon = 0.8$.

θ_{form} (Degrees)	Non-dimensional Time T = 0		Non-dimensional Steady-state Time T_{SS}	
	Non-dimensional Load Capacity W	Attitude Angle γ (Degrees)	Non-dimensional Load Capacity W	Attitude Angle γ (Degrees)
90	1.289	32.99	1.671	27.45
45	1.775	41.72	2.202	35.21
0	2.081	49.67	2.514	42.19
-45	2.321	59.00	2.737	50.27
-90	2.563	73.21	2.926	62.48
-135	2.910	96.65	3.129	83.65
-155.4	2.970	100.42	3.173	90.00

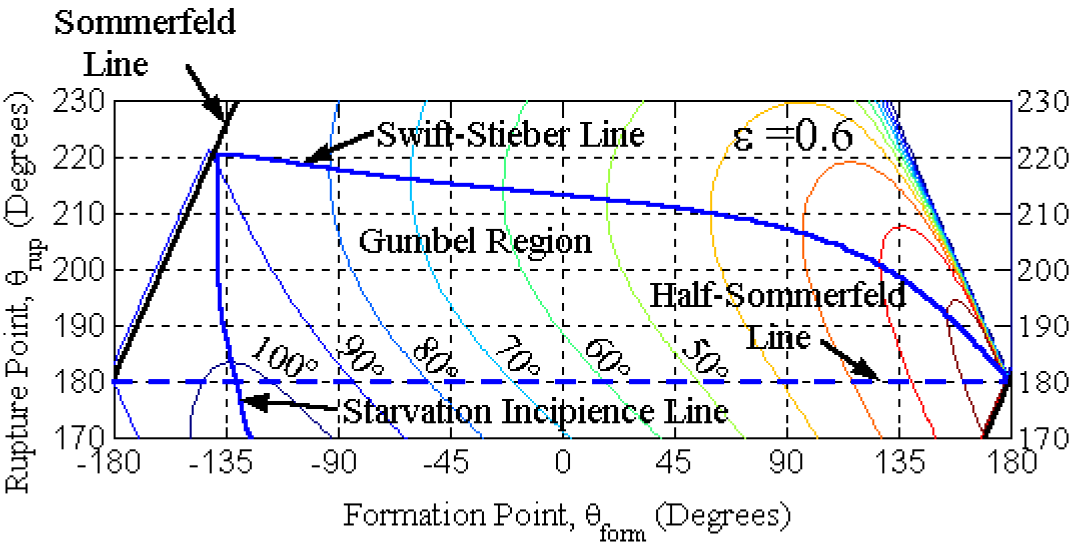

Figure 4-22. Detailed contour plot of constant attitude angles γ for ε = 0.6.

4.4.2 Frictional Force

The non-dimensional frictional force F_f is plotted in Figures 4-23 (a), (b) and (c) for ε = 0.4, 0.6 and 0.8, respectively, and various values of θ_{form}. As was found with the load vector, published results are limited to steady-state values or the half-Sommerfeld initial state [4.3]. The plots here are time-dependent curves of F_f as each Gumbel state θ_{rup} is reached. Three observations are made for both larger values of ε and for θ_{form} being further upstream from 180°:

- F_f is larger.
- The difference between $F_f(T_{SS}) - F_f(T = 0)$ is larger.
- F_f initially approaches $F_f(T_{SS})$ much faster as witnessed by the steeper slopes.

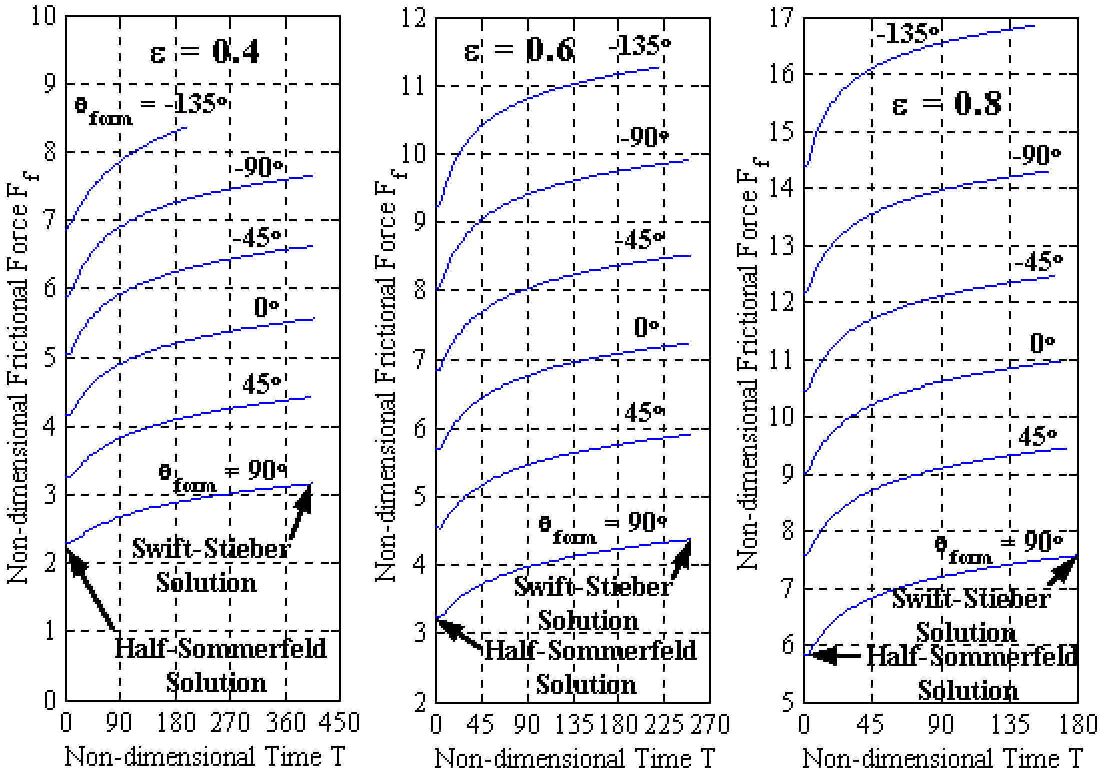

(a) ε = 0.4 (b) ε = 0.6 (c) ε = 0.8

Figure 4-23. Non-dimensional frictional force F_f versus non-dimensional time T for various eccentricity values ε.

The frictional force is useful in design for determining power requirements of the motor necessary to rotate the shaft in order to provide hydrodynamic lift for the bearing. With accurate, time-dependent values obtained for so little effort with this method, real-time modeling of dynamic control of the bearing would appear practical.

5. Conclusion

The solution to the half-void problem in long bearings presented here proposes a cogent two-phase morphology for handling cavitation. Sequential application of Olsson's continuity equation to the rupture points of the intermediate states (beyond the minimum gap) renders an interpretation of a time-dependent progression towards the ultimate Swift-Stieber solution. The solution has accomplished the following:

1. *Compact Reynolds Equation Integrals Derived.* The full-film integrals associated with the Reynolds equation were developed for arbitrary limits of full-film extent, which supports calculations for a continuous pressure profile considering cavitation with the start of the full-film other than the maximum gap.
2. *Gumbel Charts Developed.* The Gumbel charts summarize flow and the steady-state values for arbitrary supply groove arrangement. The occurrence or not of a reformation boundary (inlet starvation) is clearly predicted.
3. *Time-Dependent Bearing Performance Parameters Determined.* Traditional bearing performance parameters, specifically, the load vector and frictional force are obtained at any point in time, not just at the steady-state.
4. *Mass Conservation Demonstrated Globally.* Inclusion of the adhered film model with the Swift-Stieber boundary condition to provide cavity flow leads to mass conservation globally for the entire bearing.

The compact method can readily be extended to two-dimensions, offering a promising alternative to the Elrod cavitation algorithm, which is commonly used in more comprehensive bearing analyses. Progress made with the half-void problem is a considerable step towards modeling fluid perturbation response to a moving journal, both in plain journal bearings and also squeeze film dampers.

6. Future Work

6.1 Correct Handling of Inlet Starvation

The occurrence or not of inlet starvation involving sub-ambient non-dimensional pressures P just downstream of the formation point θ_{form} has been explained. The solution to the half void problem proposed is valid only if θ_{form} is found in Region I for the given eccentricity ε, as shown in Figure 6-1 for $\varepsilon = 0.6$. Region I consists of the solutions where $P \geq 0$ everywhere on $\theta_{form} < \theta \leq \theta_{ref}$. Improved solutions for Regions II and III need to be developed, involving the presence of inlet starvation and the existence of a reformation boundary $\theta_{ref.}$ which is shown in Figure 6-2 for $\theta_{form} = -145°$, a case that falls under Region III.

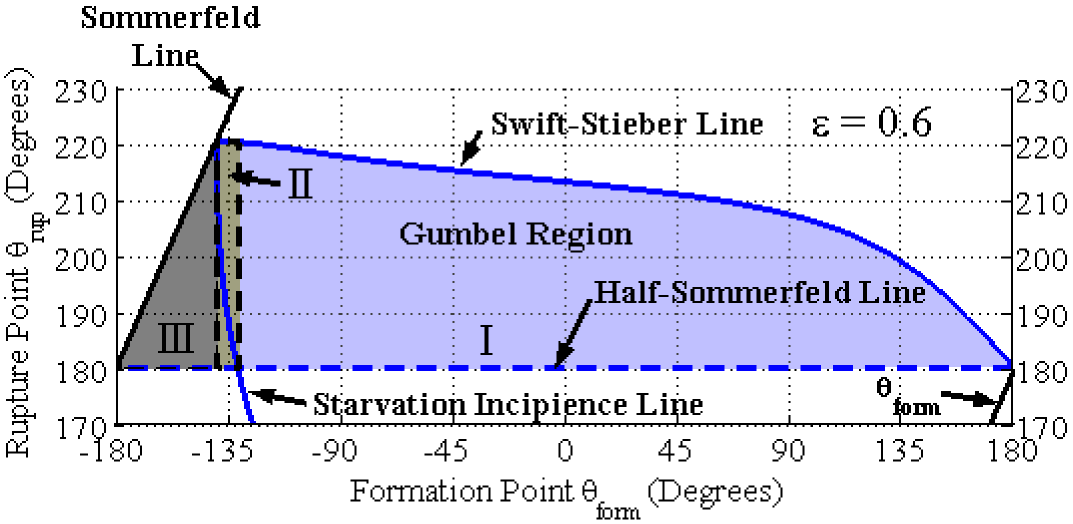

Figure 6-1. The three regions of the upper Gumbel region: I, II and III.

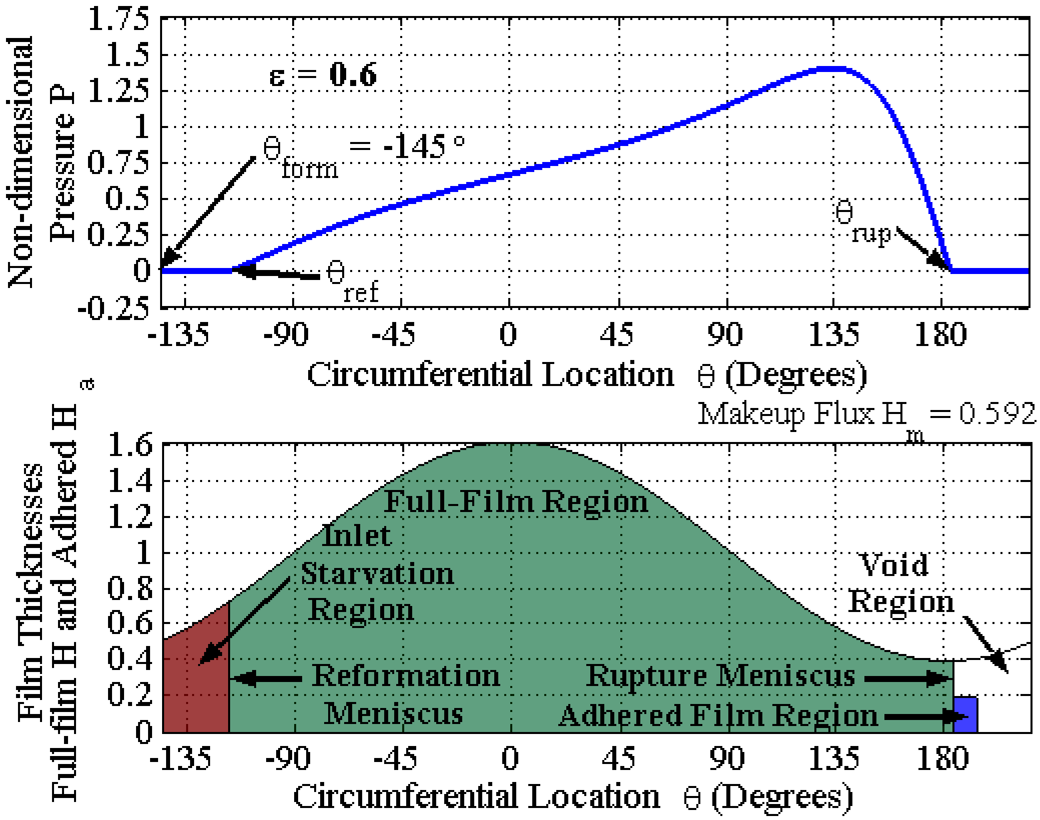

Figure 6-2. Example of supply groove location in Region III, $\theta_{form} = -145°$.

Specifically, an additional boundary condition for the Reynolds equation has to be applied at θ_{ref} that correctly determines the speed of both cavitation fronts at θ_{ref} and θ_{rup} simultaneously until inlet starvation disappears as a result of the arrival of adhered film introduced at θ_{rup}. Before the arrival of the adhered film, P at the supply groove is insufficient to maintain full-film on the interval $\theta_{form} < \theta \leq \theta_{ref}$ and both the rupture and reformation boundaries would move under a condition of constant flux. It is anticipated that for cases in Region II, a Swift-Stieber steady-state with will be reached where $\left(\frac{dP}{d\theta}\right)_{rup} = 0$. Whereas for cases in Region III, θ_{rup} will reach θ_{form} before a Swift-

Stieber steady-state is attained indicating the full-film spans the entire circumference of the bearing.

The following equation suggested by Floberg [6.1] is currently regarded as the correct equation, which would necessitate a two-dimensional solution:

$$\frac{Uh_{form}}{2} - \frac{{h_{form}}^{3}}{12}\left[\frac{\partial p}{\partial x} - \frac{\partial p}{\partial z}\left(\frac{dx}{dz}\right)\right]_{form} = \frac{Uh_{ref}}{2} \tag{6.1}$$

6.2 Extension to Two-Dimensions and Concatenation

The method proposed here can be readily extended to the two-dimensional problem, including time-dependence of the bearing gap. Whereas the rupture point movement in the one-dimensional case is accurately determined, a rupture line would have to be resolved. Concatenated mesh fluxes would be computed, from locally exact integrals of the two-dimensional Reynolds flux law (see Appendix D). Instantaneous rupture boundaries would be located as intercepts along the mesh lines. In this way, a relatively coarse computation mesh setup would be used and considerable computation savings can be expected in comparison with known conventional methods. A direct comparison can then be made to the Elrod Algorithm which is commonly used in comprehensive bearing analyses (see Appendix B).

6.3 Including Squeeze Film Effect

Progress made for rotating journal bearings could also be directed towards the study of squeeze film dampers. Roller bearings are used for the primary rotor lubrication in jet aircraft engines, however they have little ability to dissipate vibration. A journal bearing arrangement is commonly used in conjunction with roller bearings to provide supplemental damping. A simplified drawing of a squeeze film damper is shown in Figure 6-3 showing the journal rotating inside the roller bearing, which in turn, is surrounded by a layer of viscous fluid.

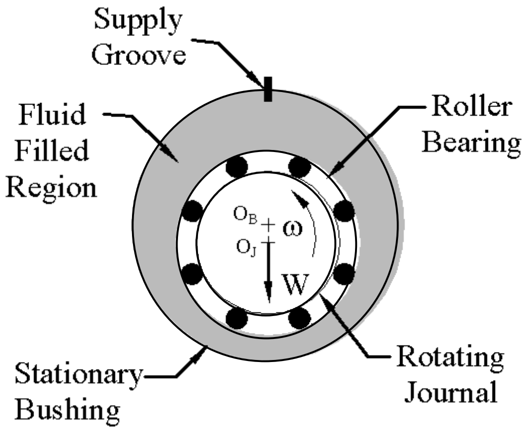

Figure 6-3. Simplified drawing of squeeze film damper.

In squeeze film dampers, cavitation mainly occurs due to translation, not rotation, of the roller bearing inside the bushing. The squeeze effect would locally increase fluid pressure causing flow away from the loading direction. Under heavy loading, oil is forced out through supply grooves located in the loading direction. A cavitation zone may form opposite the loading direction due to pressure reduction with rupture boundaries moving to establish equilibrium between full-film and void regions. Under light or negative loading, oil is fed through supply grooves to fill in the void. Once the method proposed here to solve the half-void problem in journal bearings is developed in two-dimensions, there is great potential for its application to squeeze film dampers.

7. References

1.1 Gumbel, L., "Monatsblatter Berlin Bezirksver," Verein Deutscher Ingenieure, p. 5, 1914.

1.2 Reynolds, O., "On the Theory of Lubrication and Its Application to Mr. Beauchamp Tower's Experiments, Including an Experimental Determination of the Viscosity of Olive Oil," *Philosophical Transactions of the Royal Society of London*, Series A, Vol. 177, p. 157, 1886.

1.3 Sommerfeld, A., Zeitschrift für Mathematik und Physik, p. 150, 1904.

1.4 Dowson, D, and Taylor, C. M., "Cavitation and Related Phenomena in Lubrication", *Proceedings of the 1st Leeds-Lyon Symposium on Tribology*, Mechanical Engineering Publications Limited, New York, NY, 1975.

1.5 Brewe, D.E., Ball, J.H. and Khonsari, M., "Current Research in Cavitating Fluid Films," NASA Technical Memorandum, No. 103184, May 1988.

1.6 Swift, H.W., "The Stability of Lubricating Films in Journal Bearings," *Proceedings of the Institute of Civil Engineers*, Volume 233, pp. 267-288, 1932.

1.7 Stieber, W., "Das Schwimmlager," *Verein Deutscher Ingenieure*, Berlin, 1933.

1.8 Jakobson, B. and Floberg, L., "The Finite Journal Bearing, Considering Vaporization," *Transactions of Chalmers University of Technology*, Gothenburg, Sweden, 1945.

1.9 Olsson, K.O., "Cavitation in Dynamically Loaded Bearings," *Transactions of Chalmers University of Technology*, Institute of Machine Elements, No. 26, 1965.

1.10 Coyne, J.C. and Elrod, H.G. Jr., "Conditions for the Rupture of a Lubricating Film Part I: Theoretical Model," *Journal of Lubrication Technology*, Volume 92, 451-456, July 1970.

1.11 Coyne, J.C. and Elrod, H.G., Jr., "Conditions for the Rupture of a Lubricating Film Part II: New Boundary Conditions for Reynolds Equation," *Journal of Lubrication Technology*, Volume 92, pp. 451-456, January 1971.

1.12 Floberg, L., "Cavitation Boundary Conditions with Regard to the Number of Streamers and Tensile Strength of the Liquid," Cavitation and Related Phenomena in Lubrication, *Proceedings of the 1st Leeds-Lyon Symposium on Tribology*, pp. 37- 41, 1975.

1.13 Crosby, W.A., "The Finite Journal Bearing Considering Film Separation," *Wear*, Volume 76, pp. 169-176, 1982.

1.14 Pan, C.H.T., "Dynamic Analysis of Rupture in Thin Fluid Films Part I: A Noninertial Theory," *Journal of Lubrication Technology*, Volume 105, pp. 96-104, January 1983.

1.15 Cole, J.A. and Hughes, C.J., "Oil Flow and Film Extent in Complete Journal Bearings," *Proceedings of the Institution of Mechanical. Engineers*, Volume 170, No. 17, 1956.

1.16 Etsion, I. and Pinkus, O., "Solutions of finite Journal Bearings with Incomplete Films," *ASME Paper*, No. 74-Lub-V, 1974.

1.17 Heshmat, H., "The Mechanism of Cavitation in Hydrodynamic Lubrication," *Journal of Tribology Transactions*, Volume 34, pp. 177-186, 1991.

1.18 San Andres, L. and Diaz, S.E., "Flow Visualization and Forces From a Squeeze Film Damper Operating With Natural Air Entrainment," *Journal of Lubrication Technology*, Volume 125, pp. 325-333, April 2003.

1.19 Elrod, H.G. and Adams, M.L., "A Computer Program for Cavitation and Starvation Problems," Cavitation and Related Phenomena in Lubrication, *Proceedings of the 1st Leeds-Lyon Symposium on Tribology*, pp. 37-41, 1975.

1.20 Elrod, H.G., "A Cavitation Algorithm," *Journal of Lubrication Technology*, Volume 103, pp. 350-354, July 1981.

1.21 Bayada, G., "Variational Formulation and Associated Algorithm for the Starved Finite Journal Bearing," *Journal of Lubrication Technology*, Volume 105, pp. 453-457, July 1983.

1.22 Bayada, G., Chambat, M. and El Alaoui, M., "Variational Formulations and Finite Element Algorithms for Cavitation Problems," *Journal of Tribology*, Volume 112, pp. 398-403, April 1990.

1.23 Woods, C.M. and Brewe, D.E., "The Solution of the Elrod Algorithm for a Dynamically Loaded Journal Bearing Using Multigrid Techniques," *Journal of Lubrication Technology*, Volume 111, pp. 302-308, April 1989.

1.24 Vijayaraghavan, D. and Keith, T.G., Jr., "An Efficient, Robust, and Time Accurate Numerical Scheme to a Cavitation Algorithm," *Journal of Lubrication Technology*, Volume 112, pp. 44-51, January 1990.

1.25 Kumar, A. and Booker, J.F., "A Finite Element Cavitation Algorithm: Application / Validation," *Journal of Tribology*, Volume 113, pp. 255-261, April 1991.

1.26 Claro, J.C.P. and Miranda, A.A.S., "Analysis of Hydrodynamic Journal Bearings Considering Lubricant Supply Conditions," *Proceedings of the Institution of Mechanical. Engineers*, Volume 207, pp. 93-101, 1993.

1.27 Yu, Q. and Keith, T.G., Jr., "Prediction of Cavitation in Journal Bearings Using a Boundary Element Method," *Journal of Tribology*, Volume 117, pp. 411-421, July 1995.

2.1 Dowson, D. and Taylor, C.M., "Fundamental Aspects of Cavitation in Bearings," P*roceedings of the 1st Leeds-Lyon Symposium on Tribology*, Mechanical Engineering Publications Limited, New York, NY, pp. 15-28, 1975.

2.2 Dubois, G.B. and Ocvirk, F.W., "Analytical Derivation and Experimental Evaluation of Short Bearing Approximation for Full Journal Bearings," *National Advisory Committee for Aeronautics Report*, 1157, 1953.

2.3 Gumbel, L., "Monatsblatter Berlin Bezirksver," *Verein Deutscher Ingenieure*, p. 5, 1914.

2.4 Swift, H.W., "The Stability of Lubricating Films in Journal Bearings," *Proceedings of the Institute of Civil Engineers,* Volume 233, pp. 267-288, 1932.

2.5 Stieber, W., "Das Schwimmlager," *Verein Deutscher Ingenieure*, Berlin, 1933.

2.6 Olsson, K.O., "Cavitation in Dynamically Loaded Bearings," *Transactions of Chalmers University of Technology*, *Institute of Machine Elements,* No. 26, 1965.

2.7 Bois, G.P., *Tables of Indefinite Integrals*, Dover Publications, Inc. New York, NY, 1961.

2.8 Harnoy, A., *Bearing Design in Machinery, Engineering Tribology and Lubrication*, Marcel Dekker, Inc., New York, NY, 2003.

3.1 Matlab Version 6.5 R13, Software Application, *The MathWorks Inc*., Natick, MA, Copyright 1984- 2002.

3.2 Khonsari, M. M. and Booser, R. E., *Applied Tribology Bearing Design and Lubrication*, John Wiley & Sons, Inc. New York, NY, pp. 204, 2001.

4.1 Khonsari, M. M. and Booser, R. E., *Applied Tribology Bearing Design and Lubrication*, John Wiley & Sons, Inc. New York, NY, pp. 214-217, 2001.

4.2 Szeri, A. Z., *Fluid Film Lubrication, Theory and Design,* Cambridge University Press, New York, NY, pp.102-107, 1998.

4.3 Harnoy, A., *Bearing Design in Machinery Engineering Tribology and Lubrication*, Marcel Dekker, Inc. New York, NY pp. 133-134, 2003.

6.1 Floberg, L., "Boundary Condition of Cavitation Regions in Journal Bearings," *Transactions of the American Society of Lubrication Engineers*, Volume 4, pp. 262-266, 1961.

A.1 Harnoy, A., *Bearing Design in Machinery, Engineering Tribology and Lubrication*, Marcel Dekker, Inc., New York, NY, 2003, p128.

A.2 DuBois, G.A. and Ocvirk, F.W., "Analytical Derivation and Experimental Evaluation of Short Bearing Approximation for Full Journal Bearings," *National Advisory Committed for Aeronautics Report*, 1157, 1953.

B.1 Vijayaraghavan, B. and Keith, T.G., Jr., "An Efficient, Robust, and Time Accurate Numerical Scheme Applied to a Cavitation Algorithm," *Journal of Tribology*, Vol. 112, pp. 44-51. January 1990.

B.2 Elrod, H.G. and Adams, M.L., "A Computer Program for Cavitation and Starvation Problems," Cavitation and Related Phenomena in Lubrication, *Proceedings of the 1st Leeds-Lyon Symposium on Tribology*, pp. 37-41, 1975.

B.3 Elrod, H.G., "A Cavitation Algorithm," *Journal of Lubrication Technology*, Volume 103, pp. 350-354, July 1981.

B.4 Bayada, G., "Variational Formulation and Associated Algorithm for the Starved Finite Journal Bearing," *Journal of Lubrication Technology*, Volume 105, pp. 453-457, July 1983.

B.5 Bayada, G., Chambat, M. and El Alaoui, M., "Variational Formulations and Finite Element Algorithms for Cavitation Problems," *Journal of Tribology*, Volume 112, pp. 398-403, April 1989.

B.6 Woods, C.M., and Brewe, D.E., "The Solution of the Elrod Algorithm for a Dynamically Loaded Journal Bearing Using Multigrid Techniques," *Journal of Lubrication Technology*, Volume 111, pp. 302-308, April 1989.

B.7 Vijayaraghavan, D. and Keith, T.G., Jr., "An Efficient, Robust, and Time Accurate Numerical Scheme to a Cavitation Algorithm," *Journal of Lubrication Technology*, Volume 112, pp. 44-51, January 1990.

B.8 Kumar, A. and Booker, J.F., "A Finite Element Cavitation Algorithm: Application / Validation," *Journal of Tribology*, Volume 113, pp. 255-261, April 1991.

B.9 Claro, J.C.P., and Miranda, A.A.S., "Analysis of Hydrodynamic Journal Bearings Considering Lubricant Supply Conditions," *Proceedings of the Institution of Mechanical Engineers*, Volume 207, pp. 93-101, 1993.

B.10 Yu, Q. and Keith, T.G., Jr., "Prediction of Cavitation in Journal Bearings Using a Boundary Element Method," *Journal of Tribology*, Volume 117, pp. 411-421, July 1995.

B.11 Kohno, K., Takahashi, S. and Saki, K., "Elasto-hydrodynamic Lubrication Analysis of Journal Bearings with Combined Use of Boundary Elements and Finite Elements," *Engineering Analysis with Boundary Elements,* Volume 13, pp. 273-281, 1994.

B.12 Sui, P.C., Troxler, P. and Vanderpoel, R., "Predicting Distributor-type Fuel Injection Pump Rotor Motion Using an Integrated Lubrication and Structural Dynamics Model," *Tribology Transactions*, Volume 38, No. 4, pp. 811-820, October 1995.

B.13 Vijayaraghavan, D., Keith, T.G., Jr. and Brewe, D. E., "Effect of Lubricant Supply Starvation on the Thermohydrodynamic Performance of a Journal Bearing," *Tribology Transactions*, Volume 39, No. 3, pp. 645-653, 1996.

B.14 Hirami, H., Athre, K. and Biswas, S., "Comprehensive Design Methodology for an Engine Journal Bearing," *Proceedings of the Institution of Mechanical Engineers*, Volume 214, pp. 401-412, 2000.

B.15 Mourelatos, Z. P., "A Crankshaft System Model for Structural Dynamic Analysis of Internal Combustion Engines," *Computers and Structures*, Volume 79, pp. 2009-2027, 2001.

B.16 Matlab Version 6.5 R13, Software Application, *The MathWorks Inc*., Natick, MA, Copyright 1984-2002.

D.1 Pan, D.H.T., Perlman, A. and Li, W., "A New Numerical Technique for the Analysis of Lubricating Films. Part I: Incompressible, Isoviscous Lubricant," *Proceedings of the 13th Leeds-Lyon Symposium on Tribology*, England, September 1986, (Elsevier Science Publishers, New York, NY), pp 427-430, 1987.

D.2 Li, W. and Pan, C.H.T., "A New Numerical Technique for the Analysis of Lubricating Films. Part II: Precision and Convergence," *Institution of Mechanical Engineers Conference Publications*, pp. 47-52, 1987.

List of Appendices

A – Sommerfeld and Ocvirk Solutions

B – Summary of the Elrod Cavitation Algorithm

C – Bisection Method

D – Concatenation Solution to the Two-dimensional Reynolds Equation

E – Matlab Computer Code

F – Powerpoint Presentation Slides from Thesis Defense

Appendix A – Sommerfeld and Ocvirk Solutions

A.1 Sommerfeld Long Bearing Solution

The Sommerfeld solution is a long bearing solution to the Reynolds equation for the special case when the rupture point $\theta_{rup} = \theta_{form} + 2\pi$, which makes the solution in a circular bearing periodic. This solution does not consider cavitation and is applicable only with light loads when the fluid can support large negative pressures The solution is given here with accompanying solutions for eccentricities $\varepsilon = 0.4$, 0.6 and 0.8.

The non-dimensional pressure P was given in Equations (2-8) and (2-9) which is given here with correct Sommerfeld limits of $\theta_{form} = 0$ and $\theta_{form} \leq \theta \leq \theta_{form}+2\pi$.

$$P = \int_{\theta_{form}}^{\theta} \frac{d\theta}{(1+\varepsilon\cos\theta)^2} - H_0 \int_{\theta_{form}}^{\theta} \frac{d\theta}{(1+\varepsilon\cos\theta)^3} = J_2 - H_0 J_3 \qquad \text{(A-1)}$$

The invariant non-dimensional flux given by (2-11) also with the limits replaced.

$$H_0 = \frac{J_2}{J_3} = \frac{\displaystyle\int_{\theta_{form}}^{\theta_{form}+2\pi} \frac{d\theta}{(1+\varepsilon\cos\theta)^2}}{\displaystyle\int_{\theta_{form}}^{\theta_{form}+2\pi} \frac{d\theta}{(1+\varepsilon\cos\theta)^3}} \qquad \text{(A-2)}$$

The necessary integrals given by equation (3-1) and (3-2)

$$J_2 = \left[\frac{-\varepsilon\sin\theta}{(1-\varepsilon^2)(1+\varepsilon\cos\theta)}\right]_{\theta_{form}}^{\theta} + \frac{1}{(1-\varepsilon^2)} J_1 \qquad \text{(A-3)}$$

$$J_3 = \left[\frac{-\varepsilon\sin\theta}{2(1-\varepsilon^2)(1+\varepsilon\cos\theta)^2}\right]_{\theta_{form}}^{\theta} + \frac{3}{2(1-\varepsilon^2)} J_2 - \frac{1}{2(1-\varepsilon^2)} J_1 \qquad \text{(A-4)}$$

$$J_1 = \frac{2}{\sqrt{1-\varepsilon^2}} \operatorname{atan2}\left(\sqrt{1-\varepsilon^2}\sin\frac{(\theta-\theta_{form})}{2},\ \cos\frac{(\theta-\theta_{form})}{2} + \varepsilon\cos\frac{(\theta+\theta_{form})}{2}\right) \qquad \text{(A-5)}$$

The above formulas give the same results as the accepted Sommerfeld solution using the Sommerfeld substitution first derived back in 1904 [A-1]:

$$P = \frac{\varepsilon(2+\varepsilon\cos\theta)\sin\theta}{(2+\varepsilon^2)(1+\varepsilon\cos\theta)^2} \tag{A-6}$$

$$H_0 = \frac{2(1-\varepsilon^2)}{(2+\varepsilon^2)} \tag{A-7}$$

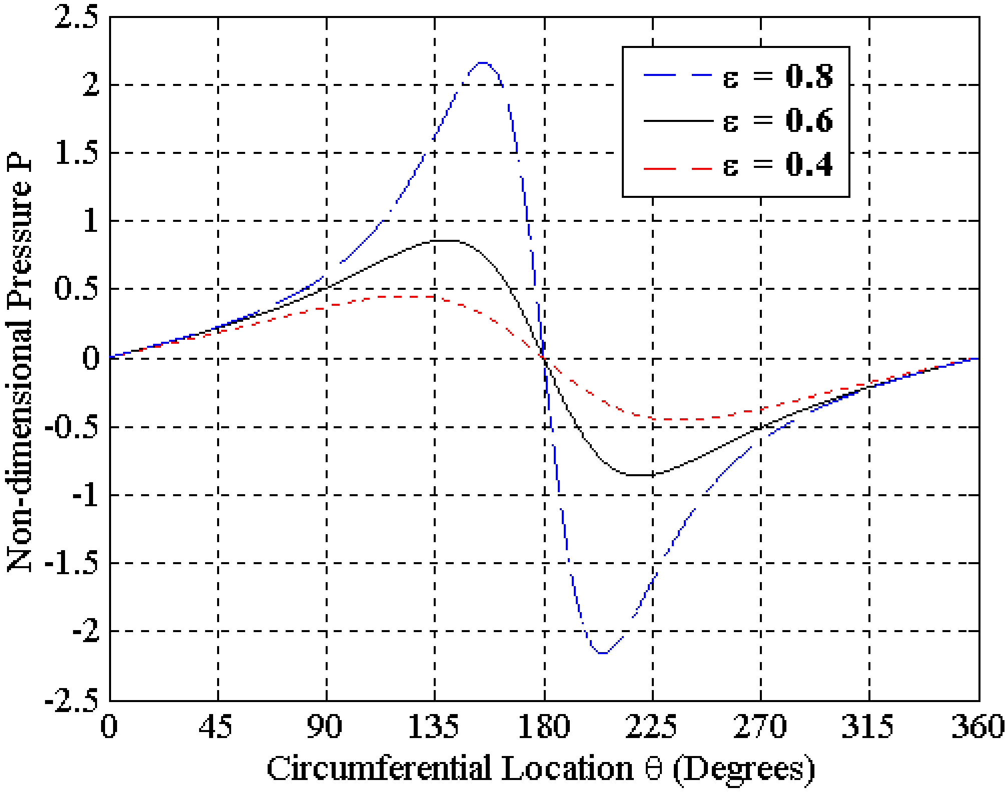

Figure A-1. Sommerfeld long bearing solution for ε = 0.4, 0.6 and 0.8.

A.2 Ocvirk Short Bearing Solution

The short bearing solution [A.2] gives an approximation to the full Reynolds equation given by Equation (2-1) when the L / D ratio is less than 1, based on the simpler differential equation:

$$\frac{\partial}{\partial z}\left(\frac{h^3}{\mu}\frac{\partial p}{\partial z}\right) = 6U\frac{\partial h}{\partial x} \tag{A-8}$$

Integrating twice with respect to z

$$p - p_0 = \frac{6\mu U}{h^3}\frac{dh}{dx}\frac{z^2}{2} + c_1 z + c_2 \tag{A-9}$$

where p_0 is the ambient pressure. The pressure is assumed to be at ambient on the ends:

$$p = p_0 \ @\ z = \pm L / 2 \tag{A-10}$$

This results in two equations with two unknown integration constants, c_1 and c_2:

$$0 = \frac{3\mu U}{h^3}\frac{dh}{dx}\frac{L^2}{4} + c_1\frac{L}{2} + c_2 \tag{A-11}$$

$$0 = \frac{3\mu U}{h^3}\frac{dh}{dx}\frac{L^2}{4} - c_1\frac{L}{2} + c_2 \tag{A-12}$$

Adding the two equations results in one of the two constants

$$c_2 = -\frac{3\mu U L^2}{4h^3}\frac{dh}{dx} \tag{A-13}$$

Substituting into Equation (A-11) gives $c_1 = 0$. Placing (A-13) back into (A-9) and solving for p-p_0 in successive steps:

$$p - p_0 = \frac{3\mu U}{h^3}\frac{dh}{dx}z^2 - \frac{3\mu U}{4h^3}\frac{dh}{dx}L^2 \tag{A-14}$$

$$p - p_0 = \frac{3\mu U}{h^3}\frac{dh}{dx}\left(z^2 - \frac{L^2}{4}\right) \tag{A-15}$$

Introducing non-dimensional terms: $H = \frac{h}{C}$, $\theta = \frac{x}{R}$, $P = (p - p_0)\frac{RC^2}{3\mu U}$ gives the non-dimensional pressure P

$$P = \frac{1}{H^3}\frac{dH}{dx}\left(z^2 - \frac{L^2}{4}\right) \tag{A-17}$$

Differentiating the non-dimensional film thickness H given by Equation (2-5) with respect to θ gives

$$\frac{dH}{d\theta} = -\varepsilon \sin\theta \tag{A-18}$$

which results in the final expression for the non-dimensional pressure

$$P(\theta, z) = \left(\frac{L^2}{4} - z^2\right) \frac{\varepsilon \sin\theta}{(1 + \varepsilon \cos\theta)^3} \tag{A-19}$$

A three-dimensional plot produced from Equation (A-19) is given in Figure A-2 for ε = 0.6.

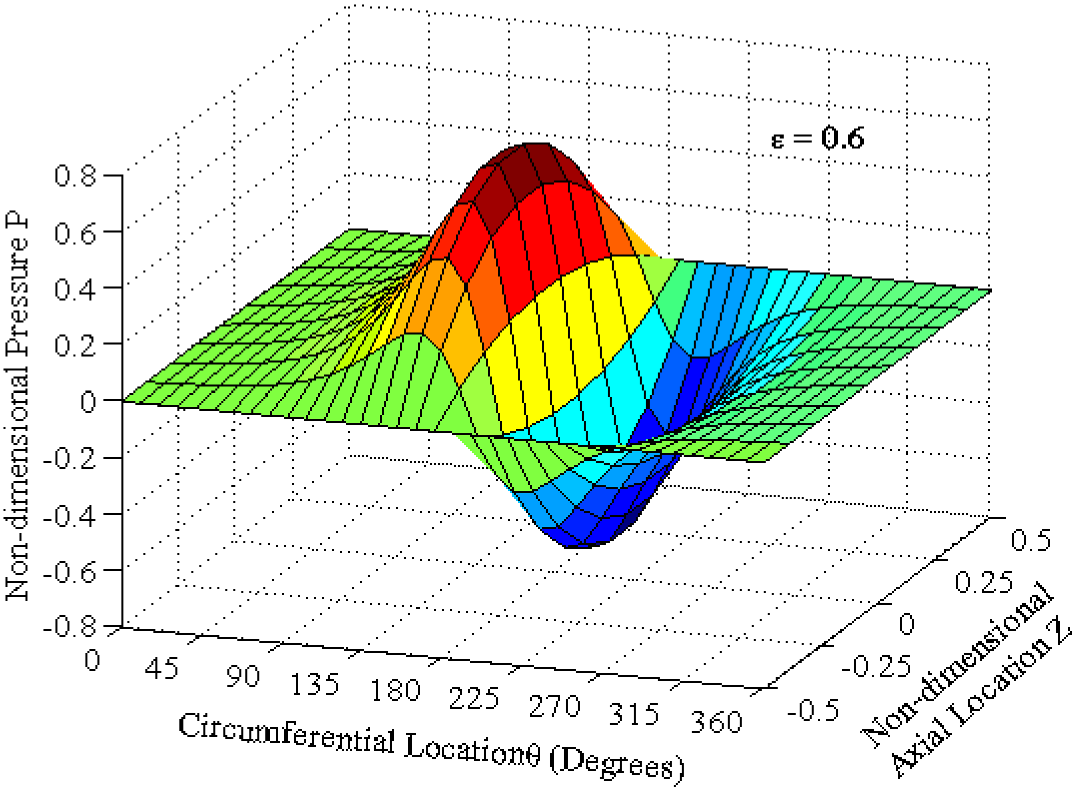

Figure A-2. Ocvirk short bearing solution for ε = 0.6.

Appendix B – Summary of the Elrod Cavitation Algorithm

B.1 Overview of the Elrod Cavitation Algorithm

The Elrod algorithm is reviewed to determine its effectiveness in applying the Reynolds equation to model flow inside a journal bearing that includes the effects of cavitation. The original objective to make a direct comparison to the integration results in the main work was not achieved, but some insight into the behavior of the Elrod algorithm was revealed. The particular scheme employed here was developed by Vijayaraghavan and Keith [B.1] and includes higher-order artificial viscosity to avoid overshoot at the rupture boundary and to control unstable oscillations. An ADI (alternate direction implicit) block iterative method was used to converge rapidly and march in time. Regardless of its popular acceptance, the Elrod algorithm is deficient in not treating the Olsson equation with reference to its dependence on the morphology model for the ruptured region; thus it has indirectly inspired the present work.

B.2 Literature Review

With the advent of the digital computer, more complex numerical analysis in bearing lubrication became practical. Elrod and Adams [B.2] proposed an algorithm employing a switch function to handle both the full-film and cavitated regions with a pseudo-compressibility concept; finite difference computation of the one-dimensional problem was furnished to illustrate the method. Elrod [B.3] published a refinement of his cavitation algorithm featuring the ADI technique for time-domain two-dimensional simulation of rupture presence in the bearing film.

The Elrod cavitation algorithm has gained widespread acceptance. Some researchers simply made use of the method to solve particular problems, others adapted portions of the technique, others added refinements, still others developed their own algorithm using the same basic concepts. Bayada [B.4] uses the finite element method to analyze under what conditions cavitation takes place. Bayada et al. [B.5] offered an improved finite element method with the addition of a fluid transport model. Woods and Brewe [B.6] added multigrid techniques to speed convergence. Vijayaraghavan and Keith [B.7] included artificial viscosity and applications to misaligned shafts and various fluid re-supply locations. Kumar and Booker [B.8] compared the finite element method to published experimental results for various bearing configurations. Claro and Miranda [B.9] studied variable supply grooves. Yu and Keith [B.10] made an attempt to identify rupture location correctly with boundary elements through interpolation between successive time steps. The roster is undoubtedly still growing.

B.3 Comprehensive Bearing Analysis

Fluid flow analysis is only one necessary aspect for a complete journal bearing design. Knowledge of flow and fluid pressure are helpful for predicting performance, however, in choosing the best design, one must also consider the interaction of the fluid with the rotor and bushing in terms of other aspects such as heat transfer and structural dynamics. There have been numerous attempts to put together comprehensive bearing analysis computational packages, including many using the Elrod cavitation algorithm, which give predictable results under intended operating conditions and constraints considering multiple aspects.

Kohno et al. [B.11], in order to take into account elastic deformation on the bearing due to loading effects, combined a boundary element method using the Reynolds equation with a finite element structural analysis model on both the journal and bushing into a single iterative numerical scheme. No mention of cavitation is given and the authors have to make simplifications to reduce computations by not considering journal rotation (low-speed condition). Sui et al. [B.12] use the Elrod cavitation algorithm with rotor elastic deformation analysis on the fuel injection pump of a diesel engine. Vijayaraghavan et al. [B.13] incorporate heat conduction to the bearing and bushing along with the Elrod algorithm running the code on a Cray XMP computer. Hirami et al. [B.14] employ a simplified analytical formulation for a finite-length two-dimensional solution including power loss and temperature considerations on viscosity for an engine crankshaft. Mourelatos [B.15] use a finite element method for structural analysis coupled with the half-Sommerfeld solution to reduce computations. It is clear that for bearing analysis packages considering multiple aspects, each of the components must be made as compact as possible in order to reduce complexity and excessive computation.

B.4 Governing Equations

Elrod's cavitation algorithm employs a single governing equation for both the full-film and partial-film zones**.** The binary switch function g is used with the pressure terms enabling different fluid behavior in both regions. The two-dimensional Reynolds elliptical equation for the full-film region with g set to 1 is:

$$\frac{\partial \rho h}{\partial t} + \frac{\partial}{\partial x}\left(\frac{\rho hU}{2} - g \frac{\rho h^{3}}{12\,\mu} \frac{\partial p}{\partial x} \right) + \frac{\partial}{\partial z}\left(- g \frac{\rho h^{3}}{12\,\mu} \frac{\partial p}{\partial z} \right) = 0 \qquad \text{(B-1)}$$

where x is the circumferential direction, z is the axial direction, t is time, p is pressure, h is the film thickness, ρ is fluid density, U is the rotating journal surface speed, h is the film thickness and μ is the viscosity. In the cavitation region, g is set to 0, resulting in a hyperbolic equation with only shear terms:

$$\frac{\partial \rho h}{\partial t} + \frac{\partial}{\partial x}\left(\frac{\rho h U}{2}\right) = 0 \qquad \text{(B-2)}$$

In place of pressure p, Equation (B-1) is arranged to solve for a single state variable Θ, which has a dual meaning. The relationship between p and Θ is given by

$$\Theta = \exp^{\left(\frac{p - p_o}{g\beta}\right)} \qquad \text{(B-3)}$$

where p_0 is the supply pressure (considered ambient here) and β is the bulk modulus introduced as a pseudo-compressibility effect. In the full-film region, Θ is a ratio of densities at each point (actual over cavitated) and in the cavitated region it is the fractional film content (0 is empty and 1 is full of liquid). The adhered film thickness can be obtained from Θ according to

$$H_a = \Theta H \qquad \text{(B-4)}$$

Using non-dimensional variables, Equation (B-1) can be written in conservative form as given in Table B-1.

Table B-1. Conservative Form of the Governing Equation.

$\frac{\partial E}{\partial T}+\frac{\partial F}{\partial X}+\frac{\partial G}{\partial Z}=0$	$a_{10}=\frac{H}{4\pi}$ $a_{11}=\frac{-B}{48\pi^{2}}H^{3}g$ $a_{22}=\frac{-B}{48\left(L/D\right)^{2}}H^{3}g$
$E=H\Theta$ $F=a_{10}\Theta+a_{11}\frac{\partial\Theta}{\partial X}$ $G=a_{22}\frac{\partial\Theta}{\partial Z}$	

The parameters that need to be defined in Table B-1 are the non-dimensional film thickness H, the non-dimensional bulk modulus B, which is a measure of elasticity of the fluid, and the bearing length to diameter ratio L/B. With the appropriate finite difference expressions inserted into the conservative form – central differencing for the full-film and upwind differencing in the cavitated region, the governing equation becomes

$$\begin{aligned}
&\frac{\left(\Theta_i^{n+1}-\Theta_i^{n}\right)H_i}{\Delta T}+\frac{-1}{8\pi\Delta X}\left[g_{i+1/2}E_{i+1}+\left(2-g_{i+1/2}-g_{i-1/2}\right)E_i+\left(2-g_{i-1/2}\right)E_{i-1}\right]\\
&+\frac{-1}{8\pi\Delta X}\left[\left(1-g_{i+1/2}\right)E_i-\left(2-g_{i+1/2}-g_{i-1/2}\right)E_{i-1}+\left(1-g_{i-1/2}\right)E_{i-2}\right]\\
&=\frac{B}{48\pi^{2}\Delta X^{2}}\left[H^{3}_{i+1/2}g_{i+1}\left(\Theta_{i+1}-1\right)-\left(H^{3}_{i+1/2}+H^{3}_{i-1/2}\right)g_i\left(\Theta_i-1\right)+H^{3}_{i-1/2}g_{i-1}\left(\Theta_{i-1}-1\right)\right]\\
&+\frac{B}{48\left(L/D\right)^{2}\Delta Z^{2}}\left[H^{3}_{j+1/2}g_{j+1}\left(\Theta_{j+1}-1\right)-\left(H^{3}_{j+1/2}+H^{3}_{j-1/2}\right)g_j\left(\Theta_j-1\right)+H^{3}_{j-1/2}g_{j-1}\left(\Theta_{j-1}-1\right)\right]
\end{aligned}\tag{B-5}$$

B.5 Programming Using ADI Technique

A computer program (see Appendix E) was written in Matlab [B.16] for the simple case of ambient pressure on all four boundaries. The Alternate Direction Implicit (ADI) technique was used along with the governing equation in non-dimensional, conservative form (Equation B-5) to march in time and reach a steady state solution. With ADI, the rows are solved implicitly followed by the columns, using the Thomas algorithm as a tri-diagonal matrix solver. A Jacobi iteration method is used to find explicitly the three coefficients of the tri-diagonal matrix. Here is an overview of the ADI procedure:

Initial Setup

- Set up the node spacing in both X and Z, being sure the entire grid has two ghost cells on left and one ghost cell outside elsewhere.
- Set initial pressure to cavitation pressure.
- Calculate film thickness (including the domain edges).
- Fill interior of matrix with a rough initial guess.
- Solve for the next value of Θ, repeat until convergence is obtained

Solve for all the rows explicitly one at a time

- Reset the tri-diagonal coefficients.
- Update the right-hand side vector explicitly.
- Apply boundary conditions for the rows.
- Call the tri-diagonal solver for the rows.
- Replace the row with solution.

Solve for all the columns explicitly one at a time

- Reset the tri-diagonal coefficients of the columns.
- Update the right-hand side explicitly.
- Apply the boundary conditions.
- Call the tri-diagonal solver.
- Replace column with solution for next iteration and calculate error.
- Reset switch function
- Calculate spectral radius for convergence test.
- Extract pressure (full-film region) or film thickness (cavitation region) and plot results.
- Update time.

The computational molecule for the tri-diagonal solver can be found in Figure B-1 to give the concept of how Equation (B-3) is divided. In solving for the rows, A_2, A_0 and A_1 are used with the solver and A_3 updates the right-hand side explicitly. In solving for the columns, A_4, A_0 and A_5 are used with the tri-diagonal solver. To preserve balance in time with the ADI technique, Vijayaraghavan and Keith [B.1] break up Equation B-3, so only roughly half of terms are inserted into the diagonal solver coefficients. The remainder are brought over to the right-hand side and considered as constants during calculations in one particular direction (either axial or circumferential).

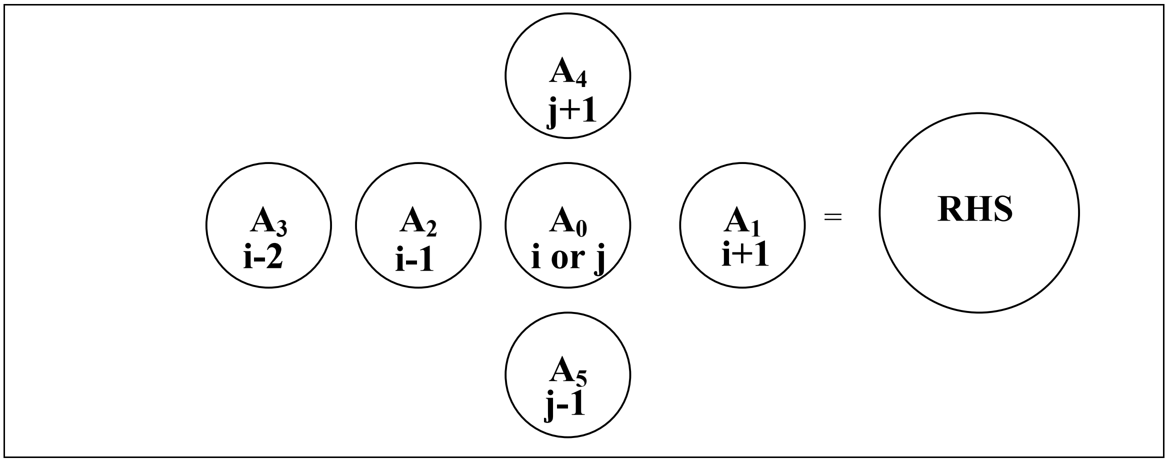

Figure B-1. Computational molecule for ADI technique.

$$
\begin{aligned}
&\left[\frac{\Delta T}{8\pi H_i \Delta X}\left(2-g_{i-1/2}\right)H_{i-1}+\frac{B\Delta T}{48\pi^2 H_i \Delta X^2}\left(H^3_{i-1/2}g_{i-1}\right)\right]\Theta_{i-1}\\
&+\left[\omega+\frac{\Delta T}{8\pi H_i \Delta X}\left(2-g_{i+1/2}-g_{i-1/2}\right)H+\frac{B\Delta T}{48\pi^2 H_i \Delta X^2}\left(H^3_{i+1/2}+H^3_{i-1/2}\right)g_i+\frac{B\Delta T}{48\left(L/D\right)^2 H_i \Delta Z^2}\left(H^3_{j+1/2}+H^3_{j-1/2}\right)g_j\right]\Theta_i\\
&+\left[\frac{\Delta T}{8\pi H_i \Delta X}\left(g_{i+1/2}H_{i+1}\right)+\frac{-B\Delta T}{48\pi^2 H_i \Delta X^2}\left(H^3_{i+1/2}g_{i+1}\right)\right]\Theta_{i+1}\\
&=\left[\frac{B\Delta T}{48\left(L/D\right)^2 H_i \Delta Z^2}H^3_{j-1/2}g_{j-1}\right]\Theta_{j-1}+\left[\omega+\frac{-\Delta T}{8\pi H_i \Delta X}\left(1-g_{i+1/2}\right)H_i\right]\Theta_i\\
&+\left[\frac{B\Delta T}{48\left(L/D\right)^2 H_i \Delta Z^2}\left(H^3_{j+1/2}g_{j+1}\right)\right]\Theta_{j+1}\\
&+\left[\frac{-\Delta T}{8\pi H_i \Delta X}\left(1-g_{i-1/2}\right)H_{i-2}\right]\Theta_{i-2}+\left[\frac{\Delta T}{8\pi H_i \Delta X}\left(2-g_{i+1/2}-g_{i-1/2}\right)H_{i-1}\right]\Theta_{i-1}\\
&+\frac{-B\Delta T}{48\pi^2 H_i \Delta X^2}\left(H^3_{i+1/2}g_{i+1}\right)+\frac{B\Delta T}{48\pi^2 H_i \Delta X^2}\left(H^3_{i+1/2}+H^3_{i-1/2}\right)g_i+\frac{-B\Delta T}{48\pi^2 H_i \Delta X^2}\left(H^3_{i-1/2}g_{i-1}\right)\\
&+\frac{-B\Delta T}{48\left(L/D\right)^2 H_i \Delta Z^2}\left(H^3_{j+1/2}g_{j+1}\right)+\frac{B\Delta T}{48\left(L/D\right)^2 H_i \Delta Z^2}\left(H^3_{j+1/2}+H^3_{j-1/2}\right)g_j+\frac{-B\Delta T}{48\left(L/D\right)^2 H_i \Delta Z^2}\left(H^3_{j-1/2}g_{j-1}\right)
\end{aligned}
$$

Figure B-2. Solving for rows explicitly.

$$A_2 = \frac{\Delta T}{8\pi H_i \Delta X}\left(2 - g_{i-\frac{1}{2}}\right)H_{i-1} + \frac{B\Delta T}{48\pi^2 H_i \Delta X^2}\left(H^3_{i-\frac{1}{2}} g_{i-1}\right)$$

$$A_0 = \omega + \frac{\Delta T}{8\pi H_i \Delta X}\left(2 - g_{i+\frac{1}{2}} - g_{i-\frac{1}{2}}\right)H + \frac{B\Delta T}{48\pi^2 H_i \Delta X^2}\left(H^3_{i+\frac{1}{2}} + H^3_{i-\frac{1}{2}}\right)g_i$$
$$+ \frac{B\Delta T}{48\left(L/D\right)^2 H_i \Delta Z^2}\left(H^3_{j+\frac{1}{2}} + H^3_{j-\frac{1}{2}}\right)g_j$$

$$A_1 = \frac{\Delta T}{8\pi H_i \Delta X}\left(g_{i+\frac{1}{2}} H_{i+1}\right) + \frac{-B\Delta T}{48\pi^2 H_i \Delta X^2}\left(H^3_{i+\frac{1}{2}} g_{i+1}\right)$$

$$A_{5,\exp} = \frac{B\Delta T}{48\left(L/D\right)^2 H_i \Delta Z^2} H^3_{j-\frac{1}{2}} g_{j-1}$$

$$A_{0,\exp} = \omega + \frac{-\Delta T}{8\pi H_i \Delta X}\left(1 - g_{i+\frac{1}{2}}\right)H_i$$

$$A_{4,\exp} = \frac{B\Delta T}{48\left(L/D\right)^2 H_i \Delta Z^2}\left(H^3_{j+\frac{1}{2}} g_{j+1}\right)$$

$$A_{3,\exp} = \frac{\Delta T}{8\pi H_i \Delta X}\left(2 - g_{i+\frac{1}{2}} - g_{i-\frac{1}{2}}\right)H_{i-1}$$

$$A_{2,\exp} = \frac{-\Delta T}{8\pi H_i \Delta X}\left(1 - g_{i-\frac{1}{2}}\right)H_{i-2}$$

$$RHS_{constant} = \frac{-B\Delta T}{48\pi^2 H_i \Delta X^2}\left(H^3_{i+\frac{1}{2}} g_{i+1}\right) + \frac{B\Delta T}{48\pi^2 H_i \Delta X^2}\left(H^3_{i+\frac{1}{2}} + H^3_{i-\frac{1}{2}}\right)g_i + \frac{-B\Delta T}{48\pi^2 H_i \Delta X^2}\left(H^3_{i-\frac{1}{2}} g_{i-1}\right)$$
$$+ \frac{-B\Delta T}{48\left(L/D\right)^2 H_i \Delta Z^2}\left(H^3_{j+\frac{1}{2}} g_{j+1}\right) + \frac{B\Delta T}{48\left(L/D\right)^2 H_i \Delta Z^2}\left(H^3_{j+\frac{1}{2}} + H^3_{j-\frac{1}{2}}\right)g_j + \frac{-B\Delta T}{48\left(L/D\right)^2 H_i \Delta Z^2}\left(H^3_{j-\frac{1}{2}} g_{j-1}\right)$$

Figure B-3. Tri-diagonal coefficients for solving rows.

$$
\left[\frac{-B\Delta T}{48\left(L/D\right)^{2}H_{i}{}^{2}}H^{3}_{j-1/2}g_{j-1}\right]\Theta_{j-1}
$$

$$
+\left[\omega+\frac{\Delta T}{8\pi\pi_{i}\Delta X}\left(2-g_{i+1/2}-g_{i-1/2}\right)H_{i}+\frac{B\Delta T}{48\pi^{2}H_{i}\Delta X^{2}}\left(H^{3}_{i+1/2}+H^{3}_{i-1/2}\right)g_{i}+\frac{B\Delta T}{48\left(L/D\right)^{2}H_{i}\Delta Z^{2}}\left(H^{3}_{j+1/2}+H^{3}_{j-1/2}\right)g_{j}\right]\Theta_{i}
$$

$$
+\left[\frac{-B\Delta T}{48\left(L/D\right)^{2}H_{i}\Delta Z^{2}}\left(H^{3}_{j+1/2}g_{j+1}\right)\right]\Theta_{j+1}
$$

$$
=\left[\frac{-\Delta T}{8\pi\pi_{i}\Delta X}\left(1-g_{i-1/2}\right)H_{i-2}\right]\Theta_{i-2}
$$

$$
+\left[\begin{array}{l}\dfrac{-\Delta T}{8\pi H_{i}\Delta X}\left(2-g_{i-1/2}\right)H_{i-1}+\dfrac{\Delta T}{8\pi H_{i}\Delta X}\left(2-g_{i+1/2}-g_{i-1/2}\right)H_{i-1}\\ +\dfrac{B\Delta T}{48\pi^{2}H_{i}\Delta X^{2}}\left(H^{3}_{i-1/2}g_{i-1}\right)\end{array}\right]\Theta_{i-1}
$$

$$
+\left[\omega+\frac{-\Delta T}{8\pi H_{i}\Delta X}\left(1-g_{i+1/2}\right)H_{i}\right]\Theta_{i}
$$

$$
+\left[\frac{-\Delta T}{8\pi H_{i}\Delta X}\left(g_{i+1/2}H_{i+1}\right)+\frac{B\Delta T}{48\pi^{2}H_{i}\Delta X^{2}}\left(H^{3}_{i+1/2}g_{i+1}\right)\right]\Theta_{i+1}
$$

$$
\frac{-B\Delta T}{48\pi^{2}H_{i}\Delta X^{2}}\left(H^{3}_{i+1/2}g_{i+1}\right)+\frac{B\Delta T}{48\pi^{2}H_{i}\Delta X^{2}}\left(H^{3}_{i+1/2}+H^{3}_{i-1/2}\right)g_{i}+\frac{-B\Delta T}{48\pi^{2}H_{i}\Delta X^{2}}\left(H^{3}_{i-1/2}g_{i-1}\right)
$$

$$
+\frac{-B\Delta T}{48\left(L/D\right)^{2}H_{i}\Delta Z^{2}}\left(H^{3}_{j+1/2}g_{j+1}\right)+\frac{B\Delta T}{48\left(L/D\right)^{2}H_{i}\Delta Z^{2}}\left(H^{3}_{j+1/2}+H^{3}_{j-1/2}\right)g_{j}+\frac{-B\Delta T}{48\left(L/D\right)^{2}H_{i}\Delta Z^{2}}\left(H^{3}_{j-1/2}g_{j-1}\right)
$$

Figure B-4. Solving for columns explicitly.

$$A_5 = \frac{-B\Delta T}{48\left(L/D\right)^2 H_i \Delta Z^2} H^3_{j-1/2} g_{j-1}$$

$$A_0 = \omega + \frac{\Delta T}{8\pi H_i \Delta X}\left(2 - g_{i+1/2} - g_{i-1/2}\right)H + \frac{B\Delta T}{48\pi^2 H_i \Delta X^2}\left(H^3_{i+1/2} + H^3_{i-1/2}\right)g_i$$
$$+ \frac{B\Delta T}{48\left(L/D\right)^2 H_i \Delta Z^2}\left(H^3_{j+1/2} + H^3_{j-1/2}\right)g_j$$

$$A_4 = \frac{-B\Delta T}{48\left(L/D\right)^2 H_i \Delta Z^2}\left(H^3_{j+1/2} g_{j+1}\right)$$

$$A_{3,\exp} = \frac{\Delta T}{8\pi H_i \Delta X}\left(2 - g_{i+1/2} - g_{i-1/2}\right)H_{i-1}$$

$$A_{2,\exp} = \frac{-\Delta T}{8\pi H_i \Delta X}\left(1 - g_{i-1/2}\right)H_{i-2} + \frac{-\Delta T}{8\pi H_i \Delta X}\left(2 - g_{i-1/2}\right)H_{i-1} + \frac{-B\Delta T}{48\pi^2 H_i \Delta X^2}\left(H^3_{i-1/2} g_{i-1}\right)$$

$$A_{0,\exp} = \omega + \frac{-\Delta T}{8\pi H_i \Delta X}\left(1 - g_{i+1/2}\right)H_i$$

$$A_{1,\exp} = \frac{-\Delta T}{8\pi H_i \Delta X}\left(g_{i+1/2} H_{i+1}\right) + \frac{B\Delta T}{48\pi^2 H_i \Delta X^2}\left(H^3_{i+1/2} g_{i+1}\right)$$

$$RHS_{\text{constant}} = \frac{-B\Delta T}{48\pi^2 H_i \Delta X^2}\left(H^3_{i+1/2} g_{i+1}\right) + \frac{B\Delta T}{48\pi^2 H_i \Delta X^2}\left(H^3_{i+1/2} + H^3_{i-1/2}\right)g_i + \frac{-B\Delta T}{48\pi^2 H_i \Delta X^2}\left(H^3_{i-1/2} g_{i-1}\right)$$
$$+ \frac{-B\Delta T}{48\left(L/D\right)^2 H_i \Delta Z^2}\left(H^3_{j+1/2} g_{j+1}\right) + \frac{B\Delta T}{48\left(L/D\right)^2 H_i \Delta Z^2}\left(H^3_{j+1/2} + H^3_{j-1/2}\right)g_j + \frac{-B\Delta T}{48\left(L/D\right)^2 H_i \Delta Z^2}\left(H^3_{j-1/2} g_{j-1}\right)$$

Figure B-5. Tri-diagonal coefficients for solving columns.

B.6 Remarks on the Elrod Cavitation Algorithm

Arbitrarily choosing L/D =1 and ε = 0.6, the following settings were obtained by trial and error in order to obtain a solution with the smallest grid spacing that was still able to converge:

- Grid spacing 24 x 16
- $\Delta t = 0.00001$
- $\beta = 12{,}500$

The Matlab [B-16] program can be found in Appendix E.5. Steady-state results obtained from are given in Figure B-1.

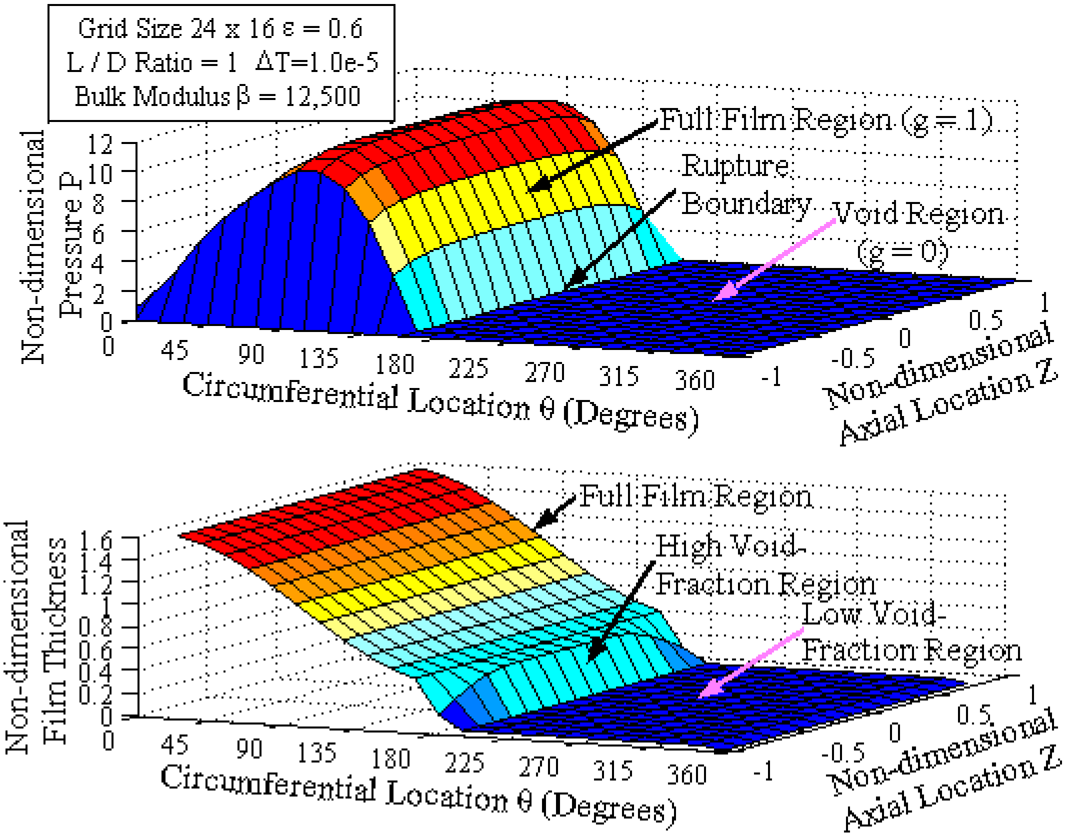

Figure B-1. Solution to Elrod cavitation algorithm.

When using Elrod's switch function, the same value of the non-dimensional bulk modulus B is applied to both the full-film and void regions, intended as a pseudo-compressibility effect. The bulk modulus β normally represents a fluid's elasticity and a typical value for lubricating oil is 1.6 x 10^9 N/m^2. In the example used here, inserting values for a reasonable size bearing geometry into the expression for the non-dimensional bulk modulus would suggest

$$B = \frac{\beta C^2}{\mu UR} = 1.6 \text{ x } 10^9 \text{ N/m}^2 \frac{(0.0005\text{m})^2}{0.05\text{Pa}\cdot\text{s}\left(1\frac{\text{m}}{\text{s}}\right)(0.05\text{m})} = 160{,}000 \qquad \text{(B-6)}$$

whereas an actual value B = 12,500 was used in order to get a stable system of equations. The numerically employed bulk modulus is on the order of 1/10 less than realistic for a lubricating oil; the system of equations is in effect much stiffer than physical reality would suggest. Non-dimensional B will depend on the grid size, L/D ratio, and other aspects of the particular bearing geometry (locations and dimensions of the supply groove, and external pressures), and must be found by trial and error for each case.

A second, and perhaps more important, observation has to do with the morphology of the fluid and the concept of slow creep. In the main part of this work, it is argued that the adhered film in the cavitation zone travels along with the rotating surface and further the void fraction α (ratio of H_a/H) at rupture points should be equal to ½. If it is further confirmed by experiment that this hypothesis is indeed valid for some operating conditions, then it will be difficult to implement Elrod's algorithm to take into account this phenomenon. With Elrod's algorithm, although the location of the steady-state rupture points are roughly in the right vicinity as determined by whether grid points have a Θ value greater 1 or not, their actual locations are not well defined. As can also be seen in Figure B-1, the adhered film profile has a void fraction on the order of ½ (and certainly, not exactly) only at the first, single grid point in the circumferential direction that is not considered full-film ($\Theta < 1$). The next grid point downstream immediately has a void fraction very close to 0. Certainly the exact rupture location can be identified more closely by using many more grid points, but then the method's use in comprehensive bearing analyses seems much less practical. There appears very little that can be done to remedy the deficiency of the adhered film.

Much development has taken place to make Elrod's algorithm more practical since its original introduction. Although the idea of a single governing equation for the entire bearing is intriguing, it is questioned how much more effort should continue. The physical unreality of the pseudo-compressibility effect, knowledge of the rupture locations obtained only at great computational expense and failure to address a two-phase morphology are three reasons to consider other alternatives for journal bearing analysis.

Appendix C – Bisection Method

The bisection method is a series of steps performed iteratively which are used to reliably and accurately find the Swift-Stieber point θ_{SS} for a given formation point θ_{form}. The pressure gradient $\left(\frac{dP}{d\theta}\right)_{rup}$ can be found at any point θ_{rup} according to the following two-step procedure:

1. Determine the invariant flux at maximum pressure, expressed in compact form, $H_0 = \frac{J_2}{J_3}$, where J_2 and J_3 are the Reynolds equation integrals formulated in Section 3.1. J_2 and J_3 are both evaluated with a lower limits of θ_{form} and an upper limit θ_{rup}.

2. Calculate the pressure gradient at rupture based on Equation (3-10) which is evaluated at the rupture point, given here by

$$\left(\frac{dP}{d\theta}\right)_{rup} = \frac{1}{H_{rup}^2} - \frac{H_0}{H_{rup}^3} \tag{C-1}$$

where H_{rup} is the non-dimensional film thickness at rupture.

To speed the procedure along, it can be observed that the pressure is always positive at θ_0 corresponding to the maximum H_0, and the minimum θ_{SS} that is being searched for will always be greater than $\theta = 180°$. In incrementing the upper limit θ_{rup} starting at 180° over a coarse grid of one grid point every degree, the location of θ_{SS} can be determined to be in the interval [a,b] where b is the first occurrence of θ_{rup} where the pressure gradient changes sign from negative to positive and a is the previous evaluation with θ_{rup} (which will have still resulted in a negative pressure gradient). Taking m as the midpoint of [a,b], there are three possibilities:

- The value of $\frac{dP}{d\theta}(m)$ is exactly 0; then m is the correct final value of θ_{SS}.
- $\frac{dP}{d\theta}(m) * \frac{dP}{d\theta}(a) < 0$; then the final value of θ_{SS} is in the interval [a,m] .
- $\frac{dP}{d\theta}(m) * \frac{dP}{d\theta}(b) < 0$; then the final value of θ_{SS} is in the interval [m,b].

Now, the same two step procedure can be repeated with the smaller of the two intervals, i.e., [a,m] or [m,b], thus reducing by half the span over which θ_{SS} may exist each time. The interval size is halved again and again until the result is less than a small number δ away from zero, thus yielding an accurate approximation to the final value of the Swift-Stieber point θ_{SS}.

Appendix D – Concatenation Solution to the Two-dimensional Reynolds Equation

D.1 Background

The one-dimensional exact solution of Reynolds equation can be adapted to treat two-dimensional problems of Reynolds equation along computational mesh lines. A mesh line solution of the circumferential pressure profile would include a particular constant along each mesh line. The word concatenation is used here to indicate that the two-dimensional numerical solution is a collection of interconnected mesh line solutions. In earlier attempts to develop such a computation method, Pan, Perlman and Li [D.1] used a secant approximation for the film thickness along the mesh line. Even with such a crude approximation, improvement over conventional Finite Difference Method (FDM) is quite apparent. To this end, the concatenation method is developed fully here without considering cavitation.

A subsequent attempt of a similar technique for the plane slider was named L.E.P.D.E.M for Locally Exact Partial Differentiation Method [D.2]. The exact bearing film geometry is used here along with the introduction of continuous Reynolds equation integrals. The derivation of the method is performed for the simplest possible formulation referred to as the one cell case and then the necessary equations and the matrix assembly method are shown for the formulation of a 3 x 3 case. Symmetry considerations and use of a banded matrix solver are implemented to reduce the size of the matrix for computational purposes. Results from a computer programmed solution are then given for the arbitrary M x N case for both a short bearing and a long bearing arrangements showing the effectiveness of the method (see Appendix E.4).

Concatenation provides a systematic approach in order to set up a system of equations involving both unknown pressures and fluxes that generates a pressure profile while ensuring two-dimensional continuity of the flow. An advantage of concatenation over other methods like finite element methods (FDM) and finite difference methods (FDM) is that it only requires a relatively coarse mesh to provide an accurate representation of the fluid behavior, since the values locally are solved exactly through integration. Concatenation thereby saves computational time and memory, which is practical when used in conjunction with other components of a complete bearing analysis such as heat transfer and/or rotor structural dynamics.

D.2 Concatenation for the One Cell Case

D.2.1 Pressure Cell for the One Cell Case

The entire development of the required system of equations and the corresponding solution for the pressure and fluxes of a single pressure cell referred to as the one cell case are considered before moving on to cases involving multiple cells. A diagram for a single pressure cell indicated by the shaded portion is found in Figure D-1.

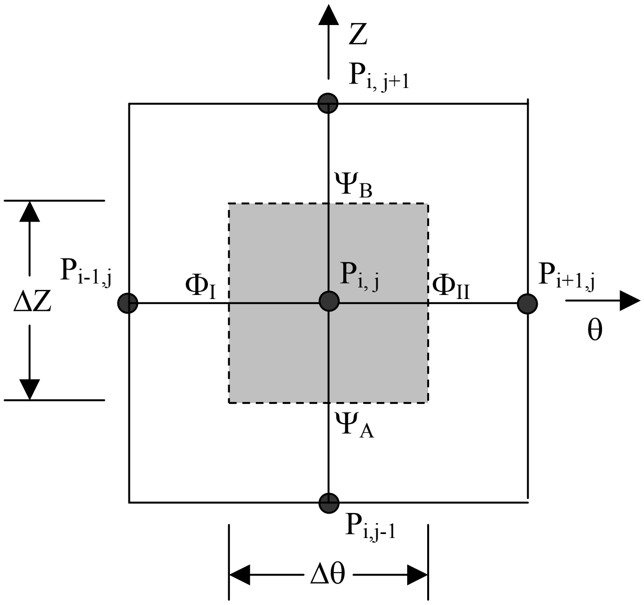

Figure D-1. Pressure cell for concatenation method.

The objective is to solve for the single pressure value $P_{i,j}$ that is located at a node at the exact center of the cell. The two non-dimensional circumferential fluxes, given by Φ_I and Φ_{II}, along with the two non-dimensional axial fluxes, given by Ψ_A and $\Psi_{B,}$ comprise the additional unknowns. The fluxes are associated with the flow through the edges of the pressure cell in either the circumferential or radial directions. The adopted sign convention is such that fluxes in the appropriate positive circumferential or radial direction are considered positive. The system of equations for the one cell case then requires five equations to solve for the five unknowns. The four external pressure values $P_{i+1,j}$, $P_{i-1,j}$, $P_{i,j+1}$ and $P_{i,j-1}$ must be specified as boundary conditions. The formulation begins with dimensional equations for the fluxes ϕ, ψ in the circumferential (x) and axial

(z) directions, respectively, are given by

$$\phi = \frac{U_x h}{2} - \frac{h^3}{12\mu}\frac{\partial p}{\partial x} \tag{D-1a}$$

$$\psi = \frac{U_z h}{2} - \frac{h^3}{12\mu}\frac{\partial p}{\partial z} \tag{D-1b}$$

where U_x and U_z are surface flow speeds in their respective directions, h is the film thickness, μ is the viscosity and p is the pressure.

D.2.2 Circumferential Flux Equations for the One Cell Case

Working first with the flux ϕ in the x – direction and beginning to solve for the pressure gradient

$$\frac{12\mu\phi}{h^3} = \frac{6\mu U_x}{h^2} - \frac{\partial p}{\partial x} \tag{D-2}$$

Substituting with non-dimensional terms: $\theta = {}^{x}\!/_{R}$, $H(\theta) = {}^{h}\!/_{C} = 1 + \varepsilon\cos\theta$ and

$\partial P = \dfrac{C^2}{6\mu R U_x}\partial p$ results in:

$$\frac{2\phi}{C U_x H^3} = \frac{1}{H^2} - \frac{\partial P}{\partial \theta} \tag{D-3}$$

The non-dimensional flux in the x-direction is given by:

$$\Phi = \frac{2\phi}{C U_x} = \text{Constant} \tag{D-4}$$

Solving for the non-dimensional pressure gradient:

$$\frac{\partial P}{\partial \theta} = \frac{1}{H^2} - \frac{\Phi}{H^3} \tag{D-5}$$

Integrating with respect to θ yields the non-dimensional pressure between two adjacent cells written here in compact form

$$P_{i,j} - P_{i-1,j} = J_2 - J_3\Phi$$

(D-6)

This equation can be applied twice since there are two fluxes Φ_I and Φ_{II}, thus contributing two of the five equations necessary to complete the entire system of equations for the one cell case. J_1 and J_2 are integral expressions representing $J_2 = \int \frac{d\theta}{H^2}$ and $J_3 = \int \frac{d\theta}{H^3}$. Continuous solutions without branch point to the integrals are given by:

$$J_2 = \int_{\theta_1}^{\theta_2} \frac{d\theta}{(1+\varepsilon\cos\theta)^2} = \left[\frac{-\varepsilon\sin\theta}{(1-\varepsilon^2)(1+\varepsilon\cos\theta)}\right]_{\theta_1}^{\theta_2} + \frac{1}{(1-\varepsilon^2)}J_1 \tag{D-7}$$

$$J_3 = \int_{\theta_1}^{\theta_2} \frac{d\theta}{(1+\varepsilon\cos\theta)^3} = \left[\frac{-\varepsilon\sin\theta}{2(1-\varepsilon^2)(1+\varepsilon\cos\theta)^2}\right]_{\theta_1}^{\theta_2} + \frac{3}{2(1-\varepsilon^2)}J_2 - \frac{1}{2(1-\varepsilon^2)}J_1 \tag{D-8}$$

with the intermediate value

$$J_1 = \int \frac{d\theta}{H} = \frac{2}{\sqrt{1-\varepsilon^2}} \operatorname{atan2}\left\{\sqrt{1-\varepsilon^2}\sin\frac{(\theta_2-\theta_1)}{2}, \cos\frac{(\theta_2-\theta_1)}{2} + \varepsilon\cos\frac{(\theta_2+\theta_1)}{2}\right\}$$

(D-9)

D.2.3 Axial Flux Equations for the One Cell Case

A similar process used for Φ in the x-direction can be followed in working with the flux ψ in the z-direction, except with a distinction made of the no side flow assumption. Beginning with the flux given by Equation (D-1b) and solving for the pressure gradient:

$$\frac{\partial \mathrm{p}}{\partial \mathrm{z}} = -\frac{12\mu\psi}{\mathrm{h}^3} \tag{D-10}$$

Substituting with non-dimensional terms, assuming the length to diameter ratio L/D = α,

$\partial \mathrm{Z} = \frac{\partial \mathrm{z}}{\mathrm{L}} = \frac{\partial \mathrm{z}}{2\mathrm{R}\alpha}$, $H = h/C = 1 + \varepsilon\cos\theta$, $\partial P = \frac{C^2}{6\mu R U_x}\partial p$ results in

$$\frac{4\psi}{\mathrm{U_x CH^3}} = -\frac{\partial \mathrm{P}}{\partial \mathrm{Z}} \tag{D-11}$$

The non-dimensional flux in the z-direction is given by

$$\Psi = \frac{2\psi}{\mathrm{CU_x}} = \text{Constant} \tag{D-12}$$

Solving for the non-dimensional pressure gradient

$$\frac{\partial P}{\partial Z} = -2\frac{\Psi}{H^3} \tag{D-13}$$

Integrating with respect to Z yields the non-dimensional pressure between two adjacent cells written here in compact form

$$P_{i,j} - P_{i,j-1} = -\frac{2\Delta Z}{H^3}\Psi \tag{D-14}$$

This equation can also be applied twice since there are two fluxes Ψ_A and Ψ_B thus contributing two more equations necessary to complete the entire system of equations for the one cell case.

D.2.4 Cell Mass Continuity for the One Cell Case

In addition to the four equations for the fluxes (two axial and two circumferential), a fifth and final equation is obtained from mass continuity over the entire cell

$$\Phi_{\mathrm{I}} - \Phi_{\mathrm{II}} + \Psi_{\mathrm{A}} - \Psi_{\mathrm{B}} = 0 \tag{D-15}$$

Keeping with the adopted sign convention, if a negative value is obtained after solving, this would indicate the flux is in the negative direction (either axial or circumferential).

D.2.5 5 x 5 System of Linear Equations for the One Cell Case

The two circumferential flux equations involving Φ_{I} and Φ_{II} from Equation (D-6), the two axial flux equations Ψ_{A} and Ψ_{B} from Equation (D-14) and the continuity equation (D-15) are assembled together to yield the 5 x 5 system of linear equations which can be solved simultaneously for the internal pressure $P_{\mathrm{i,j}}$ and the four fluxes.

$$P_{i,j} - P_{i-1,j} = J_{2-I} - J_{3-I}\Phi_I \rightarrow J_{3-I}\Phi_I + P_{i,j} = J_{2-I} + P_{i-1,j} = B_1 \tag{D-16}$$

$$P_{i,j} - P_{i,j-1} = -\frac{2\Delta Z}{H^3}\Psi_A \rightarrow \frac{2\Delta Z}{H^3}\Psi_A + P_{i,j} = P_{i,j-1} = B_2 \tag{D-17}$$

$$\Phi_I - \Phi_{II} + \Psi_A - \Psi_B = 0 \tag{D-15 repeated}$$

$$P_{i,j+1} - P_{i,j} = -\frac{2\Delta Z}{H^3}\Psi_B \rightarrow -P_{i,j} + \frac{2\Delta Z}{H^3}\Psi_B = -P_{i,j+1} = B_4 \tag{D-18}$$

$$P_{i+1,j} - P_{i,j} = J_{2-II} - J_{3-II}\Phi_{II} \rightarrow -P_{i,j} + J_{3-II}\Phi_{II} = J_{2-II} - P_{i+1,j} = B_5 \tag{D-19}$$

The order of the equations above becomes clear when they are written in standard matrix notation considering symmetry:

$$\begin{bmatrix} J_{3-I} & 0 & 1 & 0 & 0 \\ 0 & \frac{2\Delta Z}{H^3} & 1 & 0 & 0 \\ -1 & -1 & 0 & 1 & 1 \\ 0 & 0 & -1 & \frac{2\Delta Z}{H^3} & 0 \\ 0 & 0 & -1 & 0 & J_{3-II} \end{bmatrix} \begin{bmatrix} \Phi_I \\ \Psi_A \\ P_{i,j} \\ \Psi_B \\ \Phi_{II} \end{bmatrix} = \begin{bmatrix} J_{2-I} + P_{i-1,j} \\ P_{i,j-1} \\ 0 \\ -P_{i,j+1} \\ J_{2-II} - P_{i+1,j} \end{bmatrix} \tag{D-20}$$

This is can be represented symbolically in the form $[A][X] = [B]$ or expanding [A]

$$\begin{bmatrix} a_{11} & 0 & 1 & 0 & 0 \\ 0 & a_{22} & 1 & 0 & 0 \\ -1 & -1 & 0 & 1 & 1 \\ 0 & 0 & -1 & a_{44} & 0 \\ 0 & 0 & -1 & 0 & a_{55} \end{bmatrix} \begin{bmatrix} X_1 \\ X_2 \\ X_3 \\ X_4 \\ X_5 \end{bmatrix} = \begin{bmatrix} B_1 \\ B_2 \\ 0 \\ B_4 \\ B_5 \end{bmatrix} \tag{D-21}$$

The four diagonal elements a_{ii} can all be determined by selection of the grid spacing (ΔZ and $\Delta\theta$) and eccentricity ε, whereas the elements of [B] are dependent on the grid setup, eccentricity and the external pressures that serve as boundary conditions. Once the grid spacing, eccentricity and external pressures are chosen, all that remains to determine the elements of [X] is to solve the system of equations given by Equation (D-20).

It is simplest to solve the entire system first for the single pressure value $P_{i,j}$ in eliminating the four fluxes. This involves first solving the individual equations containing each of the four fluxes and inserting the expressions for the fluxes into Equation (D-15).

$$\text{From (D-16),}\quad \Phi_I = \frac{J_{2-I} + P_{i-1,j} - P_{i,j}}{J_{3-I}} \tag{D-22}$$

$$\text{From (D-17),}\quad \Psi_A = \frac{H^3\left(P_{i,j-1} - P_{i,j}\right)}{2\Delta Z} \tag{D-23}$$

$$\text{From (D-18),}\quad \Psi_B = \frac{H^3\left(P_{i,j} - P_{i,j+1}\right)}{2\Delta Z} \tag{D-24}$$

$$\text{From (D-19),}\quad \Phi_{II} = \frac{J_{2-II} + P_{i,j} - P_{i+1,j}}{J_{3-II}} \tag{D-25}$$

Inserting the flux into Equation (D-15)

$$\frac{J_{2-I}+P_{i-1,j}-P_{i,j}}{J_{3-I}}-\left(\frac{J_{2-II}+P_{i,j}-P_{i+1,j}}{J_{3-II}}\right)+\left(\frac{H^3\left(P_{i,j-1}-P_{i,j}\right)}{2\Delta Z}\right)-\left(\frac{H^3\left(P_{i,j}-P_{i,j+1}\right)}{2\Delta Z}\right)=0 \tag{D-26}$$

Solving for $\mathrm{P_{i,j}}$

$$\mathrm{P_{i,j}}=\frac{\mathrm{2J_{3-II}\Delta Z(J_{2-I}+P_{i-1,j})-2J_{3-I}\Delta Z(J_{2-II}-P_{i+1,j})+H^3J_{3-I}J_{3-II}(P_{i,j-1}-P_{i,j+1})}}{\mathrm{2\Delta Z\left(J_{3-II}-J_{3-I}\right)+2H^3J_{3-I}J_{3-II}}} \tag{D-27}$$

The simplest boundary conditions, which will be done here, is to set the pressure on the boundaries equal to zero to obtain one practical solution.

$$P_{i,j}=\frac{2J_{2-I}J_{3-II}\Delta Z-2J_{2-II}J_{3-I}\Delta Z}{2\Delta Z\left(J_{3-II}-J_{3-I}\right)+2H^3J_{3-I}J_{3-II}} \tag{D-28}$$

Evaluating the integrals involving Φ_I

$$J_{2-I}=\int_{\theta-\Delta\theta}^{\theta}\frac{d\theta}{(1+\varepsilon\cos\theta)^2}=\left[\frac{-\varepsilon\sin\theta}{(1-\varepsilon^2)(1+\varepsilon\cos\theta)}\right]_{\theta-\Delta\theta}^{\theta}+\frac{1}{(1-\varepsilon^2)}J_1 \tag{D-29}$$

$$J_{3-I}=\int_{\theta-\Delta\theta}^{\theta}\frac{d\theta}{(1+\varepsilon\cos\theta)^3}=\left[\frac{-\varepsilon\sin\theta}{2(1-\varepsilon^2)(1+\varepsilon\cos\theta)^2}\right]_{\theta-\Delta\theta}^{\theta}+\frac{3}{2(1-\varepsilon^2)}J_2-\frac{1}{2(1-\varepsilon^2)}J_1 \tag{D-30}$$

$$J_{1-I}=\frac{2}{\sqrt{1-\varepsilon^2}}\mathrm{atan2}\left\{\sqrt{1-\varepsilon^2}\sin\left(\frac{\Delta\theta}{2}\right),\cos\left(\frac{\Delta\theta}{2}\right)+\varepsilon\cos\frac{(2\theta-\Delta\theta)}{2}\right\} \tag{D-31}$$

Similar expressions concerning Φ_II except limits of integration are from θ to $\theta + \Delta\theta$. The four fluxes can be obtained by inserting $\mathrm{P_{i,j}}$ (D-28) back into Equations (D-22), (D-23), (D-24) and (D-25).

D.3 Concatenation for the 3 x 3 Cell Case

Building on the development just performed for the one cell case, the 3 x 3 pressure cell case is briefly explained. The grid setup involves a square layout of 9 pressure cells -- 3 cells in both the circumferential and axial directions as shown in Figure D-2.

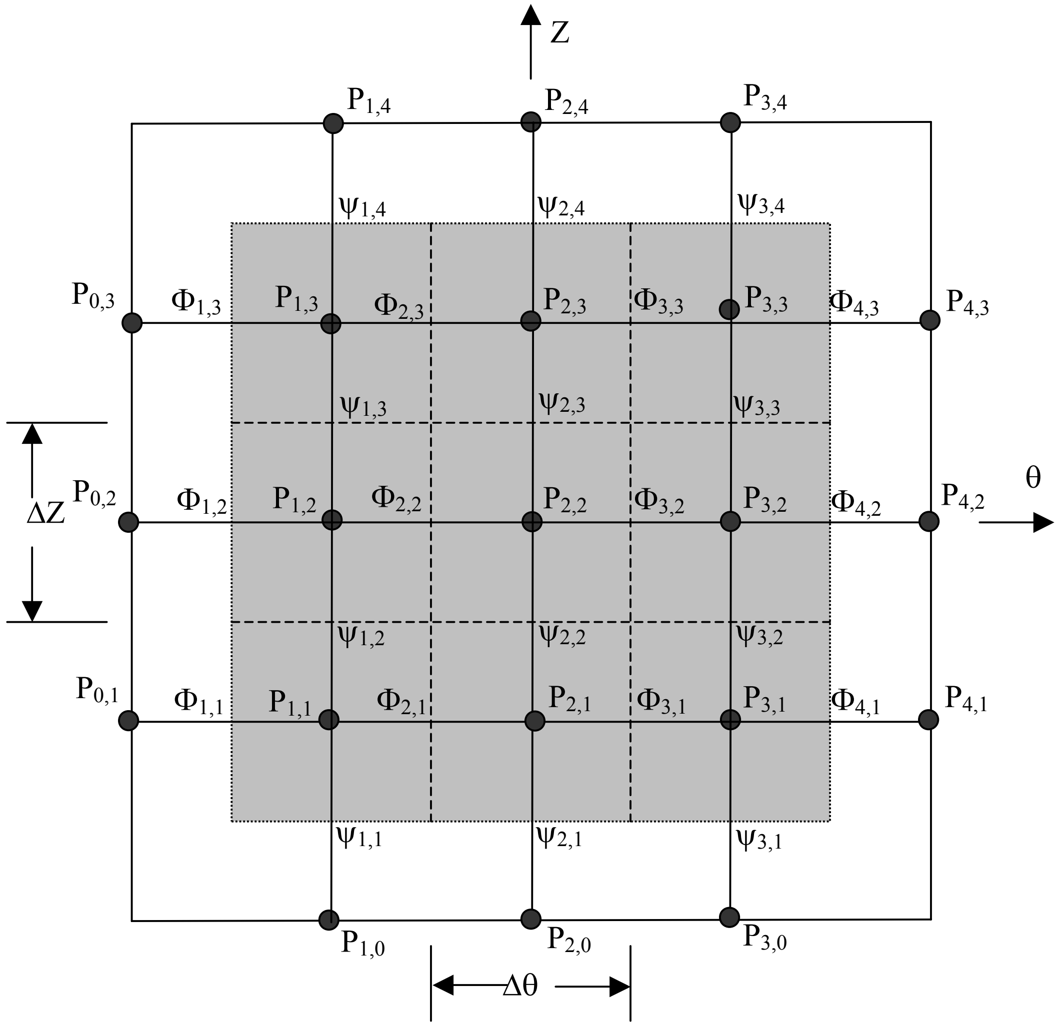

Figure D-2. Grid setup for the 3 x 3 cell case.

The solution involves setting up and solving a system of equations with 33 equations and 33 total unknowns. There are 9 continuity equations for the 9 unknown internal pressures and 24 equations for each of the 24 unknown fluxes (12 each in the circumferential and radial directions). The equations are given in Table D-1.

Table D-1. Thirty-three Independent Equations for the 3 x 3 Cell Case.

9 Equations from Continuity	**12 Equations involving Axial Fluxes**
$-\Phi_{1,1}-\Psi_{1,1}+\Phi_{2,1}+\Psi_{1,2}=0$ $-\Phi_{2,1}-\Psi_{2,1}+\Phi_{3,1}+\Psi_{2,2}=0$ $-\Phi_{3,1}-\Psi_{3,1}+\Phi_{4,1}+\Psi_{3,2}=0$ $-\Phi_{1,2}-\Psi_{1,2}+\Phi_{2,2}+\Psi_{1,3}=0$ $-\Phi_{2,2}-\Psi_{2,2}+\Phi_{3,2}+\Psi_{2,3}=0$ $-\Phi_{3,2}-\Psi_{3,2}+\Phi_{4,2}+\Psi_{3,3}=0$ $-\Phi_{1,3}-\Psi_{1,3}+\Phi_{2,3}+\Psi_{1,4}=0$ $-\Phi_{2,3}-\Psi_{2,3}+\Phi_{3,3}+\Psi_{2,4}=0$ $-\Phi_{3,3}-\Psi_{3,3}+\Phi_{4,3}+\Psi_{3,4}=0$	$\frac{2\Delta Z}{H_1}\Psi_{1,1}+P_{1,1}=P_{1,0}$ $\frac{2\Delta Z}{H_1}\Psi_{1,2}+P_{1,2}-P_{1,1}=0$ $\frac{2\Delta Z}{H_1}\Psi_{1,3}+P_{1,3}-P_{1,2}=0$ $\frac{2\Delta Z}{H_1}\Psi_{1,4}-P_{1,3}=-P_{1,4}$ $\frac{2\Delta Z}{H_2}\Psi_{2,1}+P_{2,1}=P_{2,0}$ $\frac{2\Delta Z}{H_2}\Psi_{2,2}+P_{2,2}-P_{2,1}=0$ $\frac{2\Delta Z}{H_2}\Psi_{2,3}+P_{2,3}-P_{2,2}=0$ $\frac{2\Delta \mathrm{Z}}{\mathrm{H}_1}\Psi_{1,4}-\mathrm{P}_{1,3}=-\mathrm{P}_{1,4}$ $\frac{2\Delta \mathrm{Z}}{\mathrm{H}_2}\Psi_{3,1}+\mathrm{P}_{3,1}=\mathrm{P}_{3,0}$ $\frac{2\Delta \mathrm{Z}}{\mathrm{H}_2}\Psi_{3,2}+\mathrm{P}_{3,2}-\mathrm{P}_{3,1}=0$ $\frac{2\Delta \mathrm{Z}}{\mathrm{H}_2}\Psi_{3,3}+\mathrm{P}_{3,3}-\mathrm{P}_{3,2}=0$ $\frac{2\Delta \mathrm{Z}}{\mathrm{H}_2}\Psi_{3,4}-\mathrm{P}_{3,3}=-\mathrm{P}_{3,4}$
12 Equations involving Circumferential Fluxes	
$J_{3-I}\Phi_{1,1}+P_{1,1}=J_{2-I}+P_{0,1}$ $J_{3-II}\Phi_{2,1}+P_{2,1}-P_{1,1}=J_{2-II}$ $J_{3-III}\Phi_{3,1}+P_{3,1}-P_{2,1}=J_{2-III}$ $J_{3-IV}\Phi_{4,1}-P_{3,1}=J_{2-IV}-P_{4,1}$ $J_{3-I}\Phi_{1,2}+P_{1,2}=J_{2-I}+P_{0,2}$ $J_{3-II}\Phi_{2,2}+P_{2,2}-P_{1,2}=J_{2-II}$ $J_{3-III}\Phi_{3,2}+P_{3,2}-P_{2,2}=J_{2-III}$ $J_{3-IV}\Phi_{4,2}-P_{3,2}=J_{2-IV}-P_{4,2}$ $J_{3-I}\Phi_{1,3}+P_{1,3}=J_{2-I}+P_{0,3}$ $J_{3-II}\Phi_{2,3}+P_{2,3}-P_{1,3}=J_{2-II}$ $J_{3-III}\Phi_{3,3}+P_{3,3}-P_{2,3}=J_{2-III}$ $J_{3-IV}\Phi_{4,3}-P_{3,3}=J_{2-IV}-P_{4,3}$	

The assembly of the matrix involving the mixed set of equations involving unlike terms (pressures and fluxes) makes use of the solution to the 5x5 system of equations for the one cell case represented by (D-21) as a local construction module to assemble the larger global matrix necessary to solve the larger system of equations. This is represented graphically in Figure D-3 for the first row of three pressure cells that results in a 13 x 13 section of the global matrix. For the 3 x 3 case there are three such 13 x 13 sections, since there are three rows. For simplicity, all the cells that are not shown have a value of zero. Cells a_{55}, a_{99} overlap, since equations from two neighboring pressure cells both involve the same unknown that corresponds to a circumferential flux Φ. Care must be given when assembling the multiple rows since there will also be overlap with the common axial fluxes Ψ between two adjacent rows, but the exact location has to be worked out and depends on the number of pressure columns in a row.

$$\left[\begin{array}{ccccccccccccc}
a_{11} & 0 & -1 & 0 & 0 & & & & & & & & \\
0 & a_{22} & -1 & 0 & 0 & & & & & & & & \\
-1 & -1 & 0 & 1 & 1 & & & & & & & & \\
0 & 0 & 1 & a_{44} & 0 & & & & & & & & \\
0 & 0 & 1 & 0 & a_{55} & 0 & -1 & 0 & 0 & & & & \\
 & & & & 0 & a_{66} & -1 & 0 & 0 & & & & \\
 & & & & -1 & -1 & 0 & 1 & 1 & & & & \\
 & & & & 0 & 0 & 1 & a_{88} & 0 & & & & \\
 & & & & 0 & 0 & 1 & 0 & a_{99} & 0 & -1 & 0 & 0 \\
 & & & & & & & & 0 & a_{10,10} & -1 & 0 & 0 \\
 & & & & & & & & -1 & -1 & 0 & 1 & 1 \\
 & & & & & & & & 0 & 0 & 1 & a_{12} & 0 \\
 & & & & & & & & 0 & 0 & 1 & 0 & a_{13,13}
\end{array}\right]
\begin{bmatrix} X_1 \\ X_2 \\ X_3 \\ X_4 \\ X_5 \\ X_6 \\ X_7 \\ X_8 \\ X_9 \\ X_{10} \\ X_{11} \\ X_{12} \\ X_{13} \end{bmatrix}
=
\begin{bmatrix} B_1 \\ B_2 \\ 0 \\ B_4 \\ B_5 \\ B_6 \\ 0 \\ B_8 \\ B_9 \\ B_{10} \\ 0 \\ B_{12} \\ B_{13} \end{bmatrix}$$

Figure D-3. Assembly of the global matrix.

The automated method used in filling in the coefficient matrix [A] and the right hand side vector [B] for a computer generated solution was greatly assisted by first calculating a global variable which keeps track of the center of each 5 x 5 module based on the row and column of each pressure cell. With the global variable, the contribution of neighboring pressures and fluxes can be systematically entered into the global matrix, but the process is too detailed to explain here. Once the matrix [A] and vector [B] are constructed, the solution can be solved for the [X] vector and the pressure and fluxes extracted in the same order they were assembled. Clearly, with the number of zeros in the 3 x 3 case, attempts must be made to reduce the size of the matrix before moving to the M x N case.

D.4 Reducing the Matrix Size

D.4.1 Symmetry Considerations

In regards to symmetry, a first observation that can be made is that the resulting pressure and circumferential fluxes are both symmetric in the axial direction, whereas the axial flux is anti-symmetric. Mathematically, $P(Z) = P(-Z)$, $\Phi(Z) = \Phi(-Z)$ and $\Psi(Z) = -\Psi(-Z)$. Without cavitation, the solution is also symmetric in terms of the circumferential flux and anti-symmetric in regards to the pressure and axial flux. However, once cavitation is considered, the circumferential symmetry will disappear and taking advantage of symmetry in this direction is no longer contemplated.

To take advantage of axial symmetry, if an even number of M cells is taken in the axial direction, the number of rows that has to be considered is only $\frac{M}{2}$. Appropriate boundary conditions are applied along the line of symmetry; namely the axial fluxes Ψ, along the row between the pressure cell at $\frac{M}{2}$ and the ghost cell[4] located on the other side of the line symmetry are set to zero. A second condition is that all the ghost pressures cells on the other side of the line of symmetry are equal to the pressures at $\frac{M}{2}$. With these conditions, the number of equations to solve is thereby reduced.

The extent to which the axial symmetry reduces the size of the matrix can be observed with the following formulas. For an M x N case, the size of the matrix s_A without symmetry considerations is given by

$$s_A = M * N + M * (N + 1) + N * (M + 1) \tag{D-33}$$

where as the reduced size after taking care of symmetry is given by the same formula with M replaced by M/2.

$$s_A = \frac{M}{2} * N + \frac{M}{2} * (N + 1) + N * \left(\frac{M}{2} + 1 \right) \tag{D-34}$$

The significance of the savings for different grid sizes can be seen in looking at the comparing the results of Equations (D-33) and (D-34) for the simple case of a square grid where M = N as summarized in Table D-2. Savings will be even higher with high L/D ratios (shorter bearings) since there will be more grid points in the axial direction.

---

[4] A ghost cell refers to an additional grid point which lies past the presumed boundary and is used to simulate boundary conditions. The grid here is setup so as the ghost cell is placed equidistant and opposite from the boundary as compared to the closest grid point lying within the boundary.

Table D-2. Percent Reduction in Size of Matrix s_A
Using Axial Symmetry.

M = N	s_A without Symmetry	s_A with Axial Symmetry	**Percent Reduction**
4	44	28	**36.4**
8	152	104	**31.6**
12	324	228	**29.6**
16	256	400	**28.6**
32	2144	1568	**26.9**

D.4.2 Converting from a Full Matrix to Banded Matrix

A second approach that was employed to easily reduce the size of the matrix is to set up a banded matrix in place of a square matrix and then call a banded matrix solver subroutine. The simple procedure is stated here, but no attempt is made to explain how it works, since this would require explaining the details of the banded solver subroutine. A simple example of the conversion from a square matrix to a banded matrix is given in Figure D-4.

Square Matrix	Banded Matrix
$\begin{matrix} a_{11} & 2 & 0 & 0 \\ 1 & a_{22} & 4 & 0 \\ 0 & 3 & a_{33} & 0 \\ 0 & 0 & 0 & a_{44} \end{matrix}$	$\begin{matrix} 0 & a_{11} & 2 \\ 1 & a_{22} & 4 \\ 3 & a_{33} & 0 \\ 0 & a_{44} & 0 \end{matrix}$

Figure D-4. Example of conversion from a square matrix to a banded matrix.

The half bandwidth first needs to be determined from observation of the full matrix. The half bandwidth is the longest extent between non-zero entries in any single equation. With the method here, the half bandwidth is proportional to the number of rows (grid points in the circumferential direction). The next step is to calculate the diagonal, which is always the half bandwidth plus unity. The bandwidth is then the half bandwidth plus the diagonal. With this information the banded matrix can be assembled manually. To automate the process there is a simple way to fill the banded matrix based on the indices used to fill the full matrix. In place of A[i][j], the j-index is replaced by a new index, j* allowing to assemble the banded matrix A[i][j*] where

$$j^* = \text{diagonal} + (j - i) \tag{D-34}$$

The results of a quick look at the savings in array size from use of the banded matrix over a square matrix are found in Tables D-3 and D-4. If the same grid spacing is used in the axial and circumferential directions, the percent reduction is higher for increasing L/D. Unlike the reduction with symmetry, which tapers off with increased grid size, the reduction with the banded matrix improves with a finer grid resolution (more grid points).

Table D-3. Percent Reduction with Banded Matrix for Varying L / D.

L/D	Grid Size	Square Matrix Size	Banded Matrix Size	**Percent Reduction**
1	24 x 4	146 x 146	146 x 145	**< 1%**
2	24 x 8	292 x 292	292 x 145	**50%**
3	24 x 16	438 x 438	438 x 145	**67%**
4	24 x 24	584 x 584	584 x 145	**75%**

Table D-4. Percent Reduction with Banded Matrix for Varying Grid Resolution and L/D = 2.

Grid Resolution	Grid Size	Square Matrix Size	Banded Matrix Size	**Percent Reduction**
2	24 x 8	292 x 292	292 x 145	**50%**
3	36 x 12	654 x 654	654 x 217	**67%**
4	48 x 16	1160 x 1160	1160 x 289	**75%**

The two methods of reducing the matrix size complement each other well. The use of axial symmetry reduces the number of columns and the banded matrix reduces the number of rows. Put together, this results in a concatenation method that is easy to program and very practical even with limited RAM of a personal computer.

D.5 Concatenation for the M x N Case

Only some results and a few brief comments are offered here for the M x N Case. Figure D-5 firsts tests the applicability for the method to both long bearing and short bearing arrangements. Figures D-6, D-7 and D-8 give three-dimensional plots the pressures and fluxes for a long bearing setup with a high grid resolution. Figures D-9, D-10 and D-11 give the same results for a short bearing also with a high grid resolution. Figure D-12 gives the pressure plot for a long bearing with a much lower resolution. The lower resolution of 24 x 16 captures the shape of the pressure profile remarkably well.

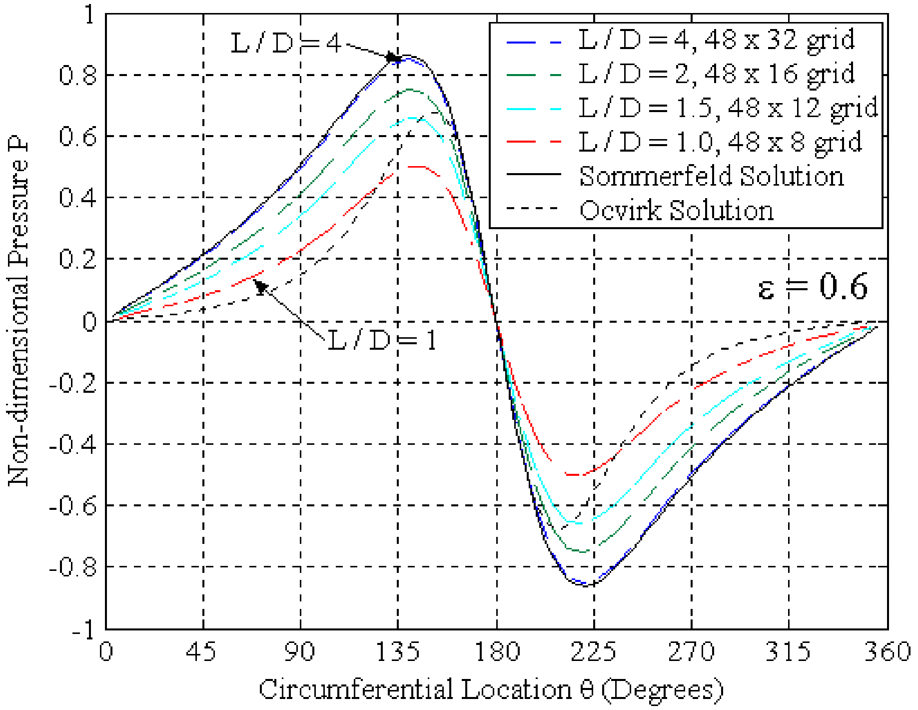

Figure D-5. Centerline comparison to Sommerfeld and Ocvirk solutions.

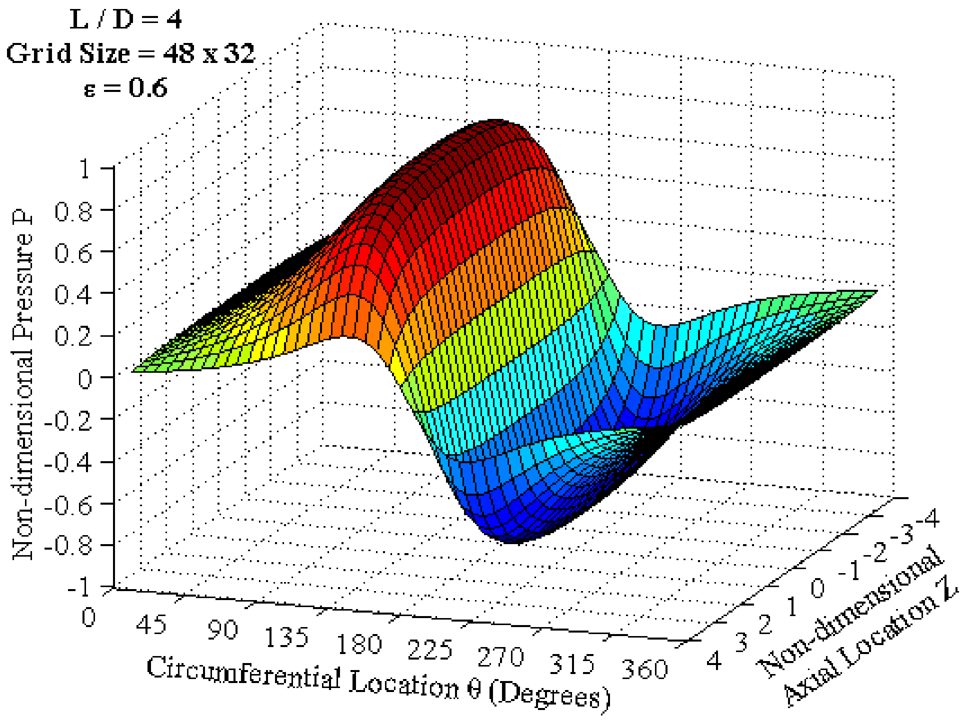

Figure D-6. Concatenated pressure P for long bearing with high grid resolution.

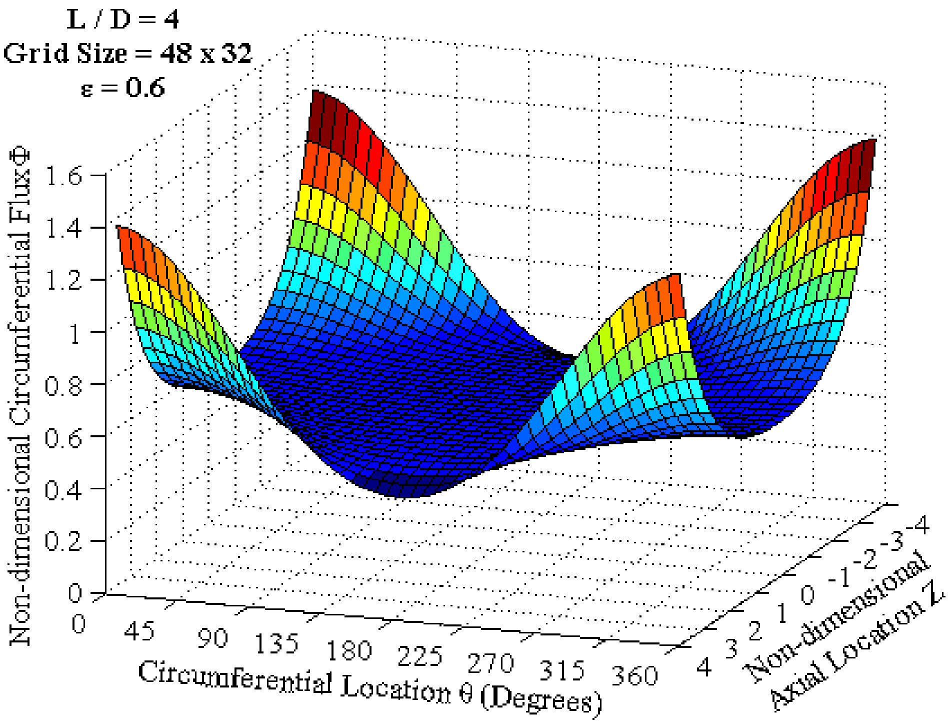

Figure D-7. Concatenated circumferential flux Φ for long bearing with high grid resolution.

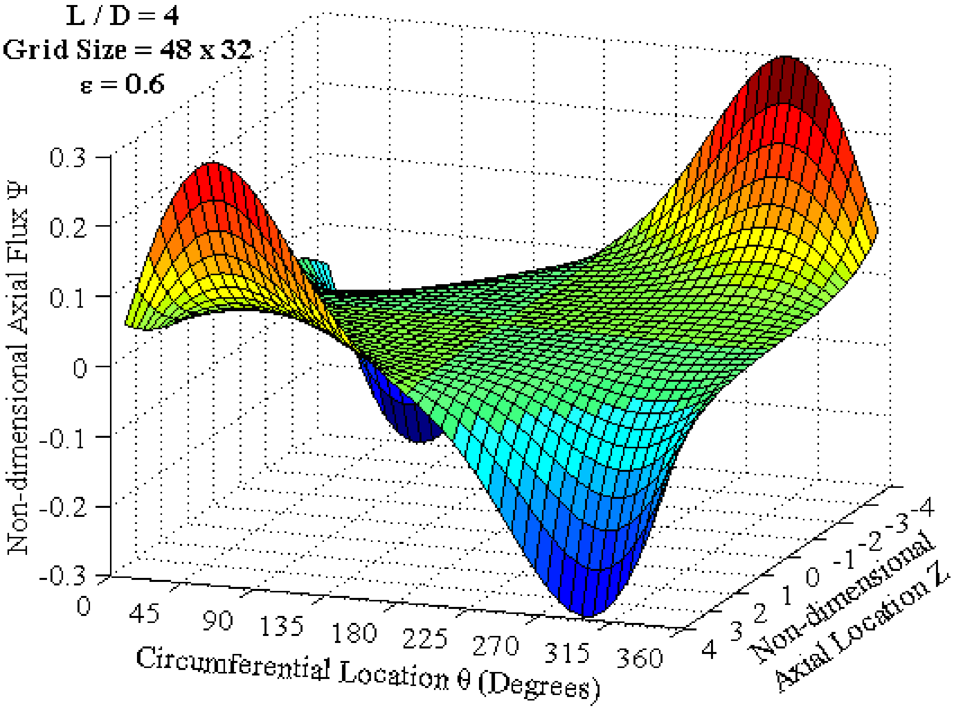

Figure D-8. Concatenated axial flux Ψ for long bearing with high grid resolution.

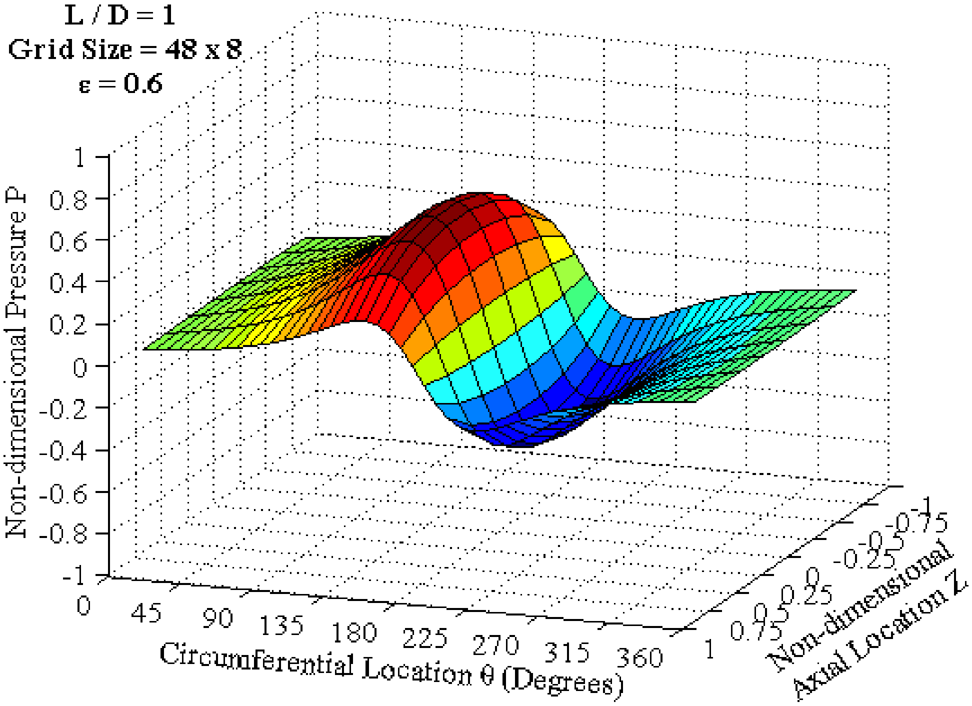

Figure D-9. Concatenated pressure P for short bearing with high grid resolution.

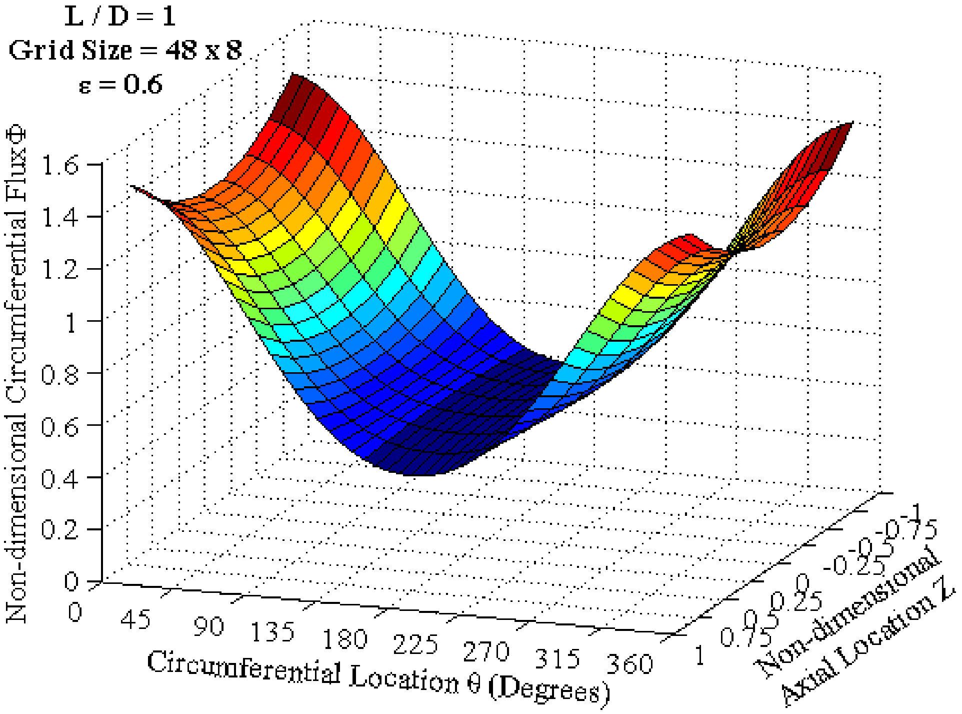

Figure D-10. Concatenated circumferential flux Φ for short bearing with high grid resolution.

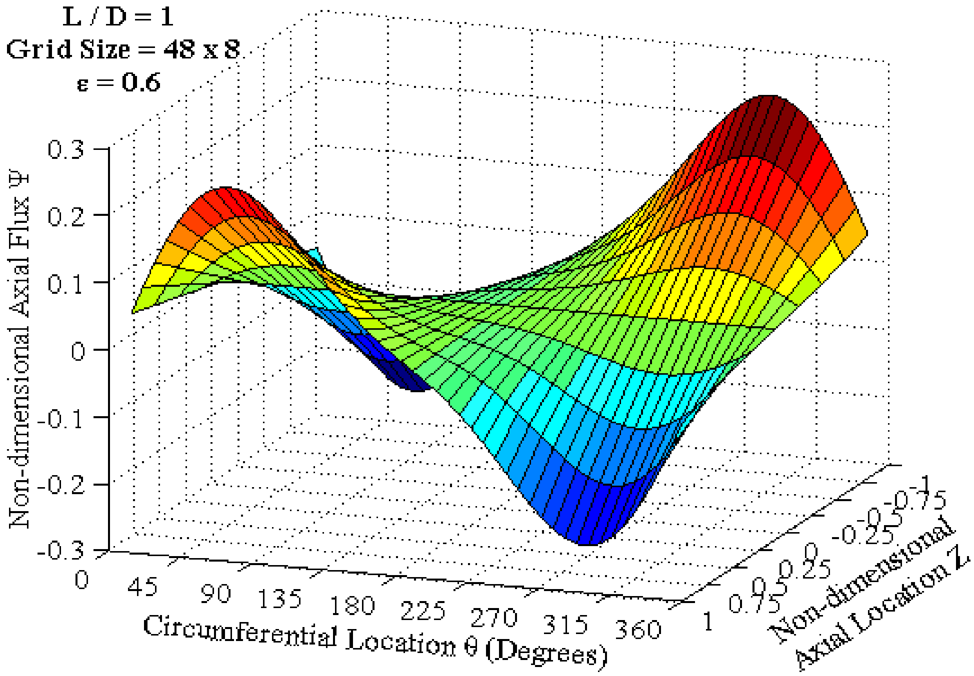

Figure D-11. Concatenated axial flux Ψ for long bearing with high grid resolution.

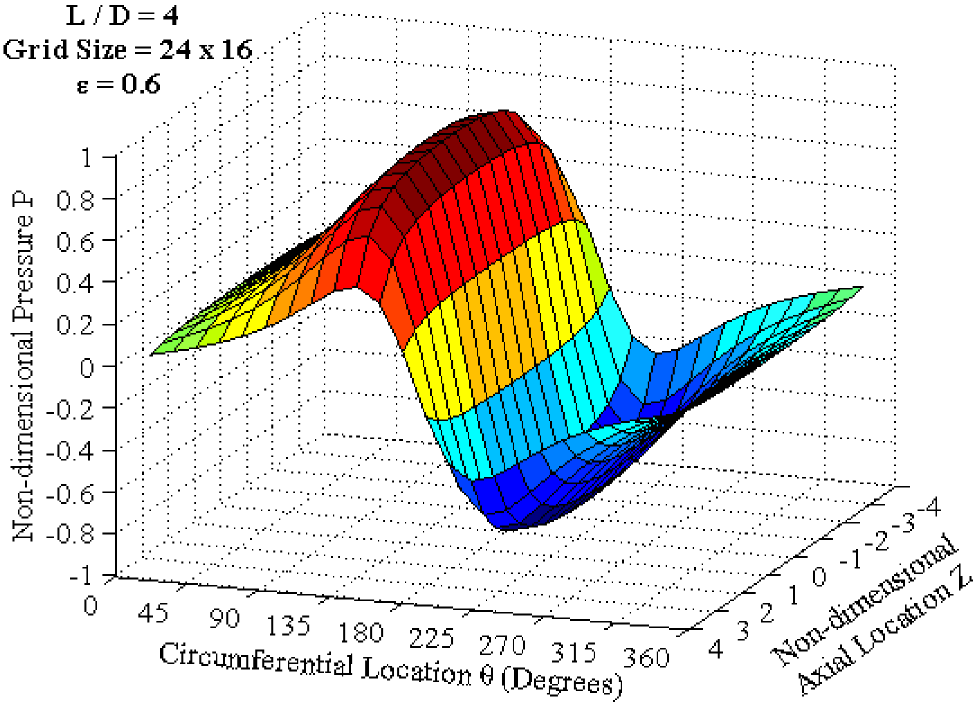

Figure D-12. Concatenated pressure P for long bearing with low resolution.

Appendix E – Matlab Computer Code

E.1 gumbel_chart.m – Generates Gumbel charts for given eccentricity.

E.2 olsson_rupture.m – Generates rupture point movement graphs used in parametric study involving speed, time and location.

E.3 olsson_integrate.m – Produces movie of two-dimensional pressure profile and film thickness plots of rupture movement from 180° to Swift-Stieber and plots makeup flux and bearing performance parameters .

E.4 concat.m – Generates three-dimensional pressure and flux plots of concatenation method without cavitation.

E.5 elrod.m – Produces movie of three-dimensional pressure and film thickness plots for Elrod cavitation algorithm.

Appendix E.1 – gumbel_chart.m

This Matlab v6.5 program creates a Gumbel chart for a given eccentricity which superimposes a contour plot of the non-dimensional flux H0 for arbitrary formation and rupture locations along with starvation incipience and Swift-Stieber lines. Starvation incipience is where film thickness H at rupture equals film thickness at formation below which cavitation occurs just downstream of the formation point. The Swift-Stieber line is where the pressure gradient at rupture is equal to zero. Also displays an attic of the values of the maximum film thickness at the Swift-Stieber line.

```
clc, clear all, close all;

eps = 0.6;  eps_str = strcat('\epsilon = ', num2str(eps));

% Settings for plotting
C = ([0.2 0.4 0.6 0.8 1.0 1.2 1.4 1.6 1.8]);
V = ([-180.0 180.0 -180.0 540.0]);
XT = ([-180:45:180]); YT = ([-180:90:450.0]); V2 =([-180.0 180.0 0.4
0.6]);
XT2 = ([-135:45:135]); YT2 = ([0.4:0.05:0.6]);
C3 = ([0.4:0.02:0.56]); V3 =([-180.0 180.0 170.0 230.0]);
XT3 = ([-180:45:180]); YT3 = ([170.0:10.0:230.0]);
pos_rect1 = [.12 .1 .8 .6]; pos_rect2 = [.12 .7 .8 .2];
pos_rect3 = [.12 .3 .8 .4];
H_max = 1.0 + eps; H_min = 1.0 - eps;
scale = 4; size_A = scale*360;

    % Setup initial arrays for theta location and film thickness
    for i = 1:size_A
        theta(i) = 4.0*pi*(i-1)/(size_A-1) - pi;
        pi_line(i) = pi; sommer_plot(i) = theta(i) + 2.0*pi;
        H(i) = 1.0 + eps * cos(theta(i));
    end;
    H0 = zeros(size_A,size_A);  valid = zeros(size_A,size_A);
    for i = 1:size_A/2
        for j = i+1:i+size_A/2
            dtheta = theta(j) - theta(i);
            y = (1.0 - eps^2.0)^0.5*sin(0.5*dtheta);
            x = cos(0.5*dtheta)+ eps * cos(theta(i)+0.5*dtheta);
            J1 = 2.0 /(1.0-eps^2.0)^0.5 * atan2(y,x);
            J2 = -eps/(1.0-eps^2.0) * (sin(theta(j))/H(j)...
                - sin(theta(i))/H(i)) + 1.0/(1.0-eps^2.0)*J1;
            J3 = -0.5*eps/(1.0-eps^2.0)...
                * (sin(theta(j))/H(j)^2.0 - sin(theta(i))/H(i)^2.0)...
                + 1.5/(1.0-eps^2.0)*J2 - 0.5/(1.0-eps^2.0)*J1;
            H0(i,j) = J2/J3;
            % determine valid points under Gumbel condition
            if H0(i,j) <= H(i) & H0(i,j) >= H(j)
                valid(i,j) = 1;
            end;
        end; % for j
    end; % for i
% Calculate size of Gumbel region
```

```
beg_ss = 0;
for i = 1:size_A/2
    if beg_ss ~= 0
        break;
    end;
    for j = i+1:i+size_A/2
        if valid(i,j) == 1
            beg_ss = i;
            break;
        end;
    end;
end;

% Calculate Swift-Stieber Line
k = 0;
for i = beg_ss:size_A/2
    for j = i+1:i+size_A/2
        if theta(j) >= pi
            part_P = (H(j) - H0(i,j))/H(j)^3;
            if (part_P >= 0.0)
                k = k + 1;
                a = theta(j-1);
                b = theta(j);
                m = (a+b)/2.0;
                ss_th(k) = bisect(a, b, m, theta(i), eps);
                ss_form(k) = theta(i);
                H_attic(k) = H0(i,j);
                break;
            end; % if part_P
        end; % if theta > pi
    end; % for j
end; % for i
end_ss = k;

% calculate Gumbel line where H_form = H0
% close gap

gumb_form(1) = ss_form(1); gumb_th(1) = ss_th(1);
k = 1;
flag = 0;
for i = beg_ss:size_A/2
    k = k + 1;
    if theta(i) >= 0.0
        break;
    end;
    gumb_form(k) = theta(i);
    for j = i+1:i+size_A/2
        if valid(i,j) == 1
            gumb_th(k) = theta(j);
            break;
        end;
    end;
    if gumb_th(k) <= pi & flag == 0
        bord_21 = k; flag = 1;
    end;
end;
```

```
% Plot Results
figure(1);
set(gcf,'DefaultTextFontSize', 12,...
    'DefaultTextFontName', 'Times New Roman');
ax1 = axes('Position', pos_rect1,...
           'XAxisLocation','bottom', 'YAxisLocation', 'right',...
           'FontSize', 12, 'FontName', 'Times New Roman');
axis(ax1,V); set(gca, 'XTick', XT, 'YTick', YT);
ax2 = axes('Position',pos_rect1,...
           'FontSize', 12, 'FontName', 'Times New Roman');
contour(theta*180.0/pi,fliplr(theta*180.0/pi),rot90(H0),C); hold on;
axis(ax2,V); set(gca,'XTick', XT); set(gca,'YTick', YT);
line(gumb_form*180.0/pi,gumb_th*180.0/pi,'Color','b','Parent',ax2);
line(ss_form*180.0/pi,ss_th*180.0/pi,'Color','b','Parent',ax2);
plot(theta*180.0/pi, theta*180.0/pi,'k');
plot(theta*180.0/pi, sommer_plot*180.0/pi,'k');
plot(theta*180.0/pi, pi_line*180.0/pi,'k--');
plot(0,0,'kx'); plot(180,180,'kx');
ylabel('Rupture Point, \theta_r_u_p (Degrees)',...
           'FontSize', 12, 'FontName', 'Times New Roman');
xlabel('Formation Point, \theta_f_o_r_m (Degrees)',...
           'FontSize', 12, 'FontName', 'Times New Roman');
text(-150, 380, eps_str, 'FontSize', 16);
hs = strcat('H_m_a_x = ', num2str(H_max)); text(25,-50,hs);
hs = strcat('H_m_i_n = ', num2str(H_min)); text(50,25,hs);
text(-75,250, 'Swift-Stieber Line');
text(-100,350, 'Sommerfeld Line');
text(-100,50, 'Starvation Incipience Line');
text(100,0, 'Gumbel Region');
text(-10,0, '\theta_f_o_r_m');
ax3 = axes('Position', pos_rect2,...
           'FontSize', 12, 'FontName', 'Times New Roman');
plot(ss_form*180.0/pi, H_attic);
set(gca,'XTick', XT2);
set(gca,'YTick', YT2);
axis(ax3, V2);
ylabel('Swift-Stieber Flux H0',...
           'FontSize', 12, 'FontName', 'Times New Roman');
grid on; hold off;
```

```
figure(2);
set(gcf,'DefaultTextFontSize', 12,...
    'DefaultTextFontName', 'Times New Roman');
ax1 = axes('Position',pos_rect3,...
           'XAxisLocation','bottom',...
           'YAxisLocation','right',...
           'FontSize', 12, 'FontName', 'Times New Roman');
axis(V3); set(gca,'XTick', [], 'YTick', YT3);
ax2 = axes('Position',pos_rect3,...
           'FontSize', 12, 'FontName', 'Times New Roman');
contour(theta*180.0/pi,fliplr(theta*180.0/pi),rot90(H0),C3); hold on;
axis(V3); set(gca, 'XTick', XT3, 'YTick', YT3);
line(gumb_form*180.0/pi, gumb_th*180.0/pi,...
    'LineWidth', 2.0, 'Color', 'b', 'Parent', ax2);
line(ss_form*180.0/pi, ss_th*180.0/pi,...
    'LineWidth', 2.0, 'Color', 'b' ,'Parent', ax2);
line(theta*180.0/pi, pi_line*180.0/pi,...
    'LineStyle', '--', 'LineWidth', 2.0, 'Color', 'b' ,'Parent', ax2);
plot(theta*180.0/pi, theta*180.0/pi,'k');
plot(theta*180.0/pi, sommer_plot*180.0/pi,'k');
text(100, 225, eps_str, 'FontSize', 16);
text(-75, 185, '\theta_f_o_r_m = \pi');
text(-75, 220, 'Swift-Stieber Line'); text(20, 175, 'Gumbel Region');
text(-115, 175, 'Starvation Incipience Line');
ylabel('Rupture Point, \theta_r_u_p (Degrees)',...
           'FontSize', 12, 'FontName', 'Times New Roman');
xlabel('Formation Point, \theta_f_o_r_m (Degrees)',...
           'FontSize', 12, 'FontName', 'Times New Roman');
grid on; hold off;

function m = bisect(a, b, m, th1, eps)

% bisection method
diff = 10.0;
epsilon = 1.0e-13;
while (diff >= epsilon)
    H2 = 1.0 + eps * cos(m); H1 = 1.0 + eps * cos(th1);
    y = (1.0 - eps^2.0)^0.5*sin(0.5*(m-th1));
    x = cos(0.5*(m-th1)) + eps * cos(0.5*(m+th1));
    J1 = 2.0/(1.0-eps^2.0)^0.5*atan2(y,x);
    J2 = -eps/(1.0-eps^2.0)*(sin(m)/H2 - sin(th1)/H1)...
        + 1.0/(1.0-eps^2.0)*J1;
    J3 = -0.5*eps/(1.0-eps^2.0)*(sin(m)/H2^2.0 - sin(th1)/H1^2.0)...
        + 1.5/(1.0-eps^2.0)*J2 - 0.5/(1.0-eps^2.0)*J1;
    HZ = J2/J3;
    part_P = (H2 - HZ)/H2^3;
    diff = abs(part_P);
    if diff <= epsilon;
        break;
    end;
    if (part_P > 0.0)
        b = m;
    else
        a = m;
    end; % if part_P
        m = (a + b)/2.0;
end; % while diff
```

Appendix E.2 olsson_rupture.m

This Matlab v6.5 program calculates various speed, time and location graphs for intermediate Gumbel states starting from an initial starved condition at the minimum gap (180 degrees) until steady-state is reached with a zero pressure gradient at rupture (Swift-Stieber condition). The sequential procedure below is repeated for five different starting formation points as follows:

- Select eccentricity and th_form.
- Calculate Swift-Stieber point th_ss calling bisection subroutine.
- Divide up the region from 180 deg to th_ss into equal number of grid points th_rup.
- For each th_rup, find non-dimensional flux HZ (short for H zero).
- Calculate rupture meniscus speed u_rup and reciprocal u_recip.
- Integrate u_recip using trapezoidal rule to determine time to rupture t_rup at equally spaced spatial increments theta.
- Perform 3rd order polynomial curve fit on th_rup versus log(t_rup)to find th_rup at equally spaced increments of non-dimensional time t.
- Plot results:
    - figure 1 -- meniscus speed versus rupture location
    - figure 2 -- reciprocal of meniscus speed versus rupture location
    - figure 3 -- time versus rupture location
    - figure 4 -- meniscus speed vs. time

```
clc, clear all, close all;
eps = 0.4;

% parameters for labeling axes
V1 = ([180 215 0 0.4]); XT1 = ([180:5:215]); YT1 = ([0:0.05:0.4]);
V2 = ([180 215 0 50]); XT2 = ([180:5:215]); YT2 = ([0:10:50]);
V3 = ([180 215 0 270]); XT3 = ([180:5:215]); YT3 = ([0:45:270]);
V4 = ([0 270 0 0.4]); XT4 = ([0:45:270]); YT4 = ([0:0.05:0.4]);

for k = 1:5
    switch(k)
        case 1, th_form = -40.0; s = 'r--';
        case 2, th_form = -20.0; s = 'r-.';
        case 3, th_form = 0.0; s = 'b-';
        case 4, th_form = 20.0; s = 'k:';
        case 5, th_form = 40.0; s = 'k--';
    end; % switch k

    eps_loc = 0.0;
    eps_str = num2str(eps);
    eps_str = strcat('\epsilon =  ',eps_str);
    th_form = th_form * pi/180.0;
```

```
% calculate theta_ss, swift-stieber location for given th_form
m = 0.0; % middle value for bisection method
th_ss(k) = th_form + 2.0 * pi; % if th_ss not reached
H_form = 1.0 + eps * cos(th_form);
for j = 1:361
    theta(j) = th_form + (j-1) * pi/180.0;
    if (theta(j) > pi)
        H = 1.0 + eps * cos(theta(j));
        y = (1.0-eps^2.0)^0.5*sin(0.5*(theta(j)-th_form));
        x = cos(0.5*(theta(j)-
th_form))+eps*cos(0.5*(theta(j)+th_form));
        J1 = 2.0/(1.0-eps^2.0)^0.5*atan2(y,x);
        J2 = -eps/(1.0-eps^2.0)...
            *(sin(theta(j))/H - sin(th_form)/H_form)...
            + 1.0/(1.0-eps^2.0)*J1;
        J3 = -0.5*eps/(1.0-eps^2.0) * (sin(theta(j))/H^2.0...
            - sin(th_form)/H_form^2.0)...
            + 1.5/(1.0-eps^2.0)*J2 - 0.5/(1.0-eps^2.0)*J1;
        HZ = J2 / J3;
        part_P = (H - HZ)/H^3;
        if (part_P >= 0.0)
            a = theta(j-1);
            b = theta(j);
            m = (a+b)/2.0;
            th_ss(k) = bisect(a, b, m, th_form, eps);
            break;
        end; % if part P >= 0
    end; % if theta > pi
end; % for j
clear theta;

% calculate meniscus rupture speed and reciprocal
scale_men = 100;
n = scale_men - 5;
dth = 180.0/pi*(th_ss(k) - pi)/(scale_men-1);
for i = 1:scale_men+1
    theta(i) = pi + (th_ss(k) - pi) * (i-1) / scale_men;
    H = 1.0 + eps * cos(theta(i));
    y = (1.0-eps^2.0)^0.5*sin(0.5*(theta(i)-th_form));
    x = cos(0.5*(theta(i)-th_form)) + eps *
cos(0.5*(theta(i)+th_form));
    J1 = 2.0/(1.0-eps^2.0)^0.5*atan2(y,x);
    J2 = -eps/(1.0-eps^2.0)...
        *(sin(theta(i))/H - sin(th_form)/H_form)...
        + 1.0/(1.0-eps^2.0)*J1;
    J3 = -0.5*eps/(1.0-eps^2.0) * (sin(theta(i))/H^2.0...
        - sin(th_form)/H_form^2.0)...
        + 1.5/(1.0-eps^2.0)*J2 - 0.5/(1.0-eps^2.0)*J1;
    HZ = J2 / J3;
    u_rup(i) = HZ / H - 1.0;
    u_recip(i) = 1.0/u_rup(i);
end; % for i

    t_men(1) = 0.0; th_men(1) = pi;  u_men(1) = u_rup(1);
    % trapezoidal rule to find time, area under curve
    for i = 2:n
        th_men(i) = pi + (th_ss(k)-pi) * (i-1) / scale_men;
```

```
        t_men(i) = t_men(i-1) + 0.5*(u_recip(i-1)+u_recip(i)) * dth;
    end;

% Simpson's rule
% for i = 3:2:n
%    j = (i+1)/2;
%    th_men(j) = pi + (th_ss(k)-pi) * (i-1) / scale_men;
%     t_men(j) = t_men(j-1) + ...
%        (u_recip(i-2)+4.0*u_recip(i-1)+u_recip(i))*dth/3.0;
%    u_men(j) = u_rup(i);
%end;

tim(k) = t_men((n+1)/2);

figure(1); % meniscus speed versus rupture location
if (k == 1)
    set(gcf, 'DefaultAxesFontName', 'Times New Roman',...
        'DefaultAxesFontSize', 12, 'DefaultTextFontName',...
        'Times New Roman', 'DefaultTextFontSize', 12);
end; % if k = 1
plot(theta*180.0/pi, u_rup, s);
if (k == 1)
    hold on;
    set(gcf, 'DefaultAxesFontName', 'Times New Roman',...
        'DefaultAxesFontSize', 12, 'DefaultTextFontName',...
        'Times New Roman', 'DefaultTextFontSize', 12);
    xlabel('Rupture Location \theta_r_u_p (Degrees)',...
        'FontName', 'Times New Roman', 'FontSize', 12);
    ylabel('Rupture Meniscus Speed U_r_u_p',...
        'FontName', 'Times New Roman', 'FontSize', 12);
    axis(V1);
    text(200, 0.06, eps_str, 'FontSize', 14);
    text(185, 0.03, '\theta_f_o_r_m = 40\circ');
    text(195, 0.05, '\theta_f_o_r_m = -40\circ');
end; % if k = 1
if (k == 5)
    h = legend('\theta_f_o_r_m = -40\circ',...
        '\theta_f_o_r_m = -20\circ', '\theta_f_o_r_m = 0\circ',...
        '\theta_f_o_r_m = 20\circ', '\theta_f_o_r_m = 40\circ', 1);
    set(h, 'FontName', 'Times New Roman', 'FontSize', 10);
    set(gca, 'XTick', XT1);
    set(gca, 'YTick', YT1);
    grid;
    hold off;
end; % if k = 5
```

```
figure(2); % reciprocal of meniscus speed versus rupture location
if (k == 1)
    set(gcf, 'DefaultAxesFontName', 'Times New Roman',...
        'DefaultAxesFontSize', 12, 'DefaultTextFontName',...
        'Times New Roman', 'DefaultTextFontSize', 12);
end; % if k = 1
plot(theta*180.0/pi, u_recip, s);
if (k == 1)
    hold on;
    xlabel('Rupture Location \theta_r_u_p (Degrees)',...
        'FontName', 'Times New Roman', 'FontSize', 12);
    ylabel('Reciprocal of Meniscus Speed U_r_e_c_i_p',...
        'FontName', 'Times New Roman', 'FontSize', 12);
   axis(V2);
   text(185, 520, eps_str, 'FontSize', 14);
   text(200, 220, '\theta_f_o_r_m = 40\circ');
   text(215, 120, '\theta_f_o_r_m = -40\circ');
end; % if k = 1
if (k == 5)
    h = legend('\theta_f_o_r_m = -40\circ',...
        '\theta_f_o_r_m = -20\circ', '\theta_f_o_r_m = 0\circ',...
        '\theta_f_o_r_m = 20\circ', '\theta_f_o_r_m = 40\circ', 0);
    set(h, 'FontName', 'Times New Roman', 'FontSize', 10);
    set(gca, 'XTick', XT2); set(gca, 'YTick', YT2);
    grid;
    hold off;
end; % if k = 5

figure(3); % time versus rupture location
if (k == 1)
    set(gcf, 'DefaultAxesFontName', 'Times New Roman',...
        'DefaultAxesFontSize', 12, 'DefaultTextFontName',...
        'Times New Roman', 'DefaultTextFontSize', 12);
end; % if k = 1
plot(th_men(1:(n+1)/2)*180.0/pi, t_men(1:(n+1)/2), s);
if (k == 1)
    hold on;
    set(gcf, 'DefaultAxesFontName', 'Times New Roman',...
        'DefaultAxesFontSize', 12, 'DefaultTextFontName',...
        'Times New Roman', 'DefaultTextFontSize', 12);
    xlabel('Rupture Location \theta_r_u_p (Degrees)',...
        'FontName', 'Times New Roman', 'FontSize', 12);
    ylabel('Nondimensional Time T',...
        'FontName', 'Times New Roman', 'FontSize', 12);
    axis(V3);
    text(200, 25, eps_str, 'FontSize', 14);
    text(195, 15, '\theta_f_o_r_m = 40\circ');
    text(210, 5, '\theta_f_o_r_m = -40\circ');
end; % if k = 1
if (k == 5)
    h = legend('\theta_f_o_r_m = -40\circ',...
        '\theta_f_o_r_m = -20\circ', '\theta_f_o_r_m = 0\circ',...
        '\theta_f_o_r_m = 20\circ', '\theta_f_o_r_m = 40\circ', 0);
    set(h, 'FontName', 'Times New Roman', 'FontSize', 10);
    set(gca, 'XTick', XT3);  set(gca, 'YTick', YT3);
    grid; hold off;
end; % if k = 5
```

```
figure(4); % meniscus speed vs. time
if (k == 1)
    set(gcf, 'DefaultAxesFontName', 'Times New Roman',...
        'DefaultAxesFontSize', 12, 'DefaultTextFontName',...
        'Times New Roman', 'DefaultTextFontSize', 12);
end; % if k = 1
plot(t_men(1:(n+1)/2), u_men(1:(n+1)/2), s);
if (k == 1)
    hold on;
    set(gcf, 'DefaultAxesFontName', 'Times New Roman',...
        'DefaultAxesFontSize', 12, 'DefaultTextFontName',...
        'Times New Roman', 'DefaultTextFontSize', 12);
    xlabel('Nondimensional Time T',...
        'FontName', 'Times New Roman', 'FontSize', 12);
    ylabel('Nondimesional Meniscus Speed U_r_u_p',...
        'FontName', 'Times New Roman', 'FontSize', 12);
    axis(V4);
    text(0.035, 32, eps_str, 'FontSize', 14);
    text(0.03, 28, '\theta_f_o_r_m = 40\circ');
    text(0.05, 20, '\theta_f_o_r_m = -40\circ');
end; % if k = 1
if (k == 5)
    h = legend('\theta_f_o_r_m = -40\circ',...
        '\theta_f_o_r_m = -20\circ', '\theta_f_o_r_m = 0\circ',...
        '\theta_f_o_r_m = 20\circ', '\theta_f_o_r_m = 40\circ', 0);
    set(h, 'FontName', 'Times New Roman', 'FontSize', 10);
    set(gca, 'XTick', XT4);
    set(gca, 'YTick', YT4);
    grid;
    hold off;
end; % if k = 5

end; % for k
tim th_ss
```

Appendix E.3 olsson_integrate.m

This Matlab v6.5 program produces a movie of the temporal evolution of fluid in a long journal bearing considering cavitation from an initial starved condition at the minimum gap (180 degrees) to the steady-state. Bearing performance parameters of load capacity, attitude angle and friction are calculated.

In addition to tracking the rupture meniscus movement, the program simultaneously advances the adhered film and calculates the makeup flux at the supply groove downstream. The location of the lone supply groove may be anywhere from -180 to 180 degrees and the eccentricity is constant, but arbitrary. The program

- calculates the steady state solution of the full-film region applying the Reynolds equation along with the Swift-Stieber boundary condition using the bisection method.
- determines the meniscus speed and rupture location for the intermediate Gumbel states are found using Olsson's equation at equally spaced spatial intervals between 180 degrees and steady state.
- finds the time to reach each intermediate state by numerically integrating the reciprocal of the rupture meniscus speed using the trapezoidal rule.
- Evaluates the rupture location at equally spaced temporal intervals using Matlab's *polyfit* function allowing the fluid movement to be smoothly marched along in time.

```
clc, clear all, close all;

% prompt user for setup values;
eps = input ('Enter eccentricity (0:0.99)? ');
th_form = input('Enter formation angle (-180:180)? ');
P_max = input('Enter estimate for maximum pressure (0.25:2.0)');
P_min = -0.25;

% prepare labels and sizing for plotting and movies
thf_str = num2str(abs(round(th_form)));
if th_form < 0.0
    thf_str = strcat('_m',thf_str);
else thf_str = strcat('_',thf_str);
end;
eps_str = num2str(round(eps*10.0));

% output file for movie
mov_file = strcat('Gumbel_',eps_str,thf_str)
mov = avifile(mov_file, 'compression', 'Indeo3',...
    'quality', 100, 'fps', 2);
if mod(th_form, 45) == 0
    th_beg = th_form - mod(th_form,45); th_add = 360;
else
    th_beg = th_form - mod(th_form,45)+45; th_add = 315;
end;
th_end = th_form + 360.0; Hm_loc = th_end - 50.0; H_max = 1.0 + eps;
eps_str = num2str(eps); eps_str = strcat('\epsilon =     ', eps_str);
thf_str = num2str(th_form);
thf_str = strcat('\theta_f_o_r_m =     ', thf_str, '\circ');
```

```
eps_hgt = P_max + 0.2; eps_loc = th_form + 120.0;
if th_form == 90
    eps_loc = th_form + 270.0;
end;
thf_hgt = eps_hgt; thf_loc = eps_loc + 90;
% axes scaling and tick marks for plotting
V1 = ([th_form th_end P_min P_max]);
V2 = ([th_form th_end 0.0 H_max]);
V3 = ([0 315 0.0 0.8]);
V4 = ([0 315 0.0 2.0]);
V5 =  ([0 315 -90 90]);
XT = ([th_beg:45:th_beg + th_add]);
YT = ([P_min:0.25:P_max]); YT2 = ([0.0:0.2:H_max]);
XT3 = ([0:45:315]); YT3 = ([0.0:0.2:0.8]); YT4 = ([0.0:0.2:2.0]);
pos_rect1 = [.1  .6  .8  .35];
pos_rect2 = [.1  .1  .8  .35];
pos_rect3 = [.1  .3  .8  .2];

    th_form = (th_form-0.0) * pi/180.0; % convert from degrees to
radians
    % the 0.5 in th_form above is for the supply groove finite width

    % calculate theta_ss, swift-stieber location for given th_form
    m = 0.0; % middle value for bisection method
    th_ss = th_form + 2.0 * pi; % if th_ss not reached
    H_form = 1.0 + eps * cos(th_form);
    for j = 1:361
        theta(j) = th_form + (j-1) * pi/180.0;
        if (theta(j) > pi)
            H = 1.0 + eps * cos(theta(j));
            y = (1.0-eps^2.0)^0.5*sin(0.5*(theta(j)-th_form));
            x = cos(0.5*(theta(j)-
th_form))+eps*cos(0.5*(theta(j)+th_form));
            J1 = 2.0/(1.0-eps^2.0)^0.5*atan2(y,x);
            a2 = -eps/(1.0-eps^2.0)...
                *(sin(theta(j))/H - sin(th_form)/H_form);
            a3 = -0.5*eps/(1.0-eps^2.0) * (sin(theta(j))/H^2.0...
                - sin(th_form)/H_form^2.0);
            J2 = a2 + 1.0/(1.0-eps^2.0)*J1;
            J3 = a3 + 1.5/(1.0-eps^2.0)*J2 - 0.5/(1.0-eps^2.0)*J1;
            HZ = J2/J3;
            part_P = (H - HZ)/H^3.0;
            if (part_P >= 0.0)
                a = theta(j-1);
                b = theta(j);
                m = (a+b)/2.0;
                th_ss = bisect(a, b, m, th_form, eps);
                break;
            end; % if part P >= 0
        end; % if theta > pi
    end; % for j
    clear theta;
```

```
% calculate meniscus rupture speed and reciprocal
scale_men = 100;
n = scale_men - 3;
dth = 180.0/pi * (th_ss - pi)/(scale_men-1);
for i = 1:n+1
    th_men(i) = pi + (th_ss - pi) * (i-1) / scale_men;
    H = 1.0 + eps * cos(th_men(i));
    y = (1.0-eps^2.0)^0.5*sin(0.5*(th_men(i)-th_form));
    x = cos(0.5*(th_men(i)-th_form)) + eps *
cos(0.5*(th_men(i)+th_form));
    J1 = 2.0/(1.0-eps^2.0)^0.5*atan2(y,x);
    J2 = -eps/(1.0-eps^2.0)...
        *(sin(th_men(i))/H - sin(th_form)/H_form)...
        + 1.0/(1.0-eps^2.0)*J1;
    J3 = -0.5*eps/(1.0-eps^2.0) * (sin(th_men(i))/H^2.0...
        - sin(th_form)/H_form^2.0)...
        + 1.5/(1.0-eps^2.0)*J2 - 0.5/(1.0-eps^2.0)*J1;
    HZ = J2/J3;
    u_men(i) = HZ/H - 1.0;
    u_recip(i) = 1.0/u_men(i);
end; % for i
clear th_men;

    t_men(1) = 0.0; th_men(1) = pi;
    % trapezoidal rule to find time, area under curve
    for i = 2:n
        th_men(i) = pi + (th_ss - pi) * (i-1) / scale_men;
        t_men(i) = t_men(i-1) + 0.5 * (u_recip(i-1) + u_recip(i)) *
dth;
    end;

% determine coefficients for 3rd order polynomial curve fit on log
scale
THF = polyfit(log(t_men(2:n)), th_men(2:n), 3);

scale = 4.0; % scale of 4 allows for one grid point every one degree
grid_all = round(scale * 90.0); % grid size
for i = 1:grid_all+1
    theta_plot(i) = (i-1)/grid_all * 2.0 * pi + th_form;
    H_plot(i) = 1.0 + eps * cos(theta_plot(i));
end;

figure(1);
% march in time
active = 0;
hsg = 0.5 * pi/180.0; % supply groove half width, 0.5 deg to radians
t_rup(1) = 0.0;
th_rup(1) = pi;    Hm(1) = 0.0;
for i = 1:n
    deact = 0; active = active + 1;
    Hm(i) = 0.0; delt_Hm = 0.0;

if i >= 2  % skip for 1st iteration; trapezoidal rule needs previous
value

    % calculate rupture time and location
    t_rup(i) = log(t_men(n)*(i-1)/(n-1));
```

```
    th_rup(i) = THF(1)*t_rup(i)^3.0 + THF(2)*t_rup(i)^2.0...
        + THF(3)*t_rup(i) + THF(4);
    t_rup(i) = exp(t_rup(i));
    dth_men = (t_rup(i) - t_rup(i-1))*pi/180.0;
        % update adhered film
        for j = 1:active-1
            adher(j,1) = adher(j,1) + dth_men;
        end;

    % calculate makeup flux as it passes into supply groove
    for j = active-1:-1:2
        if adher(j,1) > (th_form + 2.0*pi-hsg)
            if adher(j-1,1) >= (th_form + 2.0*pi-hsg)
                deact = deact + 1;
                delt_Hm = delt_Hm + 0.5*(adher(j,1)-adher(j-1,1))...
                    *(adher(j,2)+adher(j-1,2));
            else
                ha2_slot = adher(j-1,2)...
                    + (th_form + 2.0*pi-hsg-adher(j-1,1))*...
                    (adher(j,2)-adher(j-1,2))/(adher(j,1)-adher(j-
1,1));
                delt_Hm = delt_Hm + 0.5*(adher(j,1)-(th_form+2.0*pi-
hsg))...
                    *(adher(j,2)+ha2_slot);
                adher(j,1) = th_form + 2.0*pi-hsg;
                adher(j,2) = ha2_slot;
            end; % if adher(j-1)
        end; % if adher(j)
    end; % for j
end; % if i >= 2

    % calculate H0 film thickness at maximum pressure
    H_rup = 1.0 + eps * cos(th_rup(i));
    y = (1.0-eps^2.0)^0.5*sin(0.5*(th_rup(i)-th_form));
    x = cos(0.5*(th_rup(i)-th_form)) +
eps*cos(0.5*(th_rup(i)+th_form));
    J1 = 2.0/(1.0-eps^2.0)^0.5*atan2(y,x);
    J2 = -eps/(1.0-eps^2.0)...
        *(sin(th_rup(i))/H_rup - sin(th_form)/H_form)...
        + 1.0/(1.0-eps^2.0)*J1;
    J3 = -0.5*eps/(1.0-eps^2.0) * (sin(th_rup(i))/H_rup^2.0...
        - sin(th_form)/H_form^2.0)...
        + 1.5/(1.0-eps^2.0)*J2 - 0.5/(1.0-eps^2.0)*J1;
    HZ = J2 / J3;
    Wy = 1.0/eps*(1.0/H_rup - 1.0/H_form...
        -0.5*HZ*(1.0/H_rup^2.0 - 1.0/H_form^2.0));
    Wx = 1.0/eps*((J1-J2)-HZ*(J2-J3));
    W(i) = (Wx^2.0+Wy^2.0)^0.5;
    Phi(i) = atan2(Wx,Wy);
    F(i) = 4.0*J1 - 3.0*J2^2.0/J3;
```

```
% calculate pressure profile
grid_full = round(0.25 * scale * 180.0/pi * (th_rup(i) - th_form));
th_red = th_form;
for j = 1:grid_full+1
    theta(j) = (j-1)/grid_full*(th_rup(i) - th_form) + th_form;
    H = 1.0 + eps * cos(theta(j));
    y = (1.0-eps^2.0)^0.5*sin(0.5*(theta(j)-th_form));
    x = cos(0.5*(theta(j)-th_form)) + eps*cos(0.5*(theta(j)+th_form));
    J1 = 2.0/(1.0-eps^2.0)^0.5*atan2(y,x);
    J2 = -eps/(1.0-eps^2.0)...
        *(sin(theta(j))/H - sin(th_form)/H_form)...
        + 1.0/(1.0-eps^2.0)*J1;
    J3 = -0.5*eps/(1.0-eps^2.0) * (sin(theta(j))/H^2.0...
        - sin(th_form)/H_form^2.0)...
        + 1.5/(1.0-eps^2.0)*J2 - 0.5/(1.0-eps^2.0)*J1;
    P(j) = J2 - HZ * J3;
    if theta(j) < pi/2.0 & P(j) < 0.0
        P(j) = 0.0;
        th_red = theta(j);
    end; % if P
end; % for j (calculate pressure profile)

    if i >= 2
        Hm(i) = HZ - 2.0*delt_Hm/dth_men; % add total makeup
    end; % if i > 2
    adher(active, 2) = H_rup / 2.0;
    adher(active, 1) = th_rup(i);
    % sort in ascending order based on theta
    adher = sortrows(adher,1);
    active = active - deact;

% delete inactive fluxes and prepare adhered film for plotting
clear adh_tmp th_adh H2_adh;
for j = 1:active
    adh_tmp(j,:) = adher(j,:);
    th_adh(j) = adher(j,1);
    H2_adh(j) = adher(j,2);
end;
clear adher;
adher = adh_tmp;
th_adh(active+1) = th_adh(active);
H2_adh(active+1) = 0.0;
th_adh(active+2) = th_adh(1);
H2_adh(active+2) = 0.0;

    % Calculate subambient and full film for plotting
    if th_red ~= th_form
        grid_sub = round(0.25 * scale * 180.0/pi * (th_red - th_form));
        for j = 1:grid_sub+1
            th_sub(j) = (j-1)/grid_sub*(th_red - th_form) + th_form;
            H_sub(j) = 1.0 + eps * cos(th_sub(j));
        end; % for j
        th_sub(grid_sub+2) = th_sub(grid_sub+1); H_sub(grid_sub+2) =
0.0;
        th_sub(grid_sub+3) = th_sub(1); H_sub(grid_sub+3) = 0.0;
    end; % if th_red
```

```
grid_full = round(0.25 * scale * 180.0/pi * (th_rup(i) - th_form));
for j = 1:grid_full+1
    th_full(j) = (j-1)/grid_full*(th_rup(i) - th_form) + th_form;
    H_full(j) = 1.0 + eps * cos(th_full(j));
end;
th_full(grid_full+2) = th_full(grid_full+1); H_full(grid_full+2) = 0.0;
th_full(grid_full+3) = th_full(1); H_full(grid_full+3) = 0.0;

    % 'Times New Roman'
    set(gcf, 'DefaultAxesFontName', 'Helvetica',...
        'DefaultAxesFontSize', 10, 'DefaultTextFontName',...
        'Helvetica', 'DefaultTextFontSize', 10);
    subplot(2,1,1); plot(theta*180.0/pi, P); hold on;
    axis(V1); set(gca, 'XTick', XT, 'YTick', YT);
    text(eps_loc, eps_hgt, eps_str, 'FontSize', 12);
    text(thf_loc, thf_hgt, thf_str, 'FontSize', 12);
    xlabel('Circumferential Location \theta (Degrees)',...
            'FontName', 'Helvetica', 'FontSize', 12);
    ylabel('Non-dimensional Pressure P',...
            'FontName', 'Helvetica', 'FontSize', 12);
    X = [th_rup(i)*180.0/pi (th_form + 2.0*pi)*180.0/pi]; Y = [0.0
0.0];
    line(X,Y);
    grid on; hold off;

        subplot(2,1,2); plot(theta_plot*180.0/pi, H_plot, 'k'); hold
on;
        axis(V2); set(gca, 'XTick', XT, 'YTick', YT2);
        xlabel('Circumferential Location \theta (Degrees)',...
            'FontName', 'Helvetica', 'FontSize', 12);
        ylabel('Film Thickness H, H_a',...
            'FontName', 'Helvetica', 'FontSize', 12);
        if i >= 2
            Hm_str = num2str(Hm(i));
            Hm_str = strcat('H_m = ', Hm_str);
            text(Hm_loc, 1.91, 'Makeup Flux');
            text(Hm_loc, 1.72, Hm_str);
        end;
        if th_red ~= th_form
            fill(th_sub*180.0/pi, H_sub, [1.0 0.0 0.0],...
                'FaceAlpha', 0.5);
        end;
        fill(th_full*180.0/pi, H_full, [0.0 0.5 0.5], 'FaceAlpha',
0.5);
        fill(th_adh*180.0/pi, H2_adh, [0.0 0.0 1.0], 'FaceAlpha', 0.7);
        grid on; hold off;

        if t_rup(i) >= 250
            break;
        end;
    mf = getframe(gcf);
    mov = addframe(mov,mf);
end; % for i (time march)
```

```
    Hm(1) = Hm(2);
    % plot makeup flux as a function of time
    figure(2);
    set(gcf, 'DefaultAxesFontName', 'Helvetica',...
        'DefaultAxesFontSize', 10, 'DefaultTextFontName',...
        'Helvetica', 'DefaultTextFontSize', 12);
    axis(V3); set(gca, 'XTick', XT3, 'YTick', YT3);
    subplot(3,1,2); scatter(t_rup, Hm, '.'); hold on;
    xlabel('Nondimensional Time T',...
        'FontName', 'Helvetica', 'FontSize', 12);
    ylabel('Nondimensional Flux H_m at Supply Groove',...
        'FontName', 'Helvetica', 'FontSize', 12);
    thf_str = num2str(th_form*180.0/pi-0.5);
    thf_str = strcat('\theta_f_o_r_m = ',thf_str,'\circ');
    text(1.0, 0.3, eps_str); text(1.0, 0.2, thf_str);
    grid on; hold off;

% add several copies of last frame to allow time to pause at end
for i = 1:10
    mov = addframe(mov,mf);
end;
mov = close(mov);

    % plot makeup flux as a function of time
    figure(3); polar(Phi, W); hold on;
    % figure(4); plot(t_rup, F);
```

Appendix E.4 concat.m

This program uses the concatenation method to solve the Reynolds equation in 2-D. It calls a banded matrix solver and further reduces computation by taking advantage of symmetry. The program sets all four boundaries to zero pressure and plots the pressure profile and fluxes in both directions. In addition, it compares the centerline pressure to both long (Sommerfeld) and short bearing theory (Ocvirk solution).

```
clc, clear all, close all;

eps = 0.6;
LD = input('Enter L/D ratio 0.5, 1, 2 or 4? ');
scale = input('Enter resolution min 1, 2, 3 or 4 max? ');
n = 12 * scale; % number of pressure cells in theta direction
m = 2 * LD * scale; % number of pressure cells in z direction

% scaling parameters for plotting
V1 = ([-LD LD 0 360 -1.0 1.0]); V2 = ([-LD LD 0 360 0.0 1.6]);
V3 = ([-LD LD 0 360 -0.3 0.3]); V4 = ([0 360 -1.0 1.0]);
XT = ([0:45:360]);  YT1 = ([-LD:LD*0.25:LD]); YT4 = ([-1.0:0.2:1.0]);
ZT1 = ([-1.0:0.2:1.0]);  ZT2 = ([0:0.2:1.6]); ZT3 = ([-0.3:0.1:0.3]);

% variables for setting up solution matrix
half_m = m/2; hbw = n*3; diag = hbw + 1; bw = hbw + diag;
size_A = n*half_m + half_m*(n+1) + n*(half_m);
A = zeros(size_A,bw); p = zeros(n,m);
phi = zeros(n+1,m); psi = zeros(n,m+1);

% right hand side vector initially set to zero
for i = 1:size_A
    B(i) = 0.0;
end; % for i

dtheta = 2.0 * pi/(n+1);
for i = 1:n
    theta(i) = i * dtheta;
    theta_phi(i) = theta(i) - 0.5 * dtheta;
end;
theta_phi(n+1) = theta(i) + 0.5 * dtheta;

dz = 2.0*LD/(m+1);
for j = 1:m
    z(j) = j * dz - LD;
    z_psi(j) = z(j) - 0.5 * dz;
end;
z_psi(m+1) = z(j) + 0.5 * dz;
```

```
% calculate global matrix cell centers
g = 0;
for j = 1:half_m
    for i = 1:n
        g = g + 3;
        if (i == 1)
            g = g + 1;
        end; % if i or j
        if (i == 1) & (j == 1)
            g = g - 2;
        end;
        glob(i,j) = g;
    end; % if i
end; % if j

y = (1.0 - eps^2.0)^0.5*sin(0.5*dtheta);
% fill in global matrix
for j = 1:half_m
    for i = 1:n
        g = glob(i,j);  % global center

        % left flux
        x = cos(-0.5*dtheta)+ eps * cos(theta(i)-0.5*dtheta);
        J1 = 2/(1.0-eps^2.0)^0.5 * atan2(y,x);
        th1 = theta(i) - dtheta; th2 = theta(i);
        H2 = 1.0 + eps * cos(th2);
        H1 = 1.0 + eps * cos(th1);
        J2 = -eps/(1.0-eps^2.0) * (sin(th2)/H2 - sin(th1)/H1)...
            + 1.0/(1.0-eps^2.0)*J1;
        J3 = -0.5*eps/(1.0-eps^2.0)...
            * (sin(th2)/H2^2.0 - sin(th1)/H1^2.0)...
            + 1.5/(1.0-eps^2.0)* J2 - 0.5/(1.0-eps^2.0)*J1;
        A(g-1,diag) = J3; % phi left
        A(g-1,diag+1) = 1.0; % pressure
        B(g-1) = J2; % right hand side
        if (i ~= 1) % only if not on far left
            g_left = glob(i-1,j);
            A(g-1,diag+g_left-g+1) = -1.0;
        end; % if i

        % pressure
        if (j ~= 1)
            g_below = glob(i,j-1);
            A(g,diag+g_below+1-g) = -1.0; % psi below
        end;
        A(g,diag-1) = -1.0; % either phi left or psi below
        A(g,diag+1) = 1.0; % psi above
        A(g,diag+2) = 1.0; % phi right

        % top flux
        H = 1.0 + eps * cos(theta(i));
        A(g+1,diag) = 2 * dz / H^3.0;
        A(g+1,diag-1) = -1.0;
        if (j ~= half_m) % pressure from cell above
            g_above = glob(i,j+1);
            A(g+1,diag+g_above-g-1) = 1.0;
        end;
```

```
        % right flux
        if (i == n)
            x = cos(-0.5*dtheta)+ eps * cos(theta(i)+0.5*dtheta);
            J1 = 2/(1.0-eps^2.0)^0.5 * atan2(y,x);
            th1 = theta(i) - dtheta; th2 = theta(i);
            H2 = 1.0 + eps * cos(th2); H1 = 1.0 + eps * cos(th1);
            J2 = -eps/(1.0-eps^2.0) * (sin(th2)/H2 - sin(th1)/H1)...
                + 1.0/(1.0-eps^2.0)*J1;
            B(g+2) = J2;
            J3 = -0.5*eps/(1.0-eps^2.0)...
                * (sin(th2)/H2^2.0 - sin(th1)/H1^2.0)...
                + 1.5/(1.0-eps^2.0)* J2 - 0.5/(1.0-eps^2.0)*J1;
            A(g+2,diag) = J3;
            A(g+2,diag-2) = -1.0;
        end; % if i
    end; % for i
end; % for j
B = banded_solver(3,A,B,size_A,hbw);

% extract pressure and fluxes from solution
for j = 1:half_m
    for i = 1:n
        g = glob(i,j); % global coord of center of local matrix
        p(i,j+half_m) = B(g);
        p(i,half_m+1-j) = B(g);
        phi(i,j+half_m) = B(g-1);
        phi(i,half_m+1-j) = B(g-1);
        if (j == 1)
            psi(i,half_m+1) = 0.0;
        end; % if j
        psi(i,j+half_m+1) = B(g+1);
        psi(i,half_m+1-j) = -B(g+1);
        if (i == n)
            phi(i+1,j+half_m) = B(g+2);
            phi(i+1,half_m+1-j) = B(g+2);
        end; % if i
    end; % for i
end; % for j

% output A vector to file
a_fid = fopen('a_band_sym.dat', 'w');
for i = 1:size_A
    for j = 1:bw
         fprintf(a_fid, '%5.2f', A(i,j));
    end;
    fprintf(a_fid, '\n');
end;
fclose(a_fid);
```

```
    j = m/2; % centerline comparison
    for i = 1:n
        p_somer(i) = eps*(2.0 + eps*cos(theta(i)))*sin(theta(i))...
           /(2.0 + eps^2.0)/(1.0 + eps*cos(theta(i)))^2.0;
        p_short(i) = (0.25 - z(j) * z(j)) * eps * sin(theta(i))...
            / (1.0 + eps * cos(theta(i)))^3.0;
    end; % for i
    plot(theta*180.0/pi , p_short);

% plot results
theta = theta * 180.0/pi;
theta_phi = theta_phi * 180.0/pi;

figure(1);
set(gcf, 'DefaultAxesFontName', 'Times New Roman',...
        'DefaultAxesFontSize', 12, 'DefaultTextFontName',...
        'Times New Roman', 'DefaultTextFontSize', 12);
surf(z, theta, p); axis(V1);
set(gca, 'XTick', YT1, 'YTick', XT, 'ZTick', ZT1);
view(110,20);
xlabel('Nondimensional Axial Location Z');
ylabel('Circumferential Location \theta (Degrees)');
zlabel('Nondimensional Pressure P');

figure(2);
set(gcf, 'DefaultAxesFontName', 'Times New Roman',...
        'DefaultAxesFontSize', 12, 'DefaultTextFontName',...
        'Times New Roman', 'DefaultTextFontSize', 12);
surf(z, theta_phi, phi); axis(V2);
set(gca, 'XTick', YT1, 'YTick', XT, 'ZTick', ZT2);
view(110,20);
xlabel('Nondimensional Axial Location Z');
ylabel('Circumferential Location\theta (Degrees)');
zlabel('Nondimensional Circumferential Flux \phi');

figure(3);
set(gcf, 'DefaultAxesFontName', 'Times New Roman',...
        'DefaultAxesFontSize', 12, 'DefaultTextFontName',...
        'Times New Roman', 'DefaultTextFontSize', 12);
surf(z_psi, theta, psi); axis(V3);
set(gca, 'XTick', YT1, 'YTick', XT, 'ZTick', ZT3);
view(110,20);
xlabel('Nondimensional Axial Location Z');
ylabel('Circumferential Location\theta (Degrees)');
zlabel('Nondimensional Axial Flux \psi');

figure(4), plot(theta, p(:,m/2), 'k-'); hold on;
set(gcf, 'DefaultAxesFontName', 'Times New Roman',...
        'DefaultAxesFontSize', 12, 'DefaultTextFontName',...
        'Times New Roman', 'DefaultTextFontSize', 12);
axis(V4); set(gca, 'XTick', XT, 'YTick', YT4);
plot(theta, p_somer, 'b--');
plot(theta, p_short, 'g:');
xlabel('Theta', 'FontName', 'Times New Roman', 'FontSize', 12);
ylabel('Centerline Pressure', 'FontName',...
    'Times New Roman', 'FontSize', 12);
grid on; hold off;
```

```
function R = banded_solver(IOPT,BM,R,NEQ,IHALFB)

%     Asymmetric Banded Matrix Equation Solver
%     Doctored to ignore zeros in LU deomposition step
%     Original Fortran code from Prof. John Sullivan WPI
%     IOPT = 1 Triangularizes the banded matrix B
%     IOPT = 2 Solves for right hand side R, solution returned in R
%     IOPT = 3 Performs IOPT = 1 THEN IOPT = 2 before returning

NRS = NEQ - 1; IHBP = IHALFB + 1;
if (IOPT ~= 2)    % Triangularize Matrix using Doolittle Method
      for K = 1:NRS
            PIVOT = BM(K,IHBP); PD = 1./PIVOT; KK = K + 1; KC = IHBP;
            for I = KK:NEQ
                  KC = KC - 1;
                  if (KC <= 0)
                        break;
                  end; % if KC
                  C = -BM(I,KC) * PD;
                  if (C ~= 0.0)
                        BM(I,KC) = C; KI = KC + 1; LIM = KC + IHALFB;
                        for J = KI:LIM
                              JC = IHBP + J-KC; BM(I,J) = BM(I,J)+
C*BM(K,JC);
                        end; % for J
                  end; % if C
            end; % for I
      end; % for K
end; % if IOPT !=2

if (IOPT ~= 1)    % Modify Load Vector R
      NN = NEQ + 1;
      IBAND = 2 * IHALFB + 1;
            for I = 2:NEQ
                  JC = IHBP - I + 1;
            JI = 1;
            if (JC <= 0)
                  JC = 1; JI = I - IHBP + 1;
            end; % for JC
            SUM = 0.0;
            for J = JC:IHALFB
                  SUM = SUM + BM(I,J) * R(JI); JI = JI + 1;
            end; % for J
            R(I) = R(I) + SUM;
      end; % for I

      % Back Solution
      R(NEQ) = R(NEQ) / BM(NEQ,IHBP);
      for IBACK = 2:NEQ
            I = NN - IBACK; JP = I; KR = IHBP + 1;
            MR = min(IBAND, IHALFB + IBACK); SUM = 0.0;
            for J = KR:MR
                  JP = JP + 1; SUM = SUM + BM(I,J) * R(JP);
            end; % for J
            R(I) = (R(I) - SUM) / BM(I,IHBP);
      end; % for IBACK
end; % if IOPT != 1
```

Appendix E.5 elrod.m

This program solves the Reynolds equation applied to a journal bearing using an ADI (alternate direction implicit) block iterative method. Elrod's cavitation algorithm is used to apply a single governing equation for both the full film and partial thickness zones. The rows are solved implicitly and then the columns, using a tri-diagonal matrix solver (Thomas algorithm). A Jacobi iteration method is used to find explicitly the three coefficients of the tri-diagonal matrix. Settings LD = 1, scale = 4, eps = 0.6, dt = 0.00001, beta = 12500

```
clc, clear all, close all;

% set node spacing in x & z
LD = input('Enter L/D ratio 0.5, 1, 2 or 4? ');
scale = input('Enter resolution low 1, 2, 3 or 4 high? ');
dt = input('enter time step? ');
beta = input('enter bulk modulus? ');
nx = 6 * scale; % number of pressure cells in theta direction
nz = round(4 * LD * scale); % number of pressure cells in z direction
eps = 0.6; % eccentricity ratio
p_c = 0.0; % cavitation pressure

% scaling parameters for plotting
V1 = ([0 360 -LD LD 0.0 12.0]); V2 = ([0 360 -LD LD 0.0 1.6]);
XT = ([0:45:360]);  YT = ([-LD:LD*0.5:LD]);
ZT1 = ([0:2:12]); ZT2 = ([0.0:0.2:1.6]);

eps_str = num2str(round(eps*10.0));
LD_str = num2str(LD); s_str = num2str(scale);
mov_file = strcat('eps_0', eps_str,'_', LD_str, 'x', s_str)
mov = avifile(mov_file, 'compression', 'Indeo3',...
    'fps', 1, 'quality', 100); % output file for movie

% entire grid has two ghost cells on left and one ghost cell outside
% elsewhere
th = zeros(nx+3, nz+2);  z = zeros(nx+3, nz+2);
p = zeros(nx+3, nz+2);  press = p;
TH_mid = ones(nx+3, nz+2); TH_prev = ones(nx+3, nz+2);
g = ones(nx+3, nz+2);

% calculate film thickness (including edges)
    dth = 2.0*pi/(nx+1); % circumferential grid spacing
    dz = 2.0*LD/(nz+1); % axial grid spacing
    L_D = dz/dth; % ratio of length to diameter
    for j = 1:nz+2
        for i = 1:nx+3
            th(i,j) = dth * (i-2);
            z(i,j) = dz * (j-1) - LD;
            H(i,j) = 1.0 + eps * cos(th(i,j));
        end;
    end;
```

```
    % for plotting Ha only
    for j = 2:nz+1
        for i = 3:nx+2
            theta(i-2,j-1) = dth * (i-2);
            zed(i-2,j-1) = dz * (j-1) - LD;
            Ha(i-2,j-1) = 1.0 + eps * cos(theta(i-2,j-1));
        end;
    end;

    % fill interior of matrix with guesses
    for j = 2:nz+1
        for i = 3:nx+2
            if i <= (nx/2 + 2)
                p(i,j) = 20.0;
                TH_mid(i,j) = exp(p(i,j)/(g(i,j)*beta));
                p(i,j) = 25.0;
                TH_prev(i,j) = exp(p(i,j)/(g(i,j)*beta));
            else
                g(i,j) = 0.0;
                TH_mid(i,j) = 0.1;
                TH_prev(i,j) = 0.1;
            end; % if i
        end; % for i
    end; % for j

% iteration parameters
figure(1);
omega = 0.1;   t = 0.0;   rho = 1.5;
count = 0;  delt_n_prev = 0.1;
k = 1; % starting point for solver

% solve for nect value of TH with block iterative method
while (-log(delt_n_prev) < 4) % until error is small
    t = t + dt; % update counters
    count = count + 1;
    delt_n = 0.0;
    clear b0 rhs;   % reset tri-diagonal coefficients
    b0 = zeros(1,nx);
    rhs = zeros(1,nx);

% solve for rows explicitly
for j = 2:nz+1
    for i = 3:nx+2
        a1 = dt/(H(i,j)*8.0*pi*dth);
        a2 = beta*dt/(H(i,j)*48.0*pi^2.0*dth^2.0);
        a3 = beta*dt/(H(i,j)*48.0*L_D^2.0*dz^2.0);
        b2(i-2) = a1*(2.0-0.5*(g(i,j)+g(i-1,j)))*H(i-1,j)...
            + a2*(0.5*(H(i,j)+H(i-1,j)))^3.0*g(i-1,j);
        b0(i-2) = omega + a1*(2.0-0.5*(g(i,j)+g(i+1,j)))...
            -0.5*(g(i,j)+g(i-
1,j))*H(i,j)+a2*((0.5*(H(i,j)+H(i+1,j)))^3.0...
            +(0.5*(H(i,j)+H(i-1,j)))^3.0)*g(i,j)...
            +a3*((0.5*(H(i,j)+H(i,j+1)))^3.0...
            +0.5*(H(i,j)+H(i,j-1)))^3.0)*g(i,j);
        b1(i-2) = a1*0.5*(g(i,j)+g(i+1,j))*H(i+1,j)...
            - a2*(0.5*(H(i,j)+H(i+1,j)))^3.0*g(i+1,j);
        b5_exp = a3*(0.5*(H(i,j)+H(i,j-1)))^3.0*g(i,j-1);
```

```
        b4_exp = a3*(0.5*(H(i,j)+H(i,j+1)))^3.0*g(i,j+1);
        b0_exp = - a1*(1.0-0.5*(g(i,j)+g(i+1,j)))*H(i,j);
        b2_exp = a1*(2.0-0.5*(g(i,j)+g(i+1,j))...
            -0.5*(g(i,j)+g(i-1,j)))*H(i-1,j);
        b3_exp = a1*(1.0-0.5*(g(i,j)+g(i-1,j)))*H(i-2,j);

    rhs_const = - a2*( (0.5*(H(i,j)+H(i+1,j)))^3.0*g(i+1,j)...
        - ((0.5*(H(i,j)+H(i+1,j)))^3.0+(0.5*(H(i,j)+H(i-
1,j)))^3.0)*g(i,j)...
        + (0.5*(H(i,j)+H(i-1,j)))^3.0*g(i-1,j) )...
        - a3*( (0.5*(H(i,j)+H(i,j+1)))^3.0*g(i,j+1)...
        - ((0.5*(H(i,j)+H(i,j+1)))^3.0+(0.5*(H(i,j)+H(i,j-
1)))^3.0)*g(i,j)...
        + (0.5*(H(i,j)+H(i,j-1)))^3.0*g(i,j-1) );

        % update rhs explicitly
        rhs(i-2) = rhs_const + (omega + b0_exp)* TH_prev(i,j)...
            + b2_exp*TH_prev(i-1,j) + b3_exp*TH_prev(i-2,j)...
            + b5_exp*TH_prev(i,j-1) + b4_exp*TH_prev(i,j+1);
    end; % for i

    % apply boundary conditions
    rhs(1) = rhs(1) - b2(1) * TH_prev(2,j);

    % call tri-diagonal solver
    thomas(b2, b0, b1, rhs, k, nx);

    % replace row with solution
    for i = 3:nx+2
        TH_mid(i,j) = rhs(i-2);
    end; % for i
end; % for j

% reset tri-diagonal coefficients
clear b0 rhs;
b0 = zeros(1,nz);
rhs = zeros(1,nz);

% solve for columns explicitly
for i = 3:nx+2
    for j = 2:nz+1
        a1 = dt/(H(i,j)*8.0*pi*dth);
        a2 = beta*dt/(H(i,j)*48.0*pi^2.0*dth^2.0);
        a3 = beta*dt/(H(i,j)*48.0*L_D^2.0*dz^2.0);

        b5(j-1) = -a3*(0.5*(H(i,j)+H(i,j-1)))^3.0*g(i,j-1);
        b0(j-1) = omega + a1*(2.0-0.5*(g(i,j)+g(i+1,j)))...
            -0.5*(g(i,j)+g(i-1,j))*H(i,j)...
            +a2*((0.5*(H(i,j)+H(i+1,j)))^3.0...
            +(0.5*(H(i,j)+H(i-1,j)))^3.0)*g(i,j)...
            +a3*((0.5*(H(i,j)+H(i,j+1)))^3.0...
            +(0.5*(H(i,j)+H(i,j-1)))^3.0)*g(i,j);
        b4(j-1) = -a3*(0.5*(H(i,j)+H(i,j+1)))^3.0*g(i,j+1);
        b3_exp = -a1*(1.0-0.5*(g(i,j)+g(i-1,j)))*H(i-2,j);
        b2_exp = -a1*(2.0-0.5*(g(i,j)+g(i-1,j)))*H(i-1,j)...
            + a2*(2.0-0.5*(g(i,j)+g(i+1,j))...
            -0.5*(g(i,j)+g(i-1,j)))*H(i-1,j)...
```

```
            + a3*(0.5*(H(i,j)+H(i-1,j)))^3.0*g(i-1,j);
        b0_exp = -a1*(1.0-0.5*(g(i,j)+g(i+1,j)))*H(i,j);
        b1_exp = -a1*(0.5*(g(i,j)+g(i+1,j)))*H(i+1,j)...
            - a2*(0.5*(H(i,j)+H(i+1,j)))^3.0*g(i+1,j);

    rhs_const = - a2*( (0.5*(H(i,j)+H(i+1,j)))^3.0*g(i+1,j)...
        - ((0.5*(H(i,j)+H(i+1,j)))^3.0+(0.5*(H(i,j)+H(i-
1,j)))^3.0)*g(i,j)...
        + (0.5*(H(i,j)+H(i-1,j)))^3.0*g(i-1,j) )...
        - a3*( (0.5*(H(i,j)+H(i,j+1)))^3.0*g(i,j+1)...
        - ((0.5*(H(i,j)+H(i,j+1)))^3.0+(0.5*(H(i,j)+H(i,j-
1)))^3.0)*g(i,j)...
        + (0.5*(H(i,j)+H(i,j-1)))^3.0*g(i,j-1) );

        % update rhs explicitly
        rhs(j-1) = b3_exp*TH_mid(i-2,j) + b2_exp*TH_mid(i-1,j)...
            + (omega + b0_exp) * TH_mid(i,j) + b1_exp*TH_mid(i+1,j)...
            + rhs_const;
    end; % for j

    % apply boundary conditions
    rhs(1) = rhs(1) - b5(1) * TH_mid(i, 1);
    rhs(nz) = rhs(nz) - b4(nz) * TH_mid(i, nz+2);

    % call tri-diagonal solver
    thomas(b5, b0, b4, rhs, k, nz);

    % replace column with solution for next iteration and calculate
error
    for j = 2:nz+1
        delt_n = delt_n + abs(rhs(j-1) - TH_prev(i,j));
        TH_prev(i,j) = rhs(j-1);
    end; % for j
end; % for i

% reset switch function
for j = 2:nz+1
    for i = 3:nx+2
        if TH_prev(i,j) >= 1.0
            g(i,j) = 1.0;
        else
            g(i,j) = 0.0;
        end; % reset switch
    end;
end;

    % calculate spectral radius for convergence test
    rho = delt_n / delt_n_prev;
    delt_n_prev = delt_n;

if count > 5 % skip plot of initial conditions
    % calculate pressure & plot results
    for i = 3:nx+2
        for j = 2:nz+1
            if g(i,j) < 1
                Ha(i-2,j-1) = TH_prev(i,j)*H(i,j);
                press(i-1,j) = p_c + 0.0;
```

```
            else
                Ha(i-2,j-1) = H(i,j);
                press(i-1,j) = p_c + g(i,j) * log(TH_prev(i,j));
            end; % if g
        end; % end for j
    end; % end for i

    subplot(2,1,1);
    surf(th*180.0/pi, z, press);
    axis(V1); set(gca,'XTick', XT, 'YTick', YT, 'ZTick', ZT1);
    view(25.0, 25.0);
%    xlabel('Circumferential Location \theta (Degrees)',...
%       'FontSize', 12, 'FontName', 'New Times Roman');
%    ylabel('Non-Dimensional Axial Location Z',...
%       'FontSize', 12, 'FontName', 'New Times Roman');
    subplot(2,1,2);
    surf(theta*180.0/pi, zed, Ha);
    axis(V2); set(gca,'XTick', XT, 'YTick', YT, 'ZTick', ZT2);
    view(25.0, 25.0);
    mf = getframe(gcf);
    mov = addframe(mov,mf);
end; % if count > 5
 if count > 72
     break;
 end;

end; % while delt_n_prev

% add several copies of last frame to allow time to pause at end
for i = 1:10
    mov = addframe(mov,mf);
end;
mov = close(mov);
clc; count, t

%     program thomas.m
%     Tri-diagonal matrix solver
%     F (first) has been added so that
%     one can begin at any starting number (usually 0 or 1)
%     original code in Fortran from Prof. John Sullivan WPI

function R = thomas(A,B,C,R,F,N);

iend = F + N - 1;
C(F) = C(F)/B(F);
R(F) = R(F)/B(F);
for i = (F+1):iend
      im = i-1;
      C(i) = C(i)/(B(i)-A(i)*C(im));
      R(i) = (R(i)-A(i)*R(im))/(B(i)-A(i)*C(im));
end; % for i
for j = (iend - 1):-1:F
      jp = j+1;
      R(j) = R(j) - C(j)*R(jp);
end; % for j
```

Appendix F – Powerpoint Presentation Slides from Thesis Defense

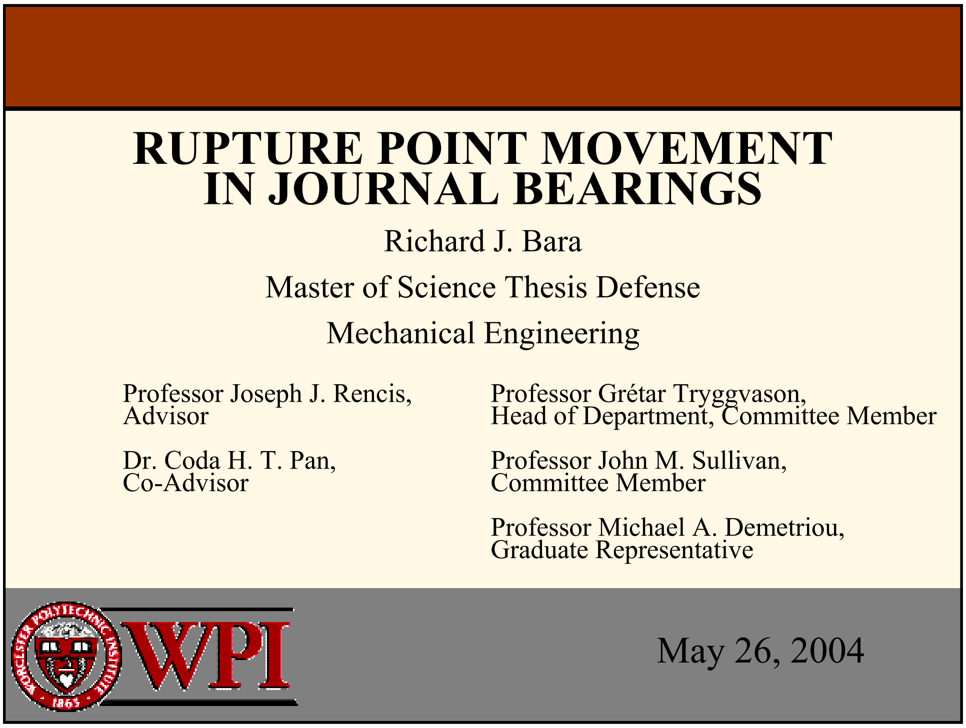

RUPTURE POINT MOVEMENT IN JOURNAL BEARINGS

Richard J. Bara

Master of Science Thesis Defense

Mechanical Engineering

Professor Joseph J. Rencis,
Advisor

Dr. Coda H. T. Pan,
Co-Advisor

Professor Grétar Tryggvason,
Head of Department, Committee Member

Professor John M. Sullivan,
Committee Member

Professor Michael A. Demetriou,
Graduate Representative

May 26, 2004

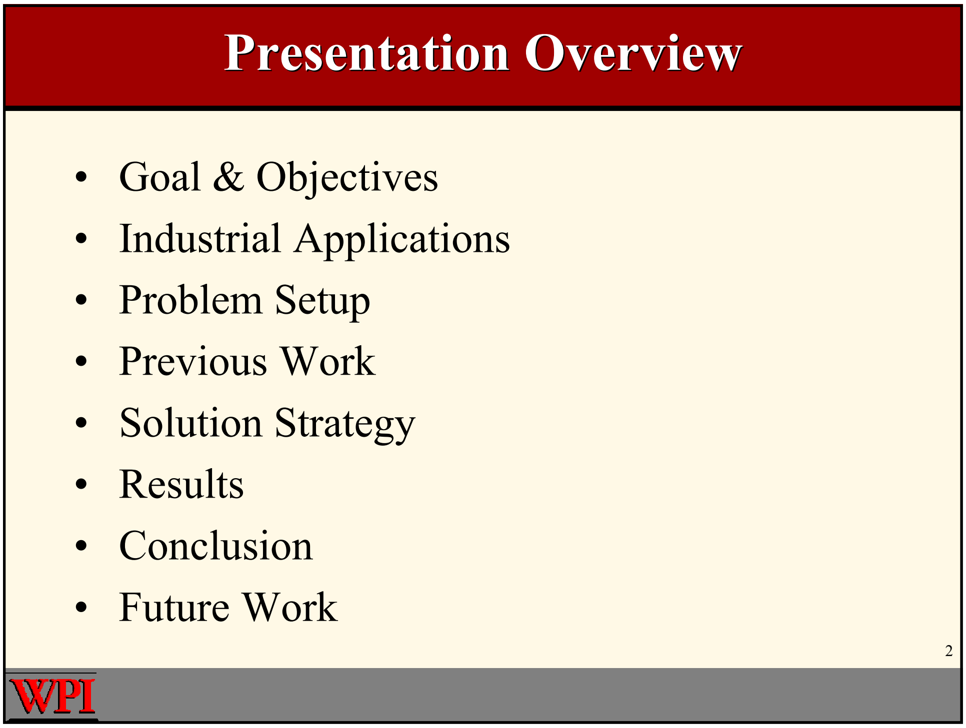

Presentation Overview

- Goal & Objectives
- Industrial Applications
- Problem Setup
- Previous Work
- Solution Strategy
- Results
- Conclusion
- Future Work

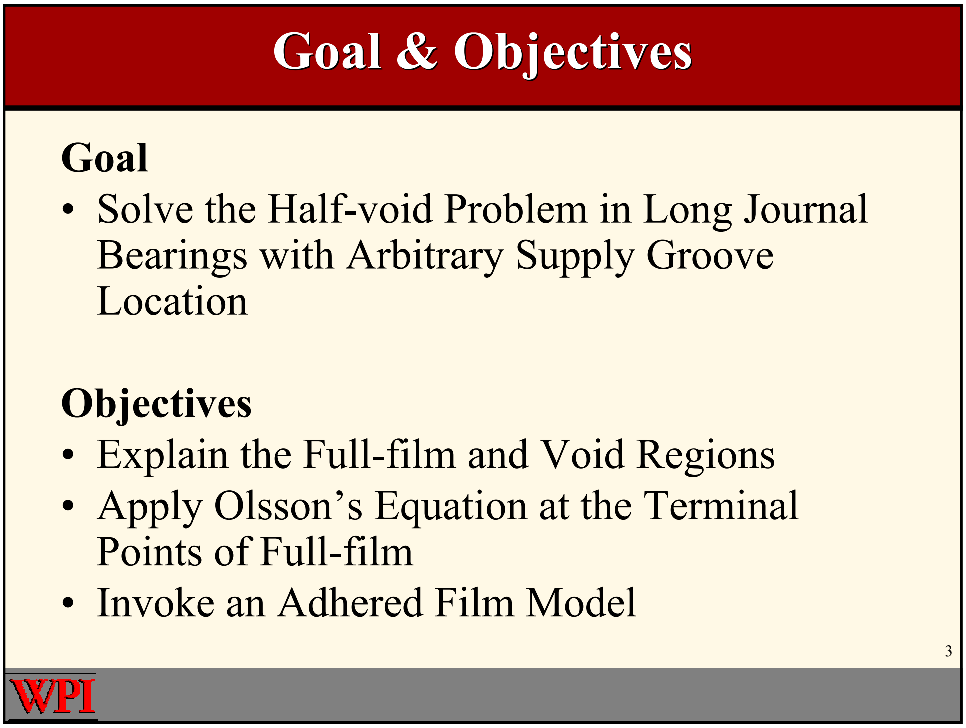

Goal & Objectives

Goal

- Solve the Half-void Problem in Long Journal Bearings with Arbitrary Supply Groove Location

Objectives

- Explain the Full-film and Void Regions
- Apply Olsson's Equation at the Terminal Points of Full-film
- Invoke an Adhered Film Model

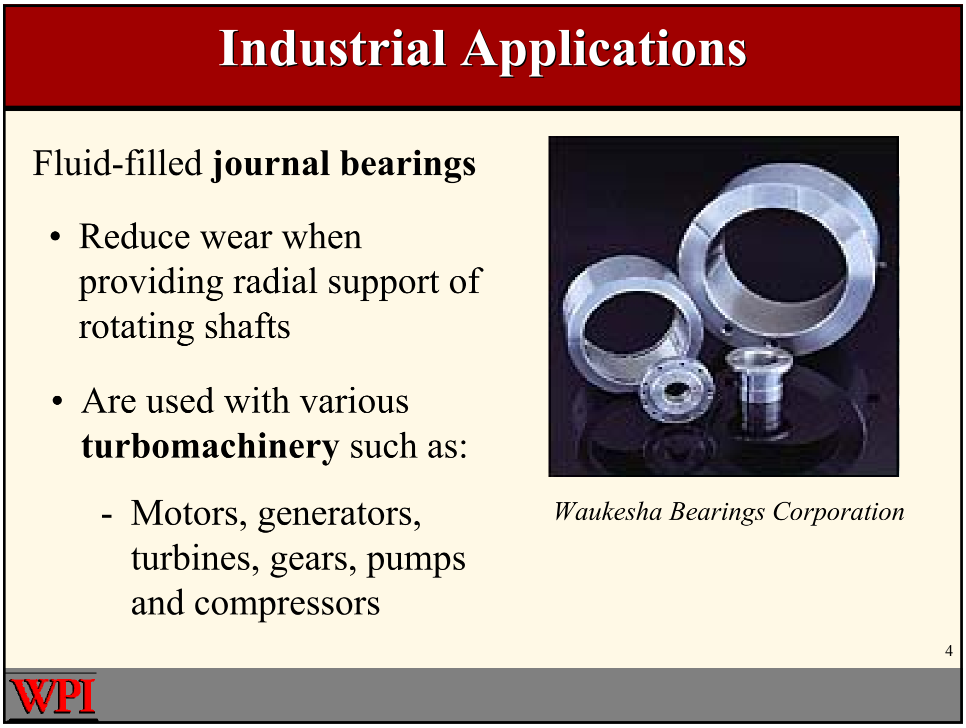

Industrial Applications

Fluid-filled **journal bearings**

- Reduce wear when providing radial support of rotating shafts
- Are used with various **turbomachinery** such as:
  - Motors, generators, turbines, gears, pumps and compressors

Waukesha Bearings Corporation

Industrial Applications -
Numerical Analysis State of Practice

Elrod Cavitation Algorithm

- Finite Difference Approach
- Single Governing Equation Based on Reynolds Equation for both Full-film **and** Void Regions
- 30 years of Development by Numerous Authors
- Fluid Component of Complete Bearing Analysis along with
  - Rotor structural analysis
  - Heat transfer analysis
- **Rupture Point Location Only Approximated**
- **High Grid Density Required**

Disadvantages

WPI

Problem Setup - Long Journal Bearing

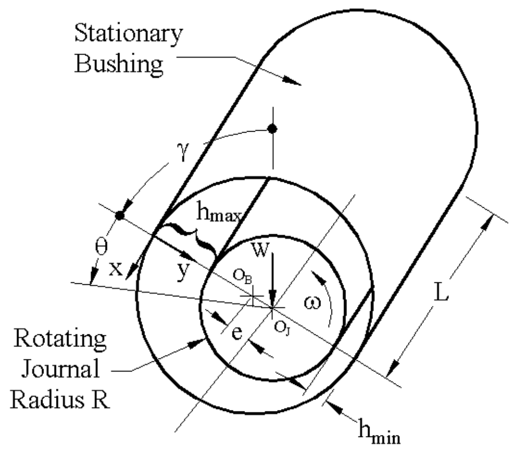

θ - Circumferential Direction

ω - Angular Speed

e - Eccentricity

h - Film Thickness

O_B - Bushing Center

O_J - Journal Center

$$\frac{L}{D} \geq 2$$

WPI

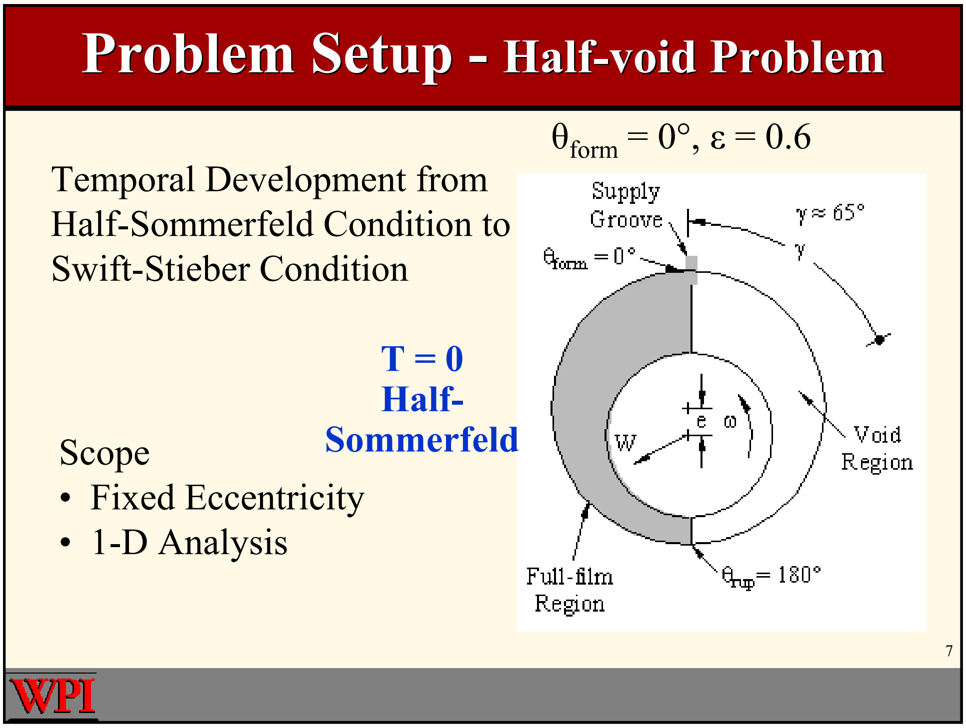

Problem Setup - Half-void Problem

$\theta_{form} = 0°, \varepsilon = 0.6$

Temporal Development from Half-Sommerfeld Condition to Swift-Stieber Condition

T = 0
Half-Sommerfeld

Scope
- Fixed Eccentricity
- 1-D Analysis

7

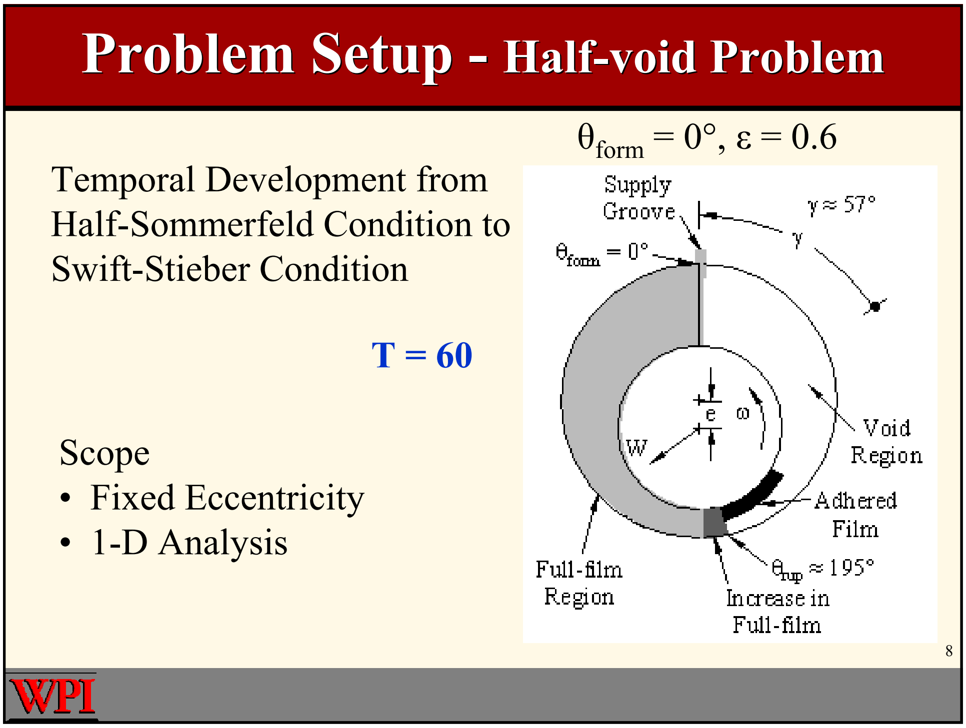

Problem Setup - Half-void Problem

$\theta_{form} = 0°, \varepsilon = 0.6$

Temporal Development from Half-Sommerfeld Condition to Swift-Stieber Condition

T = 60

Scope
- Fixed Eccentricity
- 1-D Analysis

8

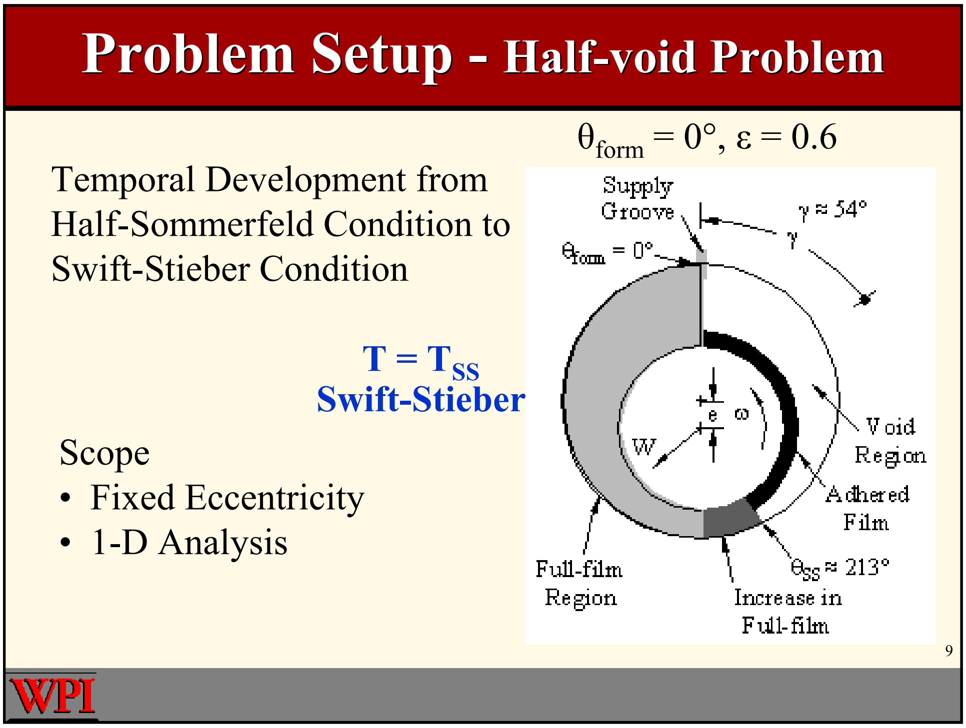

Problem Setup - Half-void Problem

Temporal Development from Half-Sommerfeld Condition to Swift-Stieber Condition

$T = T_{SS}$
Swift-Stieber

Scope

- Fixed Eccentricity
- 1-D Analysis

$\theta_{form} = 0°$, $\varepsilon = 0.6$

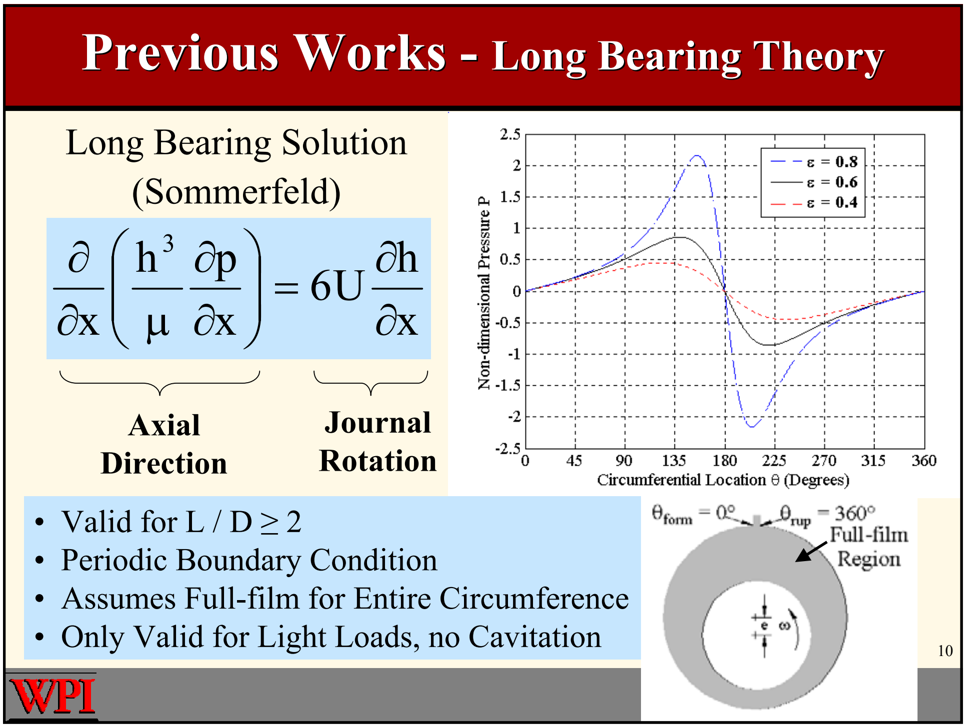

Previous Works - Long Bearing Theory

Long Bearing Solution (Sommerfeld)

$$\underbrace{\frac{\partial}{\partial x}\left(\frac{h^3}{\mu}\frac{\partial p}{\partial x}\right)}_{\textbf{Axial Direction}} = \underbrace{6U\frac{\partial h}{\partial x}}_{\textbf{Journal Rotation}}$$

- Valid for L / D ≥ 2
- Periodic Boundary Condition
- Assumes Full-film for Entire Circumference
- Only Valid for Light Loads, no Cavitation

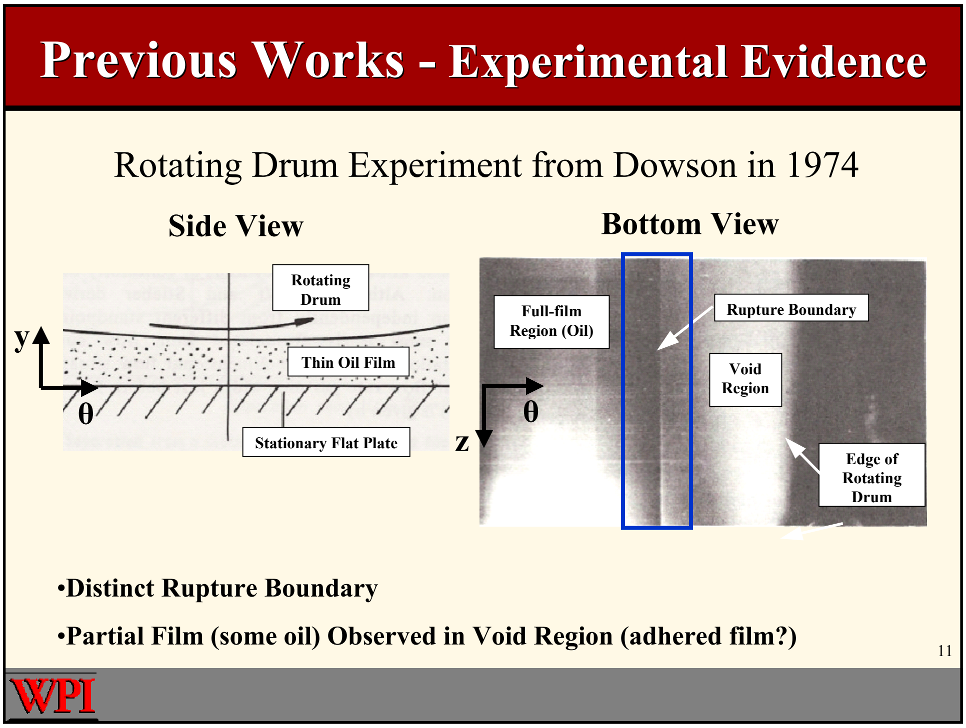

Previous Works - Experimental Evidence

Rotating Drum Experiment from Dowson in 1974

Side View

Bottom View

- **Distinct Rupture Boundary**
- **Partial Film (some oil) Observed in Void Region (adhered film?)**

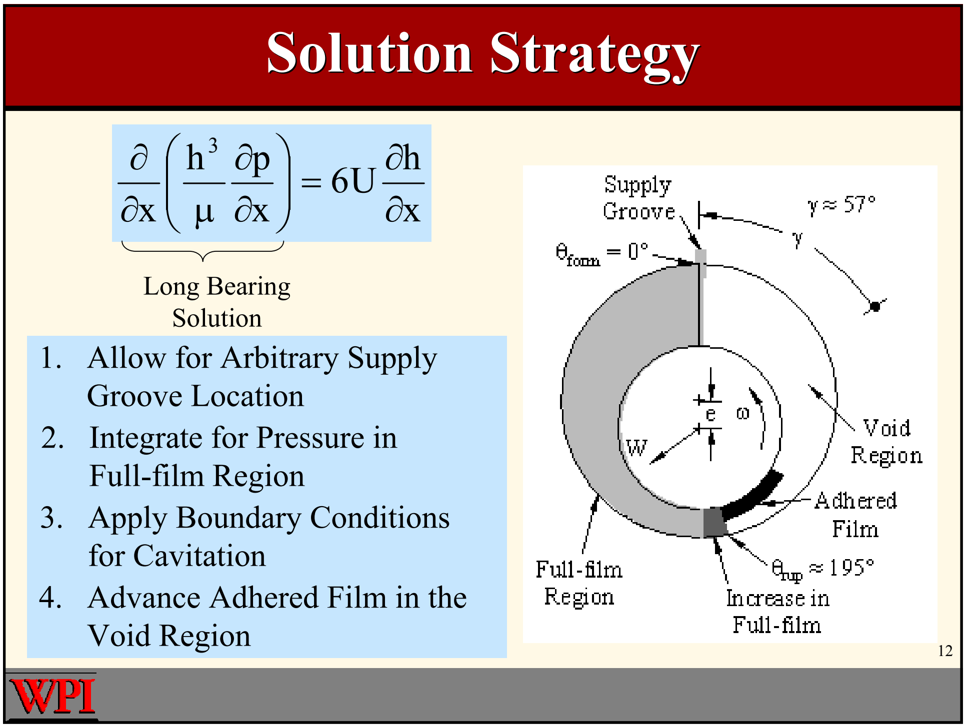

Solution Strategy

$$\underbrace{\frac{\partial}{\partial x}\left(\frac{h^3}{\mu}\frac{\partial p}{\partial x}\right)}_{\text{Long Bearing Solution}}=6U\frac{\partial h}{\partial x}$$

1. Allow for Arbitrary Supply Groove Location
2. Integrate for Pressure in Full-film Region
3. Apply Boundary Conditions for Cavitation
4. Advance Adhered Film in the Void Region

Arbitrary Supply Groove Placement

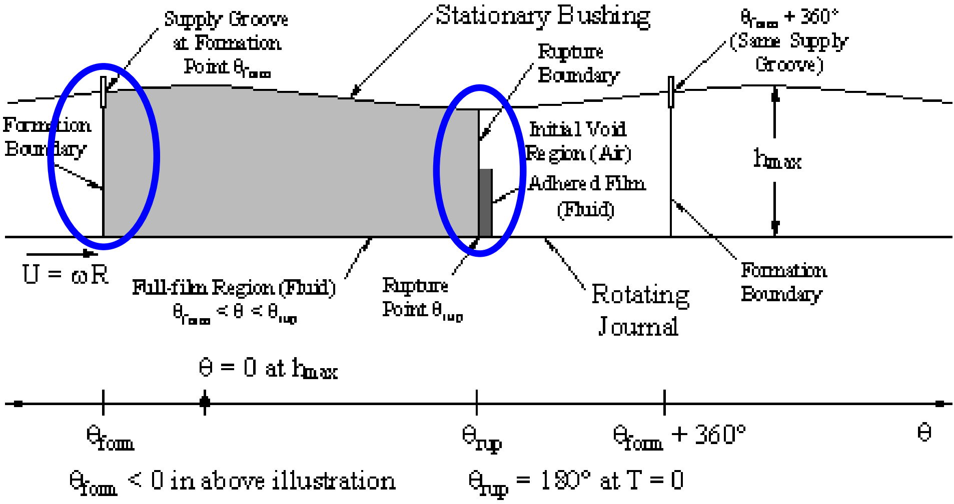

Invariant Flux

$$\phi = \int_0^h u(y)dy = \underbrace{\frac{Uh}{2}}_{\text{Couette Flow}} - \underbrace{\frac{h^3}{12\mu}\frac{\partial p}{\partial x}}_{\text{Poiseuille Flow}} = \phi_C + \phi_P = \text{Constant}$$

Non-dimensional Terms:

$$H = \frac{h}{C} = 1 + \varepsilon\cos\theta$$

$$\varepsilon = \frac{e}{C} \qquad \theta = \frac{x}{R}$$

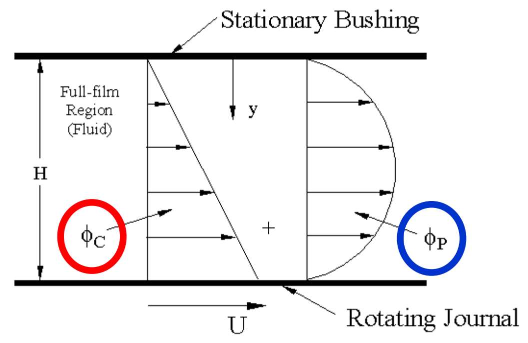

Pressure Profile

$$P = \frac{C^2}{6\mu RU}(p - p_0) = \underbrace{\int \frac{d\theta}{(1+\varepsilon\cos\theta)^2}}_{J_2} - H_0 \underbrace{\int \frac{d\theta}{(1+\varepsilon\cos\theta)^3}}_{J_3}$$

- Compact Form: $P = J_2 - H_0 J_3$
- Limits for Integrals:
  Lower → θ_{form}
  Upper → $\theta_{form} \le \theta \le \theta_{rup}$
- Boundary Conditions:
  $P = 0$ at θ_{form} and θ_{rup}

Non-dimensional Invariant Flux $$H_0 = \frac{2\phi}{UC} = \left.\frac{J_2}{J_3}\right|_{\theta_{form}}^{\theta_{rup}}$$

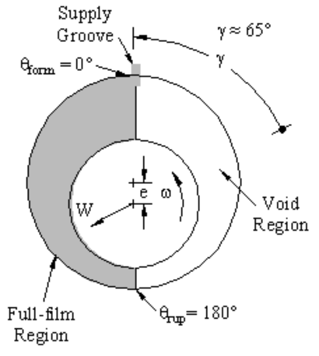

J_n Integrals

$$P = J_2 - H_0 J_3$$

Analytical Solution Allows for
1. **Arbitrary Terminal Points**
2. **Continuous Pressure Profile**

$$J_2 = \left[\frac{-\varepsilon\sin\theta}{(1-\varepsilon^2)(1+\varepsilon\cos\theta)}\right]_{\theta_{form}}^{\theta} + \frac{1}{(1-\varepsilon^2)} J_1$$

$$J_3 = \left[\frac{-\varepsilon\sin\theta}{2(1-\varepsilon^2)(1+\varepsilon\cos\theta)^2}\right]_{\theta_{form}}^{\theta} + \frac{3}{2(1-\varepsilon^2)} J_2 - \frac{1}{2(1-\varepsilon^2)} J_1$$

$$J_1 = \int_{\theta_{form}}^{\theta_{rup}} \frac{d\theta}{1+\varepsilon\cos\theta} = \left[\frac{2}{\sqrt{1-\varepsilon^2}} \tan^{-1}\left(\sqrt{\frac{(1-\varepsilon)}{(1+\varepsilon)}} \tan\frac{\theta}{2}\right)\right]_{\theta_{form}}^{\theta}$$

J_n Integrals

$$J_1 = \int_{\theta_{form}}^{\theta_{rup}} \frac{d\theta}{1+\varepsilon\cos\theta}$$

$$= \left[\frac{2}{\sqrt{1-\varepsilon^2}}\tan^{-1}\left(\sqrt{\frac{(1-\varepsilon)}{(1+\varepsilon)}}\tan\frac{\theta}{2}\right)\right]_{\theta_{form}}^{\theta}$$

Branch Points Removed and Continuous Integral!

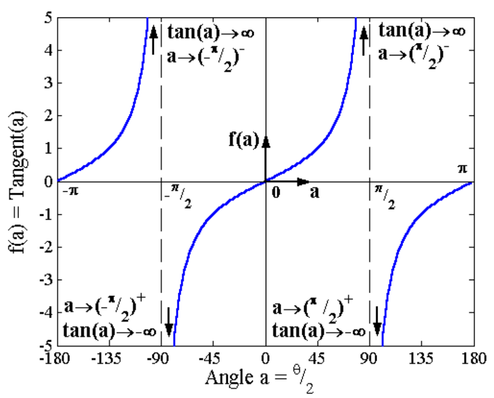

$$J_1 = \frac{2}{\sqrt{1-\varepsilon^2}}\,\mathrm{atan2}\left[\sqrt{1-\varepsilon^2}\,\sin\frac{(\theta-\theta_{form})}{2},\ \cos\frac{(\theta-\theta_{form})}{2}+\varepsilon\cos\frac{(\theta+\theta_{form})}{2}\right]$$

Swift-Stieber Boundary Condition

$$P = J_2 - H_0 J_3$$

$$H_0 = \frac{2\phi}{UC} = \left.\frac{J_2}{J_3}\right|_{\theta_{form}}^{\theta_{rup}} = H - H^3\frac{dP}{d\theta}$$

- **Special Case:** Additional Boundary Condition for Steady-State

Swift-Stieber Condition

$$\left(\frac{dP}{d\theta}\right)_{rup} = 0$$

Gives H_{ss}, θ_{ss}

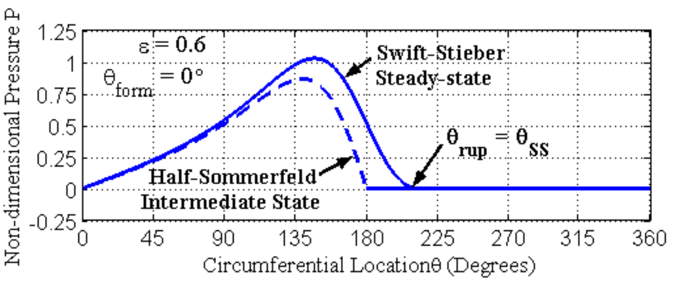

Examine Half-void **Intermediate States** for 180° $\leq\theta_{rup}\leq\theta_{ss}$

Contour Plots of Non-dimensional Flux

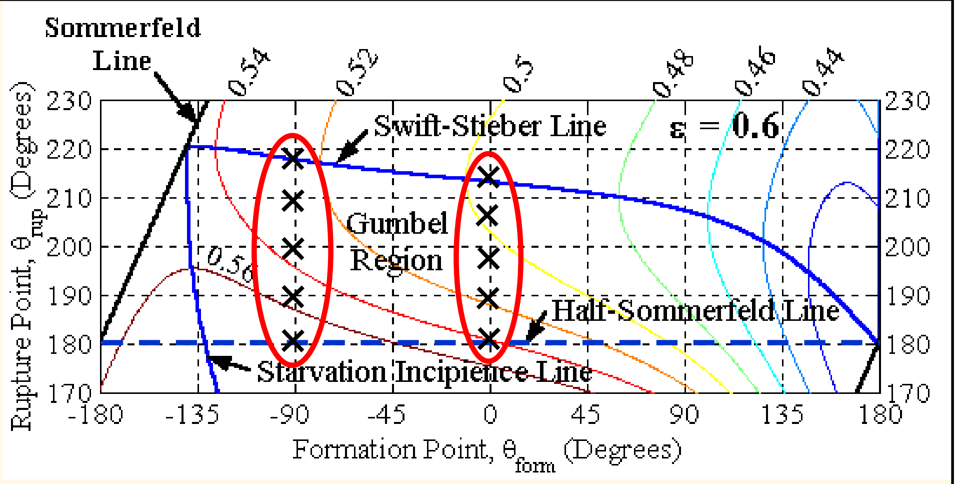

X's are Intermediate Gumbel States

Olsson's Equation at Rupture Point

$$\phi_C + \phi_P = \phi_a + \phi_{void}$$

$$\frac{UH_{rup}}{2} - \frac{UH_{rup}^3}{2}\left(\frac{dP}{d\theta}\right)_{rup} = U\alpha_{rup}H_{rup} + U_{rup}H_{rup}(1-\alpha_{rup})$$

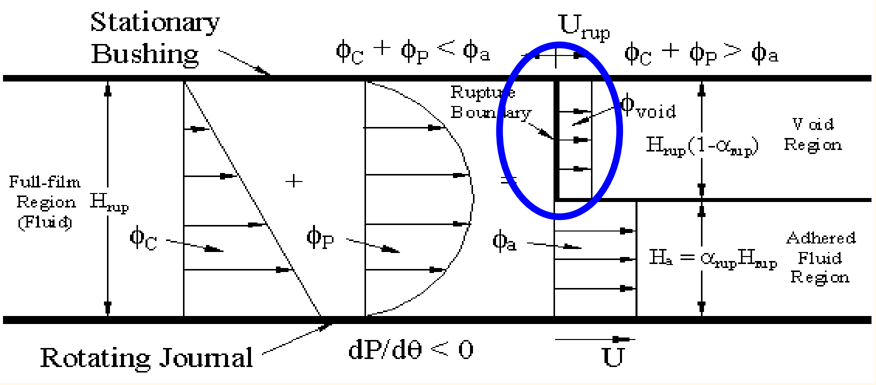

Rupture Point Speed U_{rup}

$$\frac{UH_{rup}}{2} - \frac{UH_{rup}^{3}}{2}\left(\frac{dP}{d\theta}\right)_{rup} = U\alpha_{rup}H_{rup} + \boxed{U_{rup}}H_{rup}(1-\alpha_{rup})$$

Consider Steady-state: $U_{rup} = 0$ and $\left(\frac{dP}{d\theta}\right)_{rup} = 0$

$$\therefore \alpha_{rup} = \frac{1}{2} \rightarrow H_a = \frac{H_{rup}}{2}$$

Half-void Fraction is Basis for Adhered Film!

$$\boxed{U_{rup}} = -UH_{rup}^{2}\left(\frac{dP}{d\theta}\right)_{rup} = U\left(\frac{H_0}{H_{rup}} - 1\right)$$

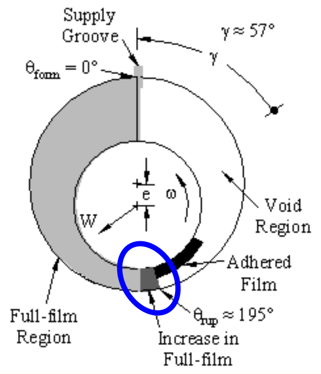

Intermediate Gumbel States

U_{rup} Calculated at Evenly Spaced Intervals

$180° \leq \theta_{rup} \leq \theta_{ss}$

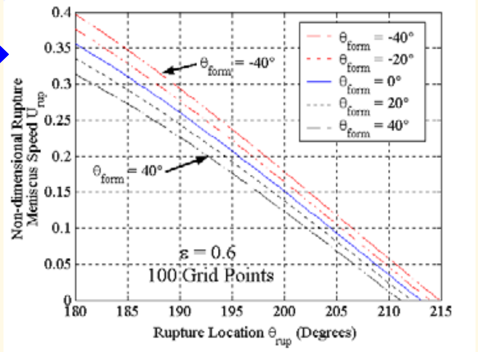

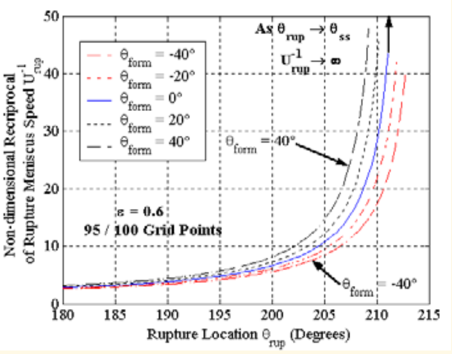

Time T to Intermediate States Obtained from Integration of Reciprocal of Rupture Speed!

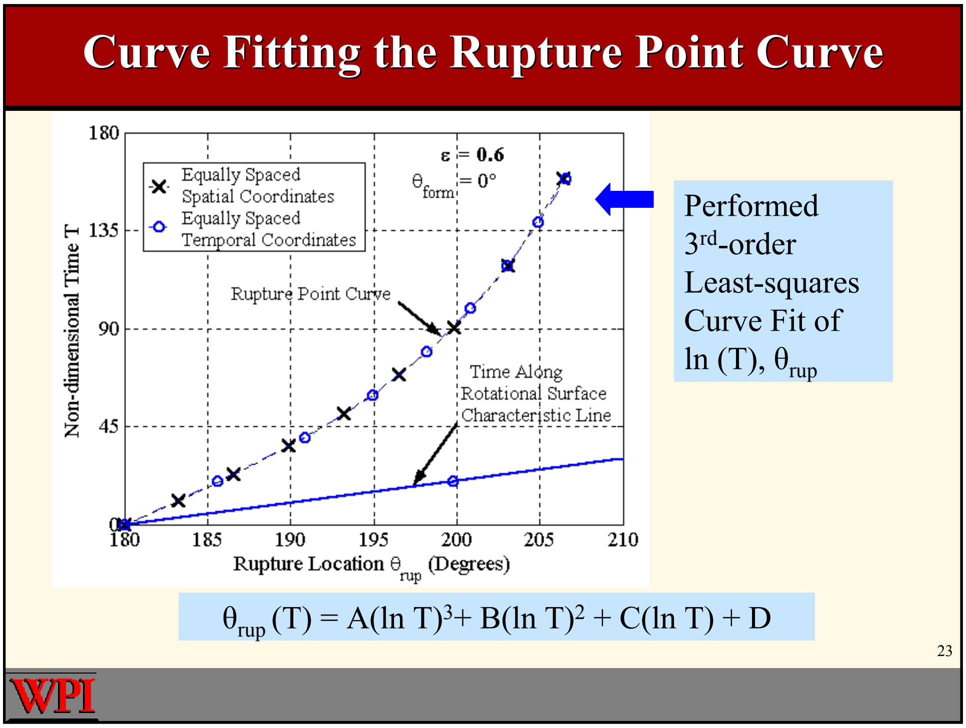

Curve Fitting the Rupture Point Curve

Performed 3^{rd}-order Least-squares Curve Fit of ln (T), θ_{rup}

$$\theta_{rup}(T) = A(\ln T)^3 + B(\ln T)^2 + C(\ln T) + D$$

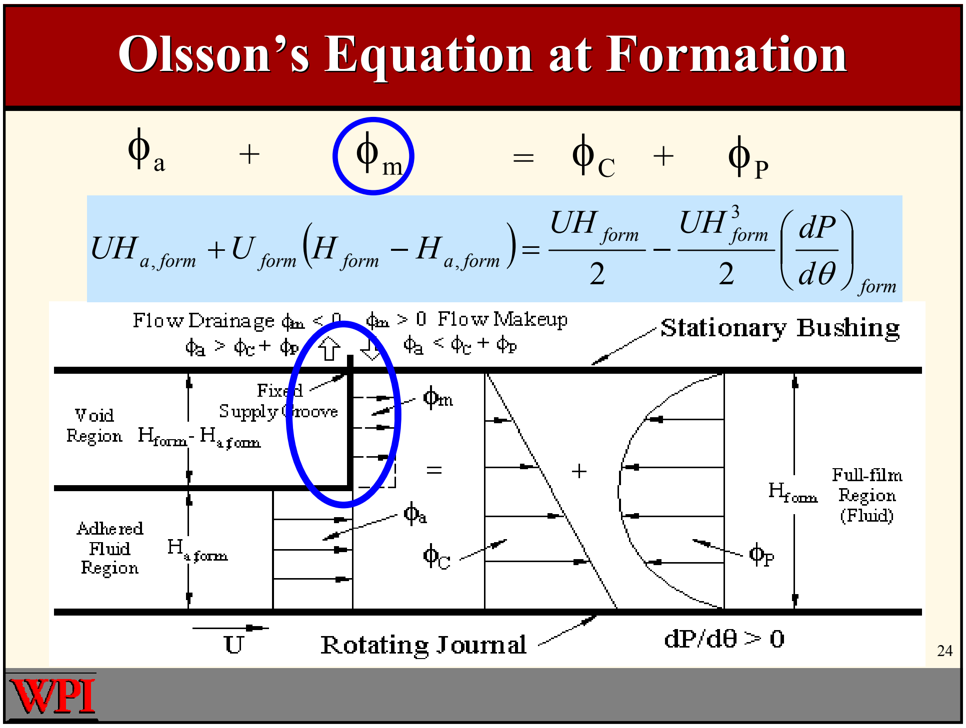

Olsson's Equation at Formation

$$\phi_a + \phi_m = \phi_C + \phi_P$$

$$UH_{a,form} + U_{form}\left(H_{form} - H_{a,form}\right) = \frac{UH_{form}}{2} - \frac{UH^3_{form}}{2}\left(\frac{dP}{d\theta}\right)_{form}$$

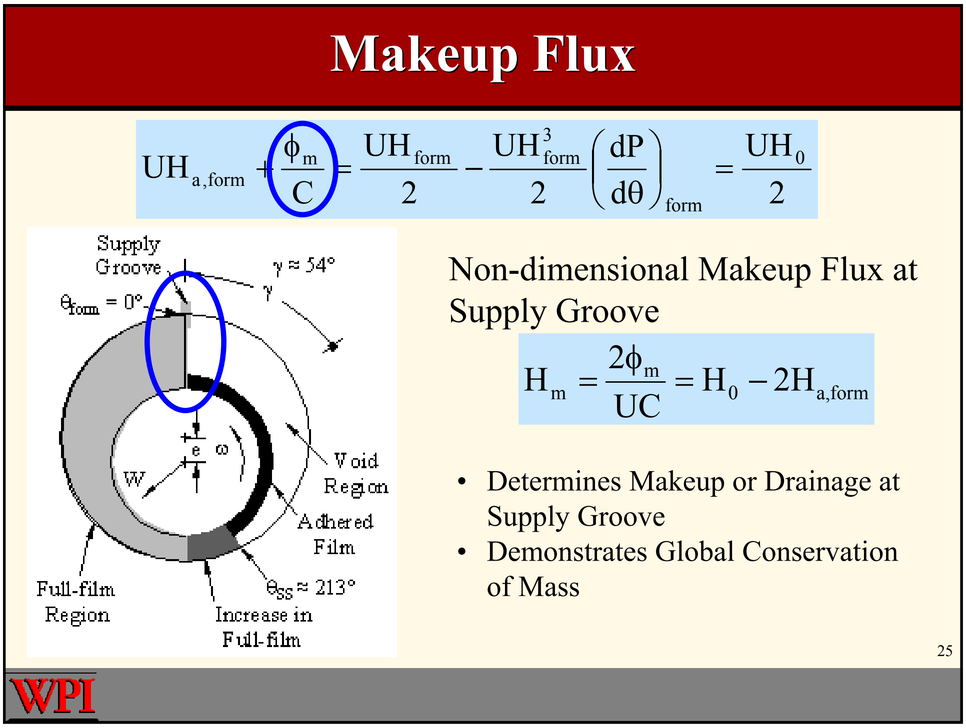

Makeup Flux

$$UH_{a,form} + \frac{\phi_m}{C} = \frac{UH_{form}}{2} - \frac{UH^3_{form}}{2}\left(\frac{dP}{d\theta}\right)_{form} = \frac{UH_0}{2}$$

Non-dimensional Makeup Flux at Supply Groove

$$H_m = \frac{2\phi_m}{UC} = H_0 - 2H_{a,form}$$

- Determines Makeup or Drainage at Supply Groove
- Demonstrates Global Conservation of Mass

25

WPI

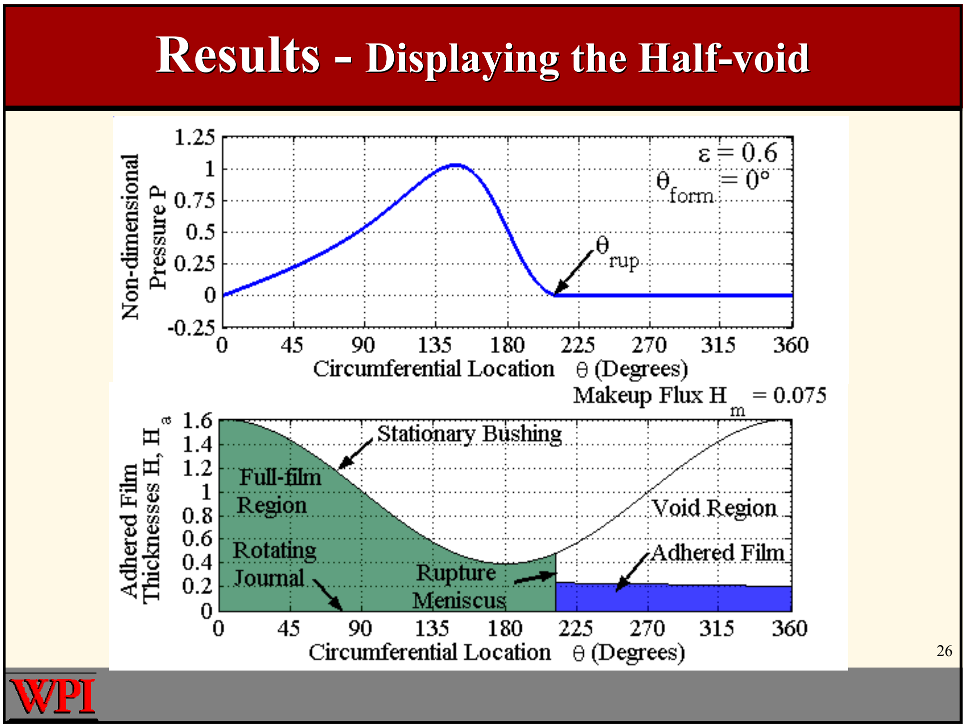

Results - Displaying the Half-void

26

WPI

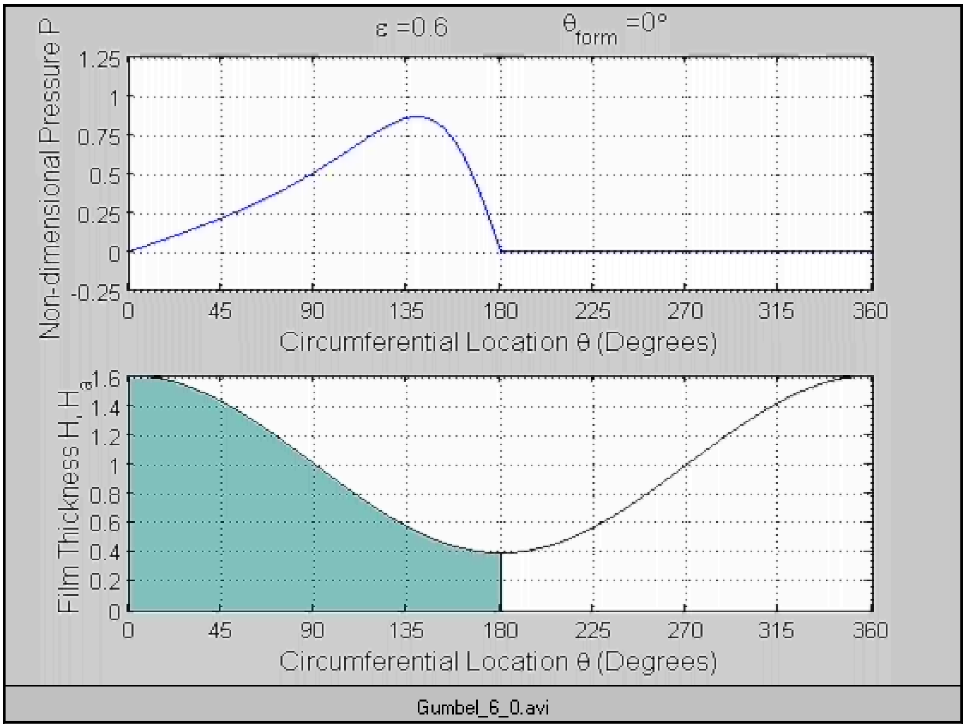
ε =0.6
θ_{form} =0°
Non-dimensional Pressure P
1.25
1
0.75
0.5
0.25
0
-0.25
0
45
90
135
180
225
270
315
360
Circumferential Location θ (Degrees)
Film Thickness H, H_a
1.6
1.4
1.2
1
0.8
0.6
0.4
0.2
0
0
45
90
135
180
225
270
315
360
Circumferential Location θ (Degrees)
Gumbel_6_0.avi

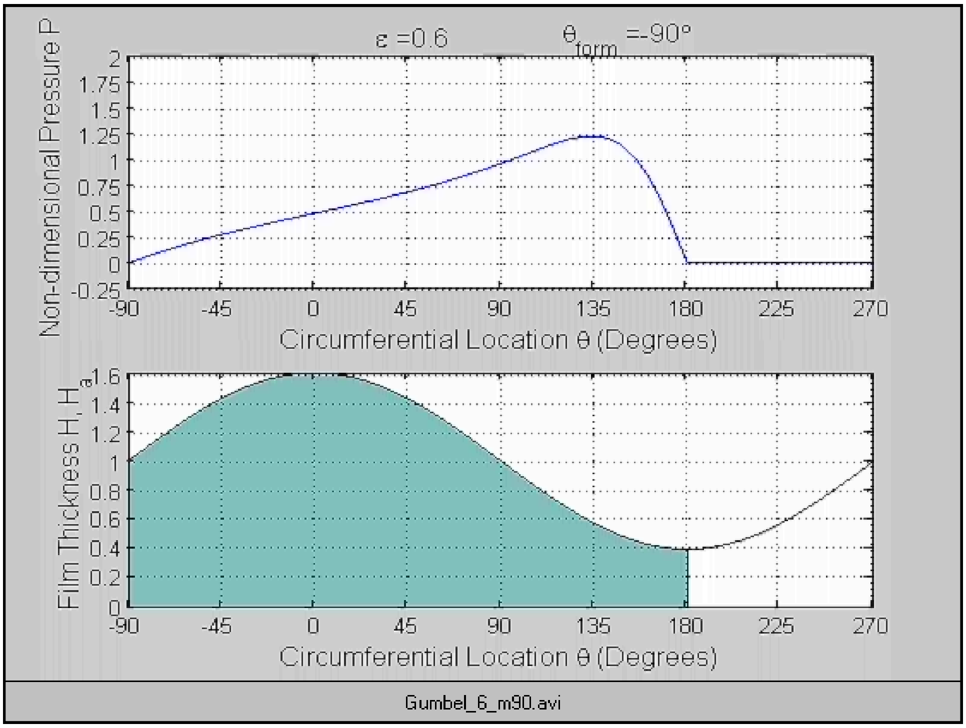
ε =0.6
θ_{form} =-90°
Non-dimensional Pressure P
2
1.75
1.5
1.25
1
0.75
0.5
0.25
0
-0.25
-90
-45
0
45
90
135
180
225
270
Circumferential Location θ (Degrees)
Film Thickness H, H_a
1.6
1.4
1.2
1
0.8
0.6
0.4
0.2
0
-90
-45
0
45
90
135
180
225
270
Circumferential Location θ (Degrees)
Gumbel_6_m90.avi

Results - Makeup Flux at Supply Groove

- Makeup Flux H_m is Invariant Flux H_0 until Adhered Film H_a Arrives
- Steady-State Makeup Flux Goes to Zero

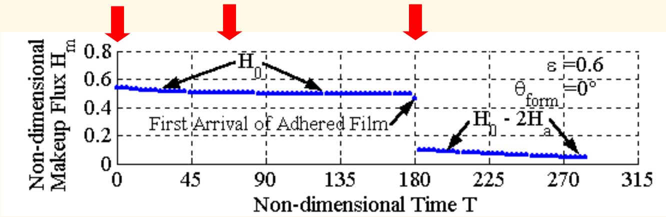

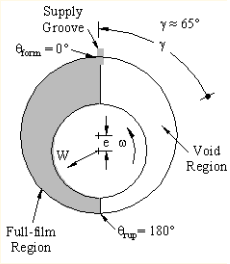

T = 0

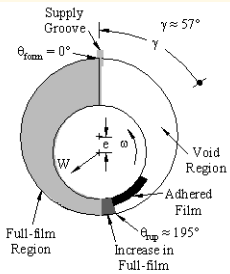

T = 60

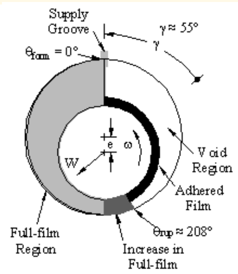

T = 180

Load Capacity

Tangential Component

$$W_x = LR \int_{\theta_{form}}^{\theta_{rup}} P \sin\theta \, d\theta$$

Radial Component

$$W_y = -LR \int_{\theta_{form}}^{\theta_{rup}} P \cos\theta \, d\theta$$

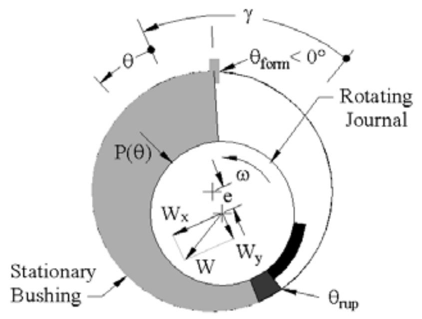

Non-dimensional Load Capacity

$$\frac{W}{LR} = \sqrt{W_x^2 + W_y^2}$$

Attitude Angle

$$\tan\gamma = \frac{W_x}{W_y}$$

Load Capacity

Tangential Component

$$\frac{W_x}{LR} = \frac{1}{\varepsilon}\left[(J_1 - J_2) - H_0(J_2 - J_3)\right]_{\theta_{form}}^{\theta_{rup}}$$

Radial Component

$$\frac{W_y}{LR} = \frac{1}{\varepsilon}\left[\frac{1}{H} - \frac{H_0}{2H^2}\right]_{\theta_{form}}^{\theta_{rup}}$$

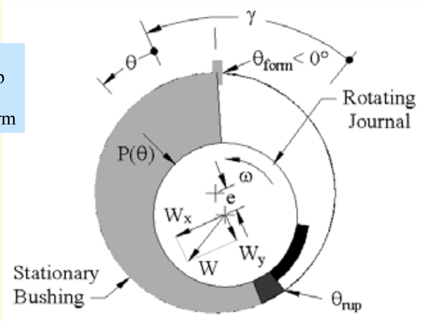

Non-dimensional Load Capacity

$$\frac{W}{LR} = \sqrt{W_x^2 + W_y^2}$$

Attitude Angle

$$\tan\gamma = \frac{W_x}{W_y}$$

Results - Load Capacity

W,γ shown here for θ_{form} = -45°
W,γ at T = 0 ⇢
W,γ at T_{SS} →

W – Load Capacity (magnitude)
γ – Attitude Angle (direction)

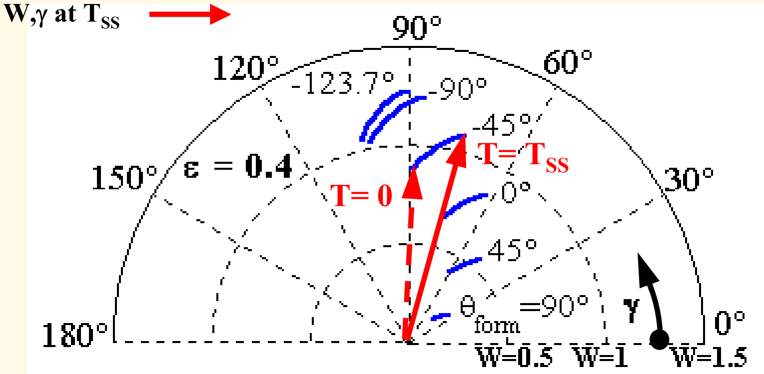

Blue Lines are Time Dependent Paths for Load Vectors!
(Only Initial and Final Values Found in Textbooks)

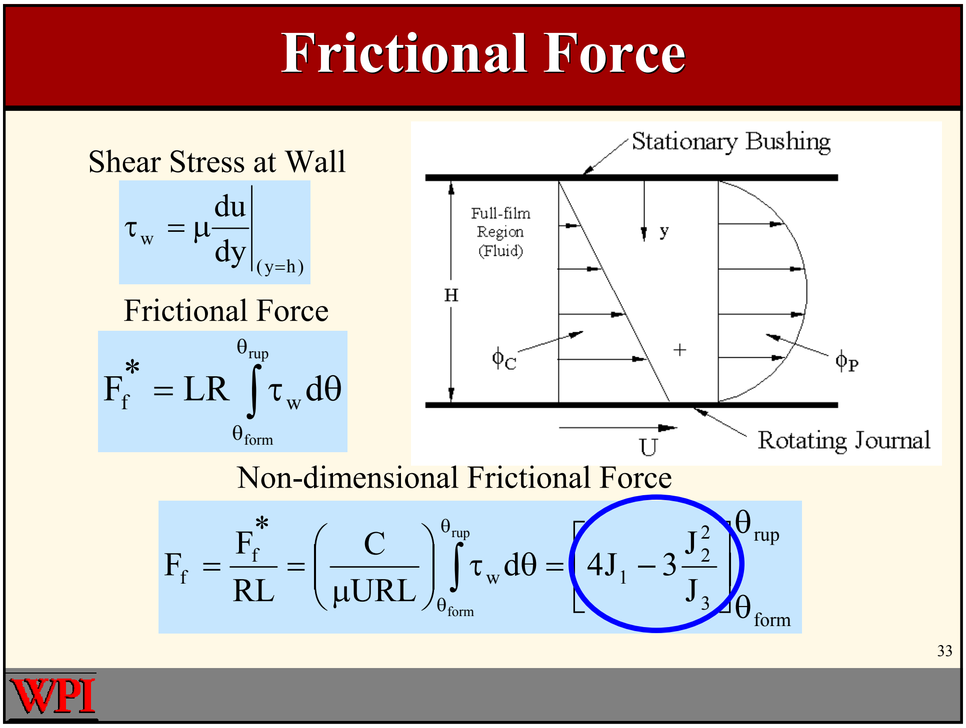

Frictional Force

Shear Stress at Wall

$$\tau_w = \mu \left.\frac{du}{dy}\right|_{(y=h)}$$

Frictional Force

$$F_f^* = LR\int_{\theta_{form}}^{\theta_{rup}} \tau_w \, d\theta$$

Non-dimensional Frictional Force

$$F_f = \frac{F_f^*}{RL} = \left(\frac{C}{\mu URL}\right)\int_{\theta_{form}}^{\theta_{rup}} \tau_w \, d\theta = \left[4J_1 - 3\frac{J_2^2}{J_3}\right]_{\theta_{form}}^{\theta_{rup}}$$

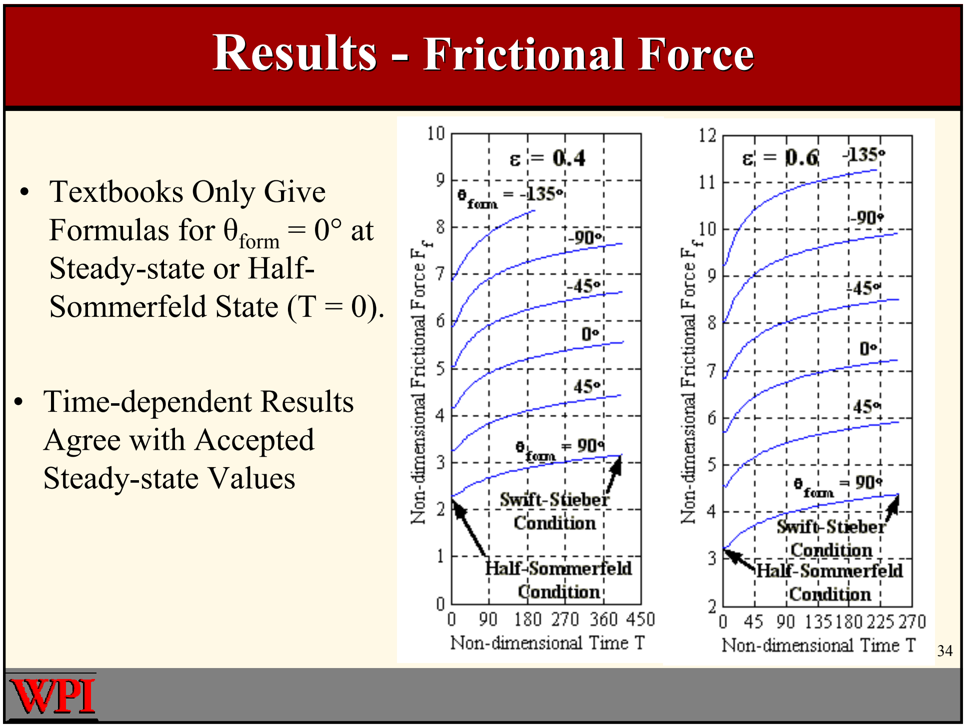

Results - Frictional Force

- Textbooks Only Give Formulas for $\theta_{form} = 0°$ at Steady-state or Half-Sommerfeld State (T = 0).
- Time-dependent Results Agree with Accepted Steady-state Values

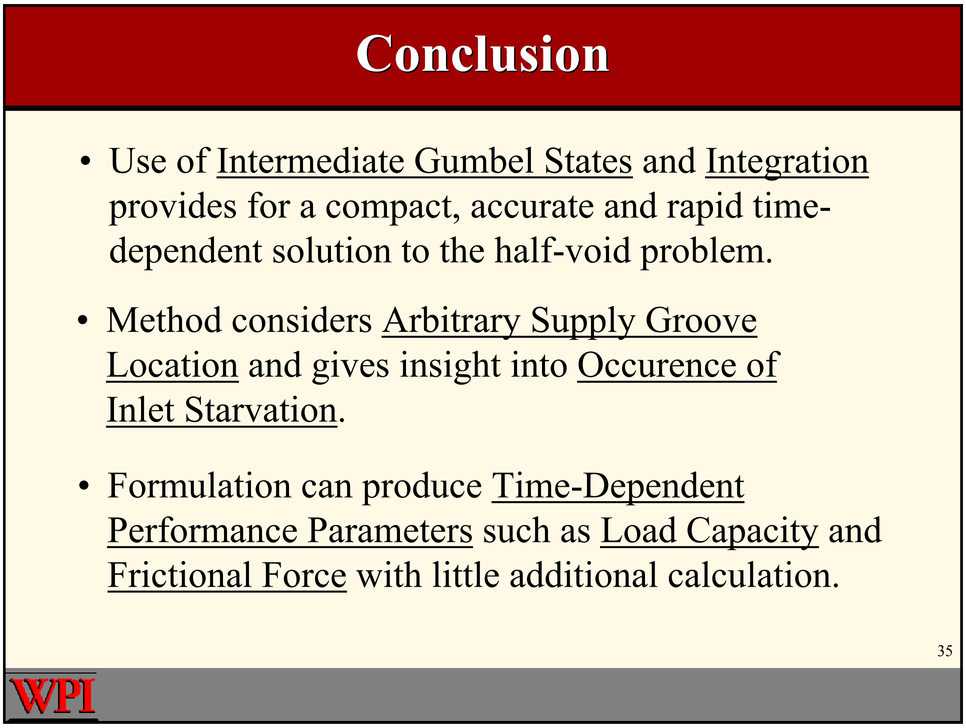

Conclusion

- Use of Intermediate Gumbel States and Integration provides for a compact, accurate and rapid time-dependent solution to the half-void problem.
- Method considers Arbitrary Supply Groove Location and gives insight into Occurence of Inlet Starvation.
- Formulation can produce Time-Dependent Performance Parameters such as Load Capacity and Frictional Force with little additional calculation.

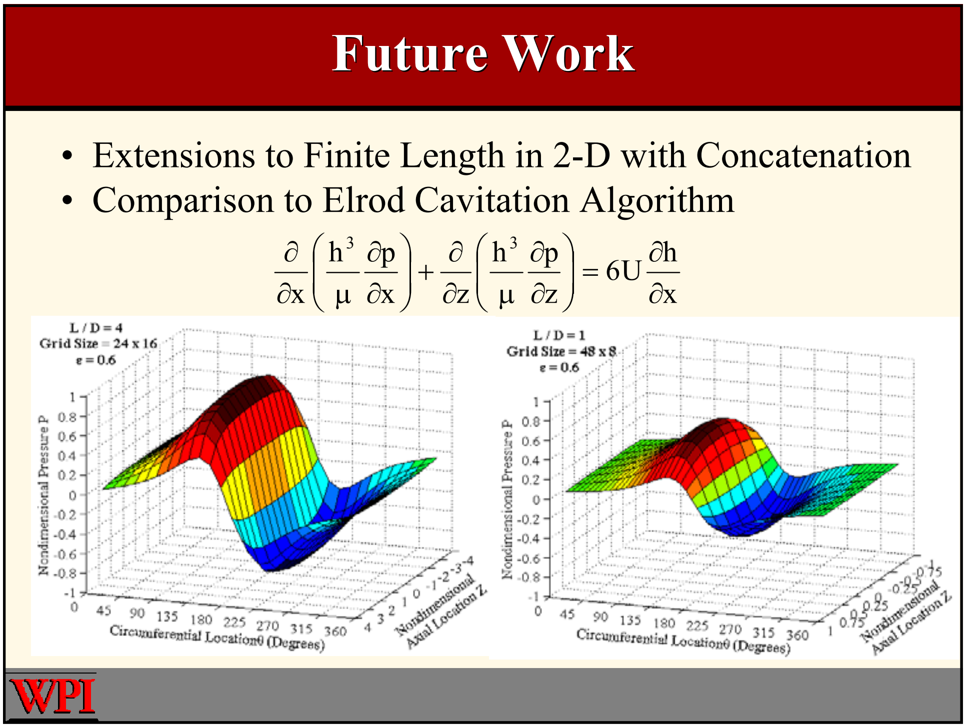

Future Work

- Extensions to Finite Length in 2-D with Concatenation
- Comparison to Elrod Cavitation Algorithm

$$\frac{\partial}{\partial x}\left(\frac{h^3}{\mu}\frac{\partial p}{\partial x}\right)+\frac{\partial}{\partial z}\left(\frac{h^3}{\mu}\frac{\partial p}{\partial z}\right)=6U\frac{\partial h}{\partial x}$$

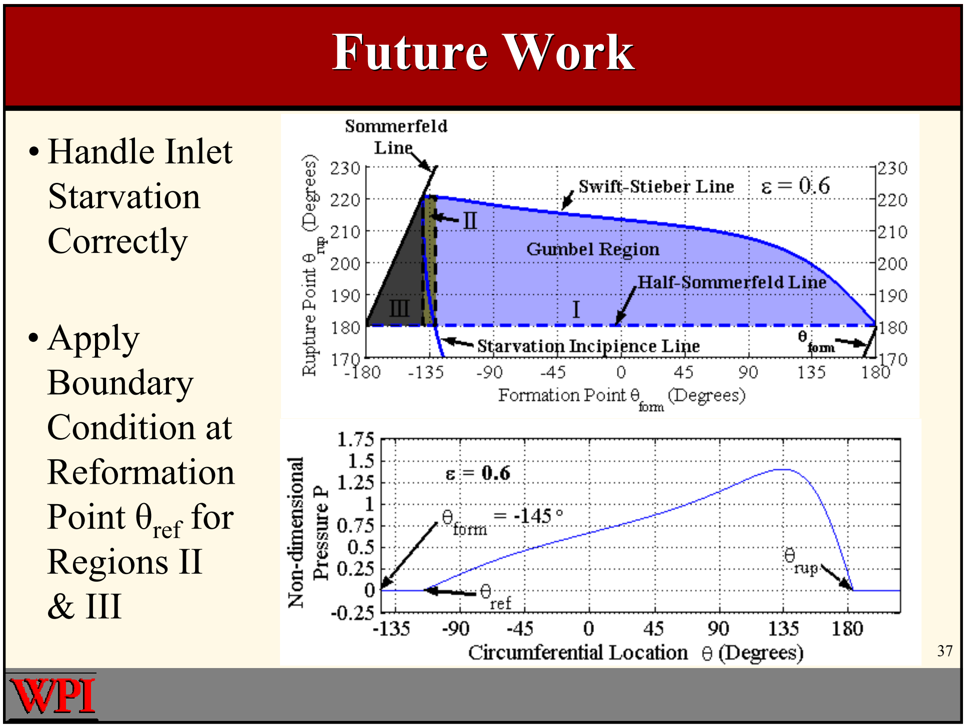

Future Work

- Handle Inlet Starvation Correctly
- Apply Boundary Condition at Reformation Point θ_{ref} for Regions II & III

Acknowledgements

- **Professor Joseph Rencis**
- **Dr. Coda H. T. Pan**
- **National Science Foundation**

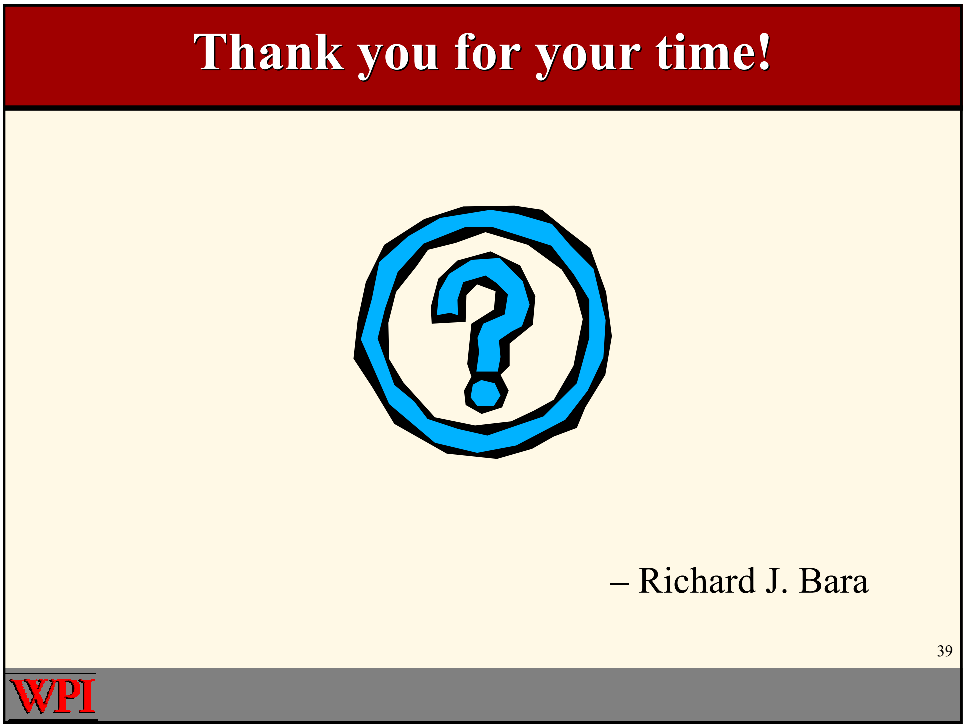

Thank you for your time!

– Richard J. Bara